Determining the characteristics of icy moons' impactors

An experimental approach

Filippo Tagliacarne

Technische Universiteit Delft

TU Delft

Determining the characteristics of icy moons' impactors

An experimental approach

by

Filippo Tagliacarne

to obtain the degree of Master of Science
at the Delft University of Technology,
to be defended publicly on Friday July 15, 2022 at 13:30.

Student number: 4670930
Project duration: September 1, 2021 – July 15, 2022
Thesis committee: Dr. S. Cazaux, Chair/Supervisor
Dr. ir. B. Root, Supervisor
Dr. Y. Tang, External examiner

Cover image credit: NASA/ESA

TU Delft

Preface

Contrary to a lot of my colleagues, I will not be ending my Master's career with this thesis as I have my internship to conclude (we can thank COVID-19 for that). However, the conclusion of this thesis signifies an end of a nine-month chapter of my life.

This thesis would have never been possible without the help of my supervisor, Dr. Stéphanie Cazaux, who infected me with her enthusiasm for the subject, and Dr. ir. Bart Root challenged my thinking process with his understanding of impact cratering. I also want to thank Dr. Sebastiaan de Vet and Dr. Yinglu Tang, who helped at the beginning of the thesis. I want to extend my gratitude to everyone else that contributed to my thesis, Dr. Miguel Ángel Satorre Aznar who helped me better understand amorphous ice, Dr. Josefina Torres Redondo, Dr. Guillermo Manuel Muñoz Caro, and Dr. Asper Chen who helped me design the final container for my thesis, Dr. Jérôme Loicq who helped me understand remote sensing capabilities for ice types, Ines Uriol Balbin who helped me with tracking options for high-speed camera footage, Huseyin Eryoruk who helped me with the gas gun at DASML, and a final thanks to the entire staff at DASML who helped me navigate the lab and fix any issues that arose. A special thanks to my friends and anyone who read through my thesis and helped me deliver a better report.

For those of you who will read this report for professional reasons, I hope this work can help you better understand impact cratering and its importance in our understanding of the history of our solar system.

Filippo Tagliacarne
Delft, July 2022

Abstract

Crater counting is the main method used to determine the age of a planetary surface. This method relies on knowing the cratering rate to estimate the absolute age of a surface. However, two theories currently exist for impact cratering of the moons in the Saturnian system, one suggesting that the majority of the impactors are of heliocentric origin (i.e. they come from orbits around the Sun), and the other suggesting that the majority of impactors are of planetocentric origin (i.e. they originate from orbits around Saturn). The different theories result in very different surface ages of the icy moons. According to the heliocentric model, the surface of Titan would date to $\approx$3 Ga, while according to the planetocentric model the surface of Titan could be dated between $\approx$15 Ma and $\approx$4 Ga, allowing for much more erosion of the surface according to Bell (2020). Given that these two orbits result in different impact velocities, this work attempts to discover if the impact velocity can be determined for impactors on icy moons based on crater characteristics, such as crater depth and diameter, by recreating impacts in the lab.

Previous impact experiments have been performed with different impactors and target materials. This study aims at expanding previous research by performing tests on icy particles, something not done before. The data obtained from experiments are then used to obtain the estimated impactor diameter that created craters on the surface of these icy moons based on the expected impact velocities. This data can then be used to predict the likelihood of an impactor originating from either a heliocentric or planetocentric orbit.

This work developed several methods to produce impact craters using different instruments and different surfaces. The best results were obtained either with the gas gun and ice blocks or with the drop tower and icy particles. Using the scaling relationships found in this work, it was shown that the required impactor diameter can be obtained from craters on icy moons and that a distinction can be made between planetocentric and heliocentric impactors. However, more work is needed to narrow down the scaling relationship to obtain a reasonable impactor diameter given a certain impact crater. More information about the crater, such as the transition of ice type during an impact, should be used in the future to further constrain the velocity ranges.

Contents

List of Figures

List of Tables

Acronyms

DASML Delft Aerospace Structures and Materials Laboratory. iii, xi, 17, 20

FOV field of view. 27, 44

HDA high density amorphous. 12

LN_2 Liquid Nitrogen. 26, 67, 69

LDA low density amorphous. 12

LHB Late Heavy Bombardment. 11

MBA Main Belt Asteroids. xi, xiii, 6, 60

MMS-2 Mojave Mars Simulant 2. xii, xv, 25, 33, 35, 37–39

NEO Near Earth Object(s). 4

TNO Trans Neptunian Object(s). 4

WLTT Weak Line T Tauri. 3

1

Introduction

Icy moons have been of particular interest to scientists lately as the presence of water on an extraterrestrial body is always of great interest. In particular, it is hypothesized that many of these icy moons have a subsurface ocean, like Europa, Ganymede, and Enceladus. The presence of liquid water makes these moons even more interesting as the presence of liquid water is one of the essential elements required for life. It is therefore important to know as much as possible about these icy moons. Among other things, the age of these icy surfaces is not very well known. Impact cratering is the most common tool used to remotely determine the age of a surface. However, for icy moons, especially the ones orbiting Jupiter and Saturn, the origin of the impactors is uncertain. Two theories currently exist on the origin of these impactors. The first is the so-called *heliocentric* theory, which states the impactors come from a heliocentric orbit which is the case for most impactors for the rocky planets in our solar system. The second theory is the *planetocentric* theory. This theory states that most impactors originate from planetocentric orbits. This planetocentric theory would result in impactors with an unknown impact frequency and impact mass, however, the impact velocity would be lower compared to heliocentric impactors which would decrease the impact energy for an object with the same mass. In his paper, Bell (2020) analyzed the relative crater density for various moons of the Saturnian system to estimate the relative age of the surfaces of these moons. His analysis showed that under the heliocentric crating theory, there should be an increase in relative cratering density with increasing distance from Saturn, meaning that the surface of Titan is as old as, if not older, than the surface of Mimas. This estimate for the surface age of Titan does not match the observation of what looks like a very young surface (Lorenz et al., 2007). Bell (2020) tried to obtain a better estimate using an extreme quasi-equilibrium saturation model (Kirchoff et al., 2018) and the young moon hypothesis (Ćuk et al., 2016), however, neither of these theories resulted in a surface age of Titan compatible with observations. Bell (2020) then showed that under planetocentric cratering, the surface of Titan could be as young as $\approx$15 Ma and the surfaces of Mimas, Tethys, Dione, Rhea, and Iapetus would have similar surface ages between them. However, Bell (2020) was unable to rule how saturation effects, which could also explain the apparent younger age of Titan and the different crater densities for Mimas, Tethys, Dione, Rhea, and Iapetus.

This report is divided into eight chapters. Chapter 2 summarizes all the required scientific background needed to understand this thesis. This chapter includes information on minor bodies in the solar system, impact craters and how they are formed, a summary of previous work on the subject, and the knowledge gap this research attempts at solving. Chapter 3 includes a breakdown of all the instruments used for the experiments, including the challenges encountered when using these instruments. This chapter also describes the containers used to experiment on the samples, along with a description of the samples and how they are prepared. Chapter 4 describes the verification and validation of the data used in this thesis. This includes assumptions made in the measurement of velocity, along with ensuring measured data is valid, such as velocity and sample density. Chapter 5 describes all the data pertaining to rocky craters. The chapter starts by describing the experiments that were carried out, then goes on to describe the data obtained for the above-mentioned experiments. The data obtained is then compared to previous work, and finally, it is analyzed and discussed in the final section. The same structure applies to chapter 6, where data pertaining to icy craters is analyzed. Chapter 7 applies the finding of this research to icy moons, describing how the data obtained can be

used to further our understanding of these bodies. Finally, chapter 8 wraps up this report by reflecting on the research questions, along with providing recommendations for future studies.

2

Scientific Background

This study investigates crater properties on icy surfaces to determine the origin of the impactors that created said craters. This chapter provides the relevant background information needed for this study. Section 2.1 discusses the origin, classification, and characteristics of minor bodies in the solar system. Section 2.2 discusses the crater anatomy, the process of crater formation, and different crater types. Section 2.3 briefly discusses the Jovian and Saturnian systems (the two systems with the largest number of icy moons), followed by the two main cratering models, heliocentric and planetocentric. The section concludes by discussing various types of ice and how they are formed. Section 2.4 discusses the previous experimental work done on rocky and icy craters respectively. Finally, this chapter concludes with section 2.5, which discusses the knowledge gap and research questions to be answered by this work.

2.1. Small bodies in the solar system

The term *small bodies*, when in the context of the solar system, refers to objects such as asteroids, comets, and any other object that is not a planet, moon, or dwarf planet (Resolution, 2006). In this section, the origin, classification, and characteristics of such bodies will be discussed.

2.1.1. Origin of small bodies

The solar system formed in a molecular cloud, from the collapse of a slowly rotating nebula. The evolution of a star system resulting in a star of comparable mass to the Solar System's sun is described by the Nebula hypothesis, first conceived in the 18th century (Kant, 1755). This process is summarized in Figure 2.1 (Hogerheijde et al., 1998). Tile (a) shows the molecular cloud, with the areas of higher density shaded darker. As the gravitational force pushes the material towards one point, the gravitational potential energy is converted into kinetic energy and then into heat (b). After that point, about 10^4-10^5 yr after the initial collapse, a protostar is born as the 8000 AU disk continues to collapse inwards (c). A T Tauri star follows the initial protostar which lasts around 10 million years (d). This is then followed by a pre-main-sequence star, also known as Weak Line T Tauri (WLTT) stars, which usually lasts tens of millions of years (e). These pre-main-sequence stars still have a remnant disk around them. Eventually, the star becomes a main-sequence star, and planets and other objects form from the remnant disk (f) (Lissauer & de Pater, 2019). The way planets formed from the remnant disk is a topic of much debate and there currently exist three theories to explain how it happened. The planetary accretion theory states that dust from the protoplanetary disk slowly collided eventually forming larger objects. These objects kept growing until all gas from the orbit was cleared. The disk instability hypothesis states that gravitational instabilities in the protoplanetary disk caused by the star collapse cause clumps of materials to form. The third and last theory, core-accretion, states that dust will collide and aggregate until it forms a protoplanet (the beginning of a planet) which then accretes gas until it runs out. The protoplanetary disk is also where asteroids are formed, and depending on their type, they can be formed in one of two main ways. Undifferentiated asteroids form similarly to rocky planets, however, the planetesimals never develop to a full planet (Lissauer & de Pater, 2019). Differentiated asteroids, on the other hand, form mostly when an impact occurs between two or more objects. Since heavier

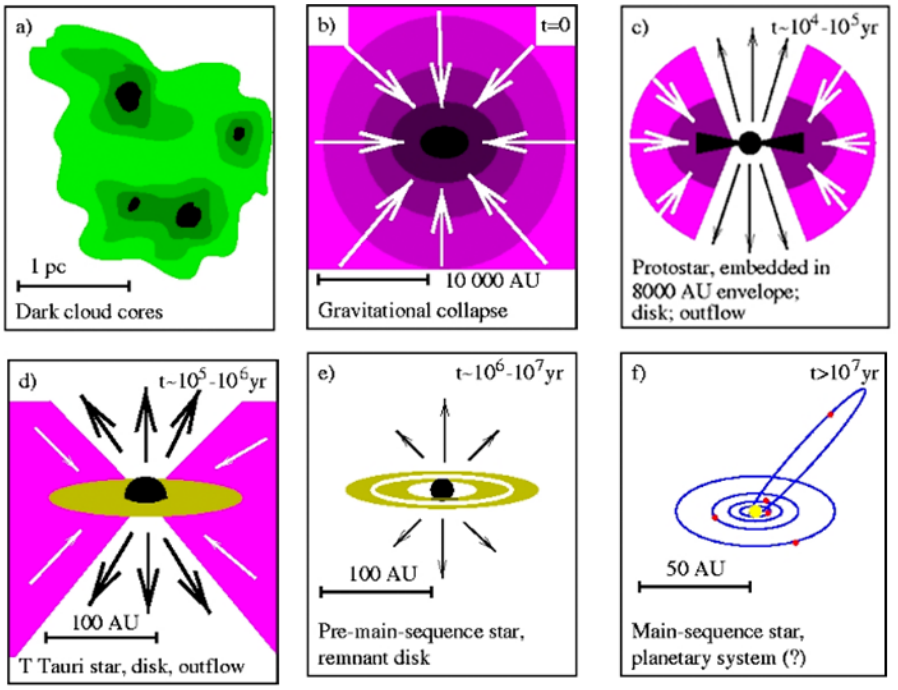

Figure 2.1: Process of star formation. A young star evolves from class 0 in tile (a) to a class III star in tile (e) before becoming a main sequence star just like the Sun in tile (f)(Hogerheijde et al., 1998)

elements like metals tend to ”sink” to the bottom of planets, the collision would allow for these differentiated materials to come out and become their own asteroids. Some of the undifferentiated asteroids can also become differentiated with heating from the Sun and/or short-lived radioactive isotopes like ^{26}Al (Woolum & Cassen, 1999). The distance from the Sun also means less accretion time (objects closer to the Sun would fall in faster). These two elements combined make it so asteroids closer to the sun are more differentiated (Davis et al., 2003)

2.1.2. Classification of asteroids and comets

Asteroids are classified in many different ways, the two most common ones are separated by their orbital characteristics or composition. For this study, the most important classification is the one based on their orbital characteristics, as that defines the speed with which the asteroid will impact a body. The largest asteroid group is the main belt asteroids, located between 2.1 and 3.3 AU from the Sun as can be seen from Figure 2.2. It is important to note that these asteroids are not uniformly distributed in the given orbital range, but are concentrated away from resonance orbits with Jupiter. These orbits appear as ”gaps” in the asteroid distribution and are called Kirkwood gaps (Dermott & Murray, 2020). The second group of asteroids is asteroids that come close to Earth’s orbit, or cross it, which is why they are called Near Earth Object(s) (NEO). The third group is the Trojan asteroids which are located at the L_4 and L_5 points of planets. These asteroids are also called Lagrange librators due to their location and the largest group is located around Jupiter’s Lagrange points (Chiang & Lithwick, 2005; Sheppard, 2006). The fourth group is called Hildas and it is located between the main belt and Jupiter’s orbit. These asteroids are in orbital resonance with Jupiter, and therefore appear clumped in three main groups as shown in Figure 2.3. The final group is composed of Trans Neptunian Object(s) (TNO) and Centaurs. TNOs are small bodies whose orbit lies (almost) completely outside the one of Neptune, while Centaurs orbit between Jupiter’s orbit and Neptune’s.

Just like asteroids, comets are also classified by their origin and orbit. The two most common origin points for comets are the Kuiper belt and Oort cloud. The Kuiper belt is a circumstellar disc extending between 30 and 50 AU (Fraser et al., 2017). Because of its disc shape and distance from the Sun, most Kuiper belt comets are short-period comets (<200 years) with orbits near the ecliptic plane (i.e.

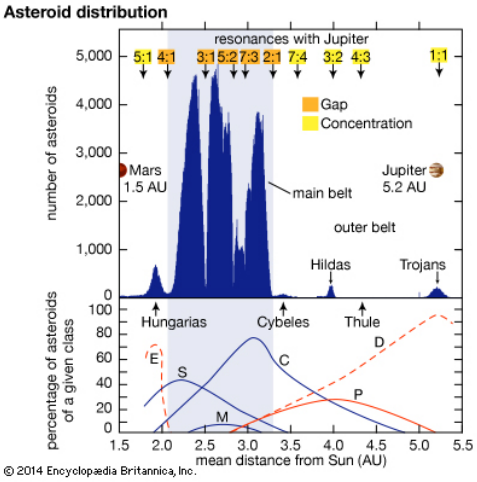

Figure 2.2: Asteroid distribution along with some of the most important asteroid families. Credit: Tedesco (2021)

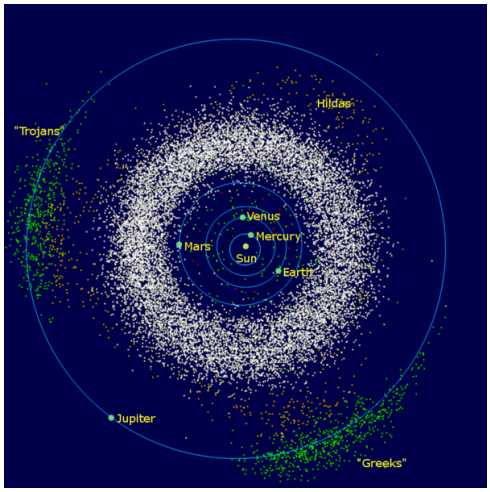

Figure 2.3: The inner Solar System, from the Sun to Jupiter. Jupiter's Trojans in green, Hildas in brown, and NEOs in red. Credit: Mdf (2006)

$i \sim 0°$) and bound (i.e. elliptic). The Oort cloud is a region of space between 2000 to ≈200 000 AU completely surrounding the solar system (Barucci et al., 2005). Therefore, comets coming from this region are long-period comets (≫200 years) with orbits of all shapes (i.e. hyperbolic, elliptic, parabolic) and orientation (Davis et al., 2003). Because of their ever-changing orbits, the Tisserand parameter (defined by Equation 2.1) is used to classify these comets (Murray & Dermott, 1999).

$$T_J = \frac{a_J}{a} + 2\left[\left(1 - e^2\right)\frac{a}{a_J}\right]^{1/2} \cos(i) \tag{2.1}$$

Depending on the Tisserand parameter a comet can be classified into three categories:

- T_J < 2: Oort Cloud comets (e.g. Hyakutake)
- 2 < T_J < 3: ecliptic, Jupiter-crossing comets (e.g. 67P)
- T_J > 3: ecliptic, inside or outside Jupiter's orbit

2.1.3. Characteristics

The population distribution of objects that exist in large numbers and are in steady-state can be described by the power-law described by Equation 2.2. This formula applies to both asteroids and comets (Bottke et al., 2005).

$$N_>(R) \equiv \int_R^{R_{\max}} N\left(R'\right) dR' = \frac{N_0}{\zeta - 1}\left(\frac{R}{R_0}\right)^{1-\zeta} \tag{2.2}$$

Where $N_>(R)$ is the number of bodies with a radius larger than the given radius R, N_0 is the reference number of objects that exist with a known radius R_0, ζ is the slope of the curve, and $R_{\max}$ is the radius of the largest object in the system of bodies considered. For a system of bodies (e.g. the asteroid belt) to be in steady-state, it means that the population distribution does not change over time. For example, debris around a planet with an atmosphere would not be in steady-state as smaller objects are more easily slowed down and therefore deorbited. Collisions also play a significant role in the steady-state of a system as they can both form smaller bodies (two bodies collide and form many small bodies) and larger bodies (two bodies collide and form one larger body). For comets, fragmentation is also a key aspect of the steady-state equilibrium, this means that comets break apart, resulting in a larger quantity of smaller bodies. The value of ζ has been empirically calculated to be 3.5 for the asteroids in the main belt, and 2.5 for comets as it can be seen in Figures 2.4 and 2.5 (Tancredi et al., 2006). The orbital velocity of an object can be determined using the vis viva equation as seen in Equation 2.3 (Lissauer & de Pater, 2019, pp. 29-31).

$$V^2 = \mu\left(\frac{2}{r} - \frac{1}{a}\right) \tag{2.3}$$

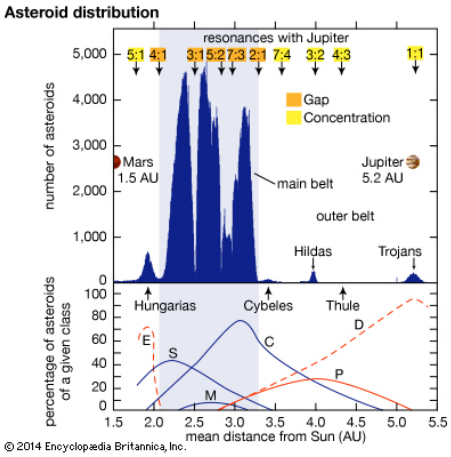

Figure 2.4: Asteroid sizes and their cumulative number. Debiased refers to the fact that all type of Main Belt Asteroids (MBA)s are represented in the plot. Image credit: Bottke et al. (2005)

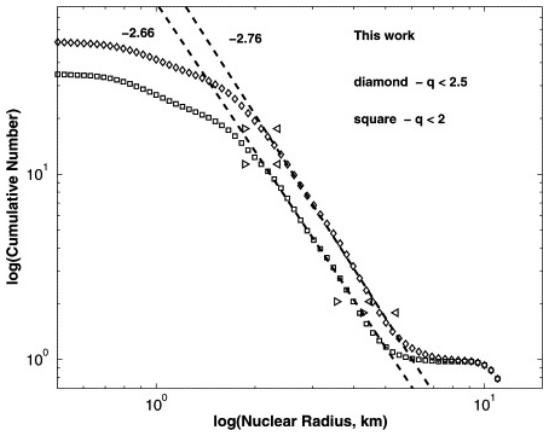

Figure 2.5: The cumulative size distribution of the sample of Jupiter-family comets with different cutting q-values. (Tancredi et al., 2006)

Where V is the orbital velocity,μ is the standard gravitational parameter of the parent body, r is the distance between the object and its parent body (e.g. the distance between the Earth and the Sun), and a is the semi-major axis of the orbit. Using the standard gravitational parameter of the Sun ($\mu_\odot = 132.712 \times 10^9\,\mathrm{km}^3/\mathrm{s}^2$) and the orbit of Saturn as radius ($r = 9.6\,\mathrm{AU}$), the orbital velocity for ecliptic bodies such as Centaurs or Kuiper-belt objects is around 12 km/s (semi-major axis $a = 30\,\mathrm{AU}$), while for isotropic objects such as Oort-cloud comets this velocity is around 14 km/s (semi-major axis $a \to \infty$) (Zahnle et al., 2003). The planetocentric orbital velocity can vary a lot depending on the planet's mass, but for Saturn, this velocity is between 5 and 8 km/s

To go from the orbital velocity of a body to the impact velocity on another body (excluding air drag) the two equations formulated by Horedt and Neukum (1984) can be used. Equation 2.4 can be used to calculate the impact velocity for a heliocentric object, while Equation 2.5 can be used to calculate the planetocentric impact velocity. In both these equations, μ_s is the satellite's standard gravitational parameter, R_s is the satellite's radius, U_p is the planet's relative velocity, and U_s is the satellite's relative velocity. While U_∞ is the encounter velocity in both cases, in Equation 2.4 it represents the velocity between impactor and planet, while in Equation 2.5 it represents the velocity between impactor and satellite.

$$V_{i,h} = \sqrt{\frac{2\mu_s}{R_s} + \frac{3\mu_p}{r_s} + U_\infty^2 + U_p^2 + U_s^2} \tag{2.4}$$

$$V_{i,p} = \sqrt{\frac{2\mu_s}{R_s} + U_\infty^2 + U_s^2} \tag{2.5}$$

Table 2.1 shows the various impact velocity for heliocentric and planetocentric impactors for some of the Jovian and Saturnian moons (Horedt & Neukum, 1984). The average time between impacts t_c is calculated using equations 2.6 and 2.7 for planetocentric and heliocentric impactors respectively, using the same values used to calculate the impact velocity.

$$t_{\mathrm{cp}} = 2\frac{\pi^2 l_s^{5/2} a^{3/2} U_\infty}{3GM_p R_s^2}\left(1 + 2\frac{GM_s}{R_s U_\infty^2}\right) \tag{2.6}$$

$$t_{\mathrm{ch}} = 2\frac{\pi^2 l_p^{5/2} a^{3/2} U_\infty}{3GM_S R_s^2}\left(1 + 2\frac{GM_p}{r_s U_\infty^2}\right) \tag{2.7}$$

Table 2.1: Mean impact velocities V_i for Heliocentric and Planetocentric projectile orbits of eccentricity e = 0.6 (Horedt & Neukum, 1984)

	V_i [km/s]		t_{ch} [years]	t_{cp} [years]
Object	Heliocentric	Planetocentric	Heliocentric	Planetocentric
Jupiter	N/A	N/A	7.14×10^6	N/A
Amalthea	46.3	12.3	1.32×10^{13}	3.14×10^3
Io	30.8	8.43	6.12×10^{10}	1.15×10^2
Europa	24.7	6.73	1.28×10^{11}	7.92×10^2
Ganymede	20.0	5.76	6.57×10^{10}	1.21×10^3
Callisto	15.7	4.52	1.25×10^{11}	9.51×10^3
Saturn	N/A	N/A	1.26×10^8	N/A
1980 S3	27.8	7.34	3.13×10^{14}	5.81×10^3
Mimas	25.2	6.65	3.55×10^{13}	1.11×10^3
Enceladus	22.3	5.86	2.77×10^{13}	1.65×10^3
Tethys	20.1	5.32	7.54×10^{12}	7.75×10^2
Dione	17.9	4.67	8.47×10^{12}	1.62×10^3
Rhea	15.4	3.99	6.11×10^{12}	2.76×10^3
Hyperion	9.86	2.35	3.76×10^{14}	2.82×10^6
Iapetus	7.25	1.63	2.63×10^{13}	2.18×10^6
Titan	10.624	3.70	1.558×10^{12}	1.293×10^4

2.2. Impact craters

Impact craters are the focus of this study. The crater anatomy is discussed in subsection 2.2.1, followed by the formation process in subsection 2.2.2. Finally, the section concludes by discussing the different types of craters in subsection 2.2.3.

2.2.1. Crater anatomy

Impact craters came in a variety of sizes and shapes, however, some features are characteristic of an impact crater and can therefore help recognize them. Hypervelocity impact craters usually have a rim around the cavity, which is where the crater diameter is measured as shown in Figure 2.6. On the outside of the crater, the ejecta can be found. This ejecta can create ”terraces” in larger complex craters. The crater cavity could be partially filled with impact melt and breccia along with other sediments deposited throughout the years. Some larger craters also have one or more central peaks as shown in Figure 2.6. The bedrock underneath the crater is often fractured as shown in Figure 2.6, which makes it possible to locate craters by gravity gradiometry (fractured bedrock is less dense than regular bedrock) as shown in Figure 2.7 (Pilkington & Grieve, 1992).

2.2.2. Crater formation

The crater formation event can be broken down into three main stages. These stages are defined by convention and are therefore somewhat arbitrary. The first stage is the contact and compression stage. This stage begins the moment the impactor touches the surface. At this point, the kinetic energy is transferred to the surface via shockwaves (Kieffer & Simonds, 1980). The compression of the shockwave can increase the pressure to hundreds of GPa, which is enough to melt, if not vaporize, rocks. This stage can last up to 2 s for faster impactors ($\approx$25 km/s) (Grieve, 1999). The second stage is called the excavation stage. This stage directly follows the first stage and generally lasts a few minutes. During this stage, material around the impact point is displaced in different directions. The shock waves create symmetric flow, where the material closer to the surface is pushed up, forming the ejecta curtain, and the material deeper down if further pushed down, compressing it even further (Grieve, 1999). The excavation stage is considered over once all the impact energy has been dissipated. The final stage is the modification stage. This stage has no clear end, however, it is considered to last a few hours. At the beginning of this stage, the transient crater (or transient cavity) is at its largest point and will begin to shrink as material falls back into the crater and the surface relaxes. After this point, the viscous

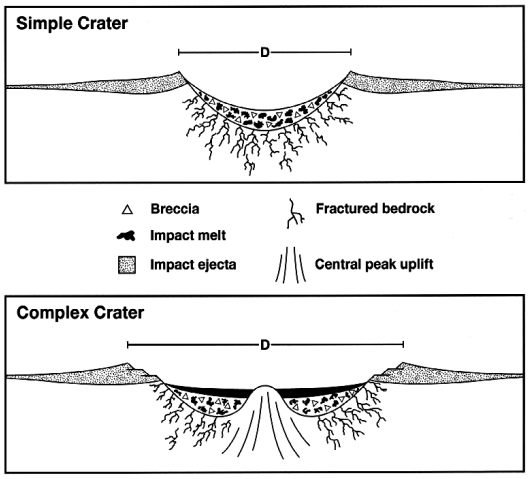

Figure 2.6: Impact Crater Structure of a simple crater (top) and a complex crater (bottom). Image credit: NASA.

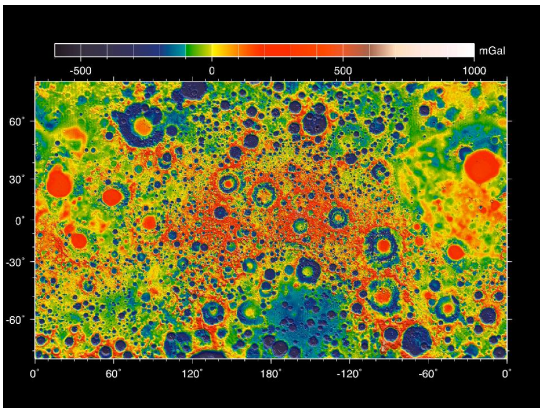

Figure 2.7: Lunar gravity field. Image credit: NASA.

relaxation stage begins. This is not a part of the crater formation, but rather what happens after the crater has been formed. This behavior is a consequence of the (semi)viscous nature of a planetary surface. Most analyses performed on surface viscosity approximate the actual flow as a Newtonian flow with effective viscosity η_{eff}. While this procedure is not exact and may result in misleading results, it is still very insightful (Melosh, 2011). Viscous relaxation acts to gradually erase any deviation from a leveled surface thereby acting to flatten said surface. Higher regions will be lowered and lower regions will be raised until equilibrium is reached.

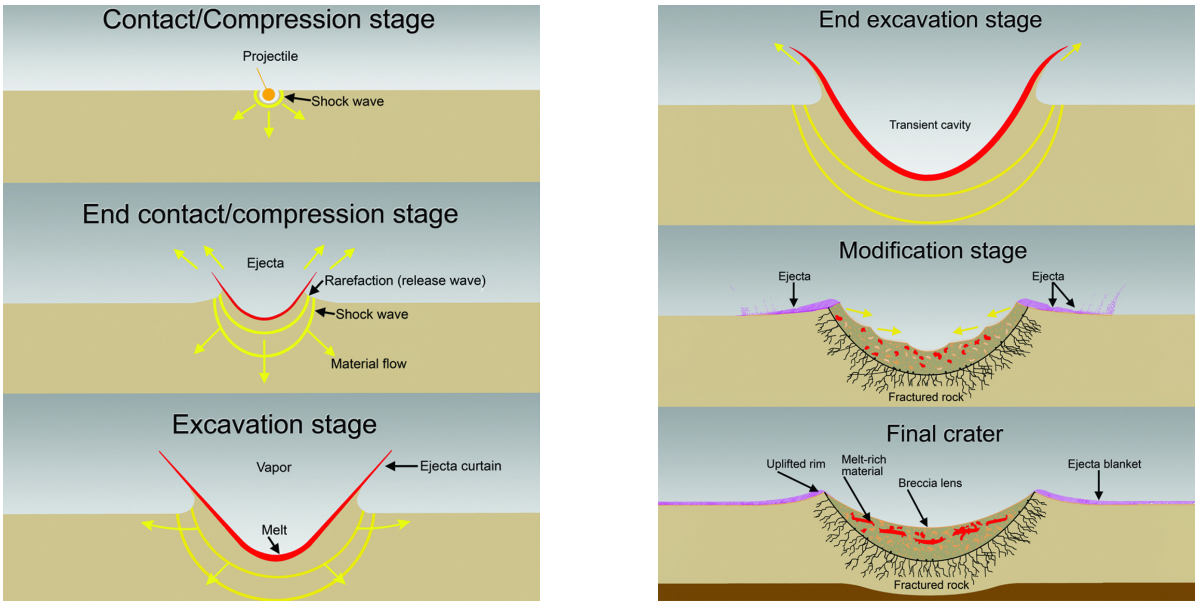

Figure 2.8: Development of a simple impact structure. (left) stages 1-3 (right) stages 4-6. Image credit (Kring, 2006).

2.2.3. Crater types

Craters are divided into three categories, based on their shape. Simple craters are the smallest of the three and present themselves as a bowl-shaped depression on the surface. The diameter of a simple crater can increase up to 20% compared to the transient crater diameter, due to minor collapse of the upper wall (Melosh, 1989). The bottom of these craters is usually filled with a mix of redeposited ejecta and debris fallen in from the rim. Complex craters are larger than simple ones and are characterized by a raised portion of the crater located at the center of the crater. This area is called an uplift region and

is the result of the interactions between shock wave effects, gravity, and rock strength. The transition between simple and complex craters occurs at a certain diameter size, based on rock strength and surface gravity. Based on their anatomy, three types of complex craters exist, central-peak, central-peak-basin, and peak-ring structures. The transition between these three types also varies based on gravity, surface density, and material strength proportionally to $c/\rho gh$. Where c is the transient material strength, ρ is the surface density, g is the surface gravity, and h is the depth of the transient crater. The third category is composed of multiring basins. These craters are the largest structures, reaching diameters of thousands of kilometers (Grieve, 1999). To qualify as a multiring basin, two or more concentric rings must be present. As these craters would require very large impactors, it is believed they were formed during the Late Heavy Bombardment (LHB) period, between 4.1 and 4.8 Ga ago.

2.2.4. Crater scaling

To scale craters from the lab setting to real-world scale, along with scaling between different surfaces, the dimensionless scaling method developed by Melosh (1989) and modified by Holsapple (1993) is used. This method consists of scaling different aspects of the impact crater according to the following equations.

$$\pi_D = D\left(\frac{\rho_t}{m_i}\right)^{1/3} \tag{2.8}$$

$$\pi_V = \frac{\rho_t V}{m_i} \tag{2.9}$$

$$\pi_2 = \frac{g}{v_i^2}\left(\frac{m_i}{\rho_i}\right)^{1/3} = 1.61\left(\frac{gL}{v_i^2}\right) \tag{2.10}$$

$$\pi_3 = \frac{Y}{\rho_t v_i^2} \tag{2.11}$$

$$\pi_4 = \frac{\rho_t}{\rho_i} \tag{2.12}$$

π_D is the scaled diameter, π_v is the scaled volume (also referred to as cratering efficiency), π_2 is the gravity scaled size, π_3 is the normalized strength (sometimes indicated as π_Y), and finally, π_4 is the density ratio. In the equations above D is the crater diameter, ρ_t and ρ_i are the target and impactor density respectively, m_i is the impactor mass, V is the crater volume, g is the gravitational acceleration of the planet/moon, v_i is the impact velocity, L is the diameter of the impactor, and Y is the yield strength of the target material. The volume V of the crater can be estimated with knowledge of the crater diameter D and depth d. Assuming the crater is a partial sphere, its volume is defined by Equation 2.13, where the ratio of d/D can be assumed to be between 0.25 and 0.33 for rocky craters (Melosh, 1989).

$$V = \frac{\pi D^3 (d/D)^2}{6}\left(3 - 2(d/D)\right) \tag{2.13}$$

2.2.5. Gravity dominated craters

Crater formation is divided into two main regimes, gravity-dominated and strength-dominated. Strength-dominated craters are craters in which expansion is driven by the strength of the target. Craters in this regime tend to be small and the target needs to have sufficient strength, such as rock or ice. Gravity-dominated craters, on the other hand, are craters in which expansion is driven by the gravity of the body. These craters tend to be larger or produced on loose a target surface such as sand or icy particles. Knowing whether or not a crater was formed the strength-dominated regime or in the gravity-dominated regime is very important as the crater scaling works differently between the two regimes as it can be seen in Figure 2.9 (Prieur et al., 2017). While knowing the exact transition between the strength regime and the gravity regime is hard (as it is not a hard transition), knowing the transition between simple and complex cratering (discussed in subsection 2.2.3) is much easier. Since the strength to gravity regime transition always occurs before the simple to complex transition, if a crater is a complex crater, it will be in the gravity-dominated cratering regime (Prieur et al., 2017).

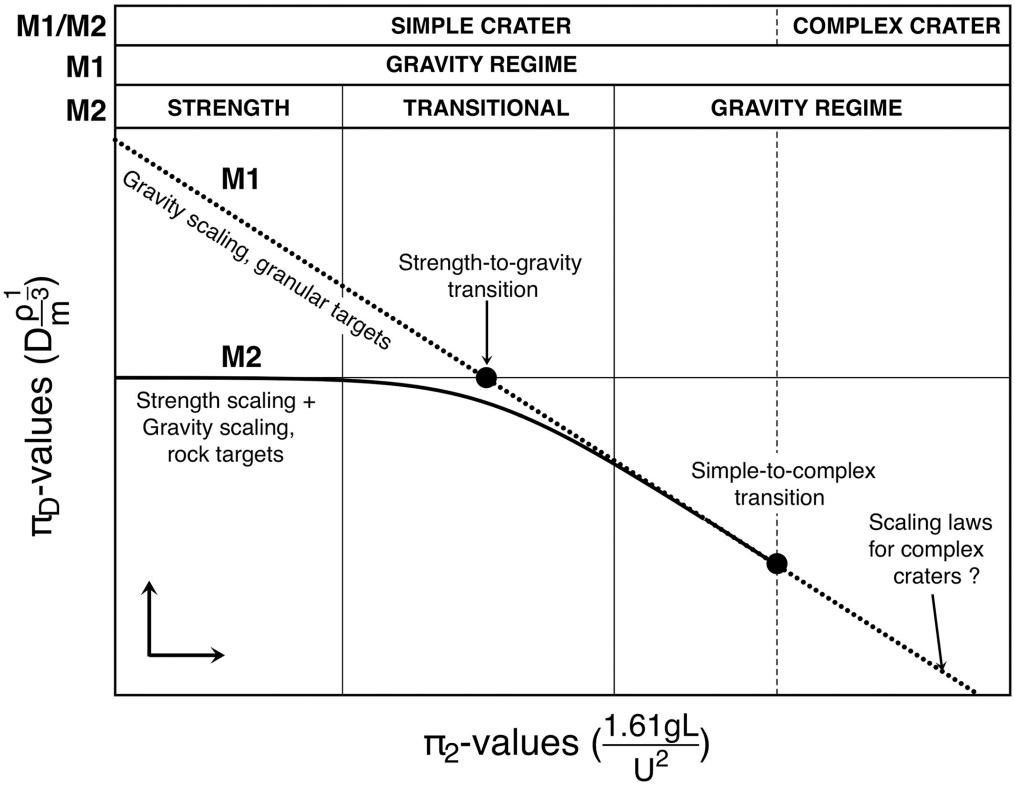

Figure 2.9: Transition between strength-dominated cratering and gravity-dominated cratering for impacts on rocky targets, along with gravity-dominated cratering for loose targets (Prieur et al., 2017).

2.3. Craters on icy moons

This section will give an overview of the necessary information for craters on icy moons, specifically for the Jovian and Saturnian systems. Subsection 2.3.1 briefly describes these two systems, subsection 2.3.2 briefly describes the heliocentric and planetocentric cratering models, finally subsection 2.3.3 describes the types of ices found on the icy moons.

2.3.1. Jovian and Saturnian system

Jupiter and Saturn are the two largest bodies in the solar system (other than the Sun), and they both harbor an extensive and interesting system of moons. Jupiter is the largest planet, with a mass of $318\,M_\oplus$, followed by Saturn with a mass of $100\,M_\oplus$. The moons orbiting these planets are just as fascinating, with some of them being almost as large as Mercury. Titan, a moon of Saturn, has an atmosphere thicker than Earth's, Io, a moon of Jupiter, has intense tidal heating, and many moons such as Europa (Jupiter II) or Enceladus (Saturn II) have subsurface oceans. These so-called icy moons are objects of great interest since some of them harbor liquid water under their surface, a key element in life as we know it. Both Jupiter and Saturn have ring systems, however, Saturn's rings are of particular interest due to their formation. One theory states that the rings are the remnants of one or more early moons that collided releasing debris, which eventually formed the rings (Ida, 2019). This theory is supported by the estimate of the rings' age given by Iess et al. (2019) of 10^7 to 10^8 years. This theory would be in favor of the planetocentric cratering theory discussed in subsection 2.3.2.

2.3.2. Cratering models: Heliocentric vs planetocentric

The heliocentric cratering model is what is believed to have formed most, if not all, of the craters in the inner planets and moons. Because of this, an estimate of the impact flux can be given throughout the age of the solar system. The most important information about this model comes from the samples returned from the Apollo lunar mission in the 1960s and 1970s. The current model includes a period in the first billion years of the solar system called the early bombardment era, where impact flux was high. The impact rate then decreased until around 3.8 Ga ago, when it picked up again. This period is called

the Late Heavy Bombardment (LHB) (Wetherill, 1975). This model should result in a curve similar to curve b in Figure 2.10, however, the exact shape of the curve is yet to be determined.

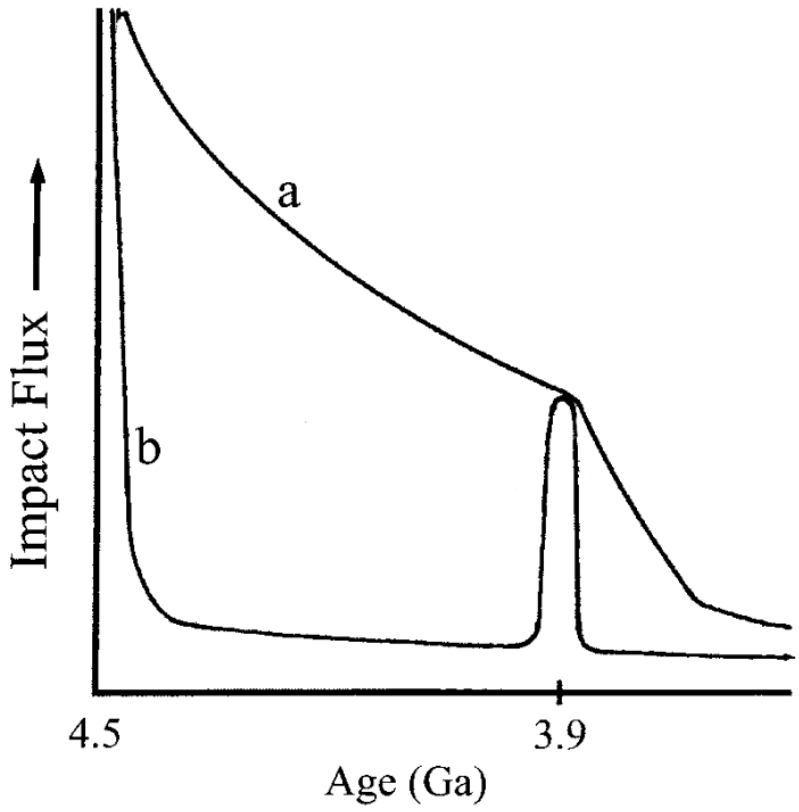

Figure 2.10: Schematic diagram showing possible evolution curves for the early impact flux at Earth, based on impact cratering data from the Moon (Kring, 2003)

The cratering rate for the planetocentric model is much harder to determine and would vary between different planets. Despite these difficulties, a relative cumulative crater number can be calculated for different moons. The following relationship was defined by Horedt and Neukum (1984).

$$N_0/N_1 = f_g \left(\frac{V_{i,1}}{V_{i,0}}\right)^{0.56p} \left(\frac{g_0}{g_1}\right)^{3p/16} \tag{2.14}$$

Where N_0 and N_1 are the cumulative crater number of the two moons, $V_{i,0}$ and $V_{i,1}$ are the impact velocities for the first and second impact, g_0 and g_1 are the gravitational accelerations of the two moons, p is the power-law exponent of the cumulative crater distribution, and f_g is the gravitational focusing parameter, determined by the following equation.

$$f_g = \frac{\left(1 + 2GM_p/l_{s,1}U_{\infty,1}^2\right)\left(1 + 2GM_{s,1}/R_{s,1}U_{h,1}^2\right)}{\left(1 + 2GM_p/l_{s,0}U_{\infty,0}^2\right)\left(1 + 2GM_{s,0}/R_{s,0}U_{h,0}^2\right)} \tag{2.15}$$

Where G is the gravitational constant, M_p is the planet's mass, l_s is the moon's orbit radius, U_∞ is the encounter velocity, M_s is the satellite's mass, R_s is the satellite's radius, and U_h is the relative velocity between planet and projectile at the border of the planet's gravitational sphere of action. However, the focusing effect of the satellite ($1 + 2GM_s/R_sU_h^2$) is negligible compared to the planet's one ($1 + 2GM_p/l_sU_\infty^2$) in Equation 2.15 (Horedt & Neukum, 1984). It must be noted that due to the very different nature of planetary impactors around two different planets, equations 2.14 and 2.15 are only valid to compute the relative cumulative crater number for the moons orbiting the same planet.

2.3.3. Types of ices

Different ice types exist in nature, each with its own morphology/characteristics. These different types of ice are formed at different pressure and temperature ranges and have different properties due to their different molecular structures as shown in Figure 2.12. Some types of ice are much more stable than others, which is why most ice types will revert to type I_c between 125 and 170 K and ice I_c will revert to I_h at 200 K (Bertie et al., 1964). Because of these properties, ice polymorphs should disappear in this order $VIII$ < (VI, V, IX) <II <I_c in icy craters (Gaffney & Matson, 1980). Therefore, ice types can be used to understand the history of the surface of an icy body. As an example, on Ganymede, the temperatures should be low enough above 70° in latitude for most of these types of ices to be stable under the surface. Therefore, the absence of these ice polymorphs could suggest some extra energy has been added to the surface, either continuously (internal source of heat) or abruptly (like a smaller impact), allowing the ice to revert to a more stable form. Ice can also form in its amorphous phase. When that happens,

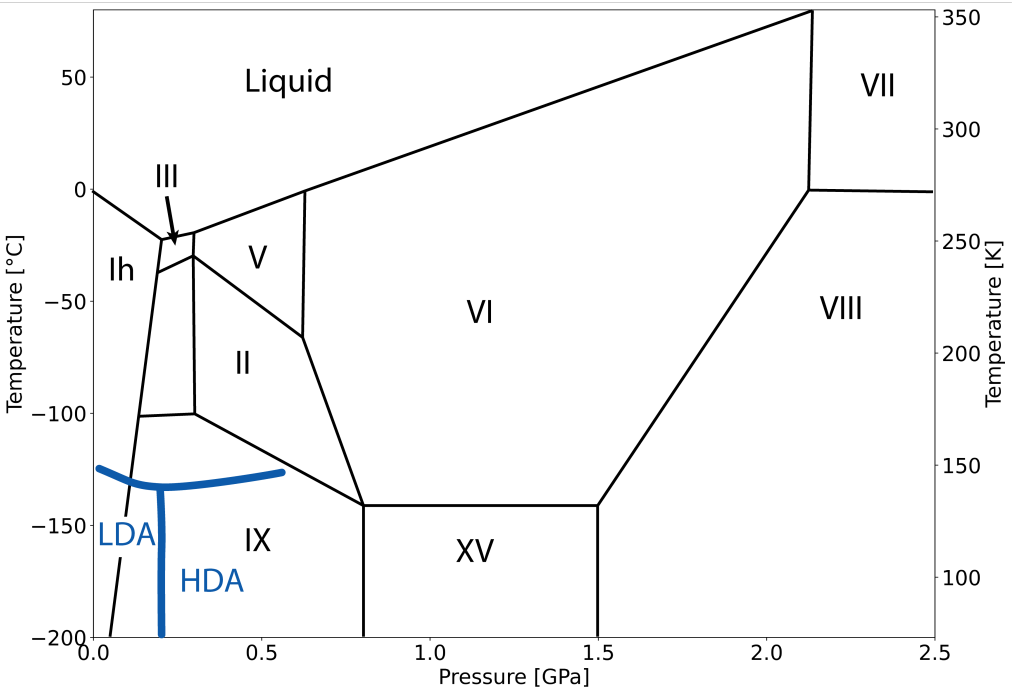

Figure 2.11: Phase diagram of water. Black lines indicate ice types, and blue line indicated region where LDA and HDA ice occur. Image obtained by combining figures provided by Tulk et al. (2019)

the molecules are not neatly aligned like for crystalline ice, resulting, among other things, in a lower density. This type of ice is formed when water rapidly cools below freezing, meaning the molecules do not have time to align themselves. Different types of amorphous ice exist, the two main ones being low density amorphous (LDA) and high density amorphous (HDA). This naming comes from the relative densities of the two ice types as both types of ice have their densities below 0.94 g/cm^3. However, the intrinsic density of the ice, without voids, is 0.94 g/cm^3 for LDA and 1.17 g/cm^3 for HDA (Mishima et al., 1984). This amorphous ice can only exist at very low temperatures as it begins transforming from LDA at 131(2) K and it becomes fully crystalline at 158 K (Jenniskens & Blake, 1994a).

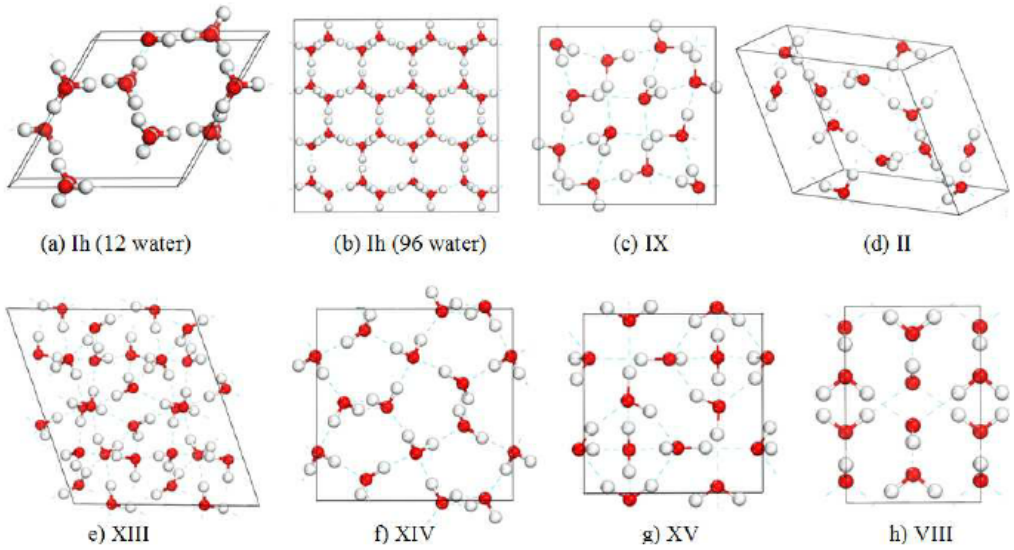

Figure 2.12: Molecular structure of different ice phases. Image credit: Santra et al. (2013)

2.4. Previous work

This section summarizes the work that has been done previously for planetary cratering. Subsection 2.4.1 briefly describes what has been done for rocky craters, while subsection 2.4.2 describes the research previously done on impacts on ice.

2.4.1. Rocky craters

Many different laboratory tests have been performed to reproduce impact conditions in the lab. Different researchers looked into different target materials, as well as different energy ranges to better understand the crater-making process and how these craters develop over time. Different materials could also be used to better reflect some particular aspect of the crater evolution, like in the research performed by Schultz et al. (2007). In their paper, Schultz et al. (2007) used many different materials to recreate six stages of the deep impact experiment. Powder pumice, along with sugar over ground perlite, were used to recreate the evolution of the ejecta shadow. Next, ground and sieved perlite were used to recreate the evolution of the ejecta and the flash before impact, along with sugar over ground perlite and pumice powder over ground perlite. A dolomite block was then used to recreate the formation of a vapor plume, followed by dolomite powder to study the evolution of the vapor plume. Layered targets were then used to better understand the excavation process and depth. To recreate the zone of avoidance (i.e. zone where no ejecta is found (Collins & Head, 1996)), perlite over sand was used, along with a combination of sand, perlite, and pumice powder. A summary of the experiments performed on rocky surfaces can be observed in Figure 2.13. The diameter and velocity of the projectile are plotted against each other, with the marker color representing the surface composition and the marker shape representing the projectile material.

2.4.2. Icy craters

Compared to research on rocky impacts, the research available for impacts on icy surfaces is limited. Figure 2.14 shows a summary of the previous research used in this study. The same data is detailed in Table 2.2, where the equations used to create the plots are used, along with the type of ice used for the experiments and the ranges of impact velocity and energy used for the experiments. Some of the ices used in the experiments are simple to make. For these types of ice, the description is provided in the table. These types of ice are usually ”commercial” ices, meaning that they are formed in large blocks at high temperatures (just below the freezing temperature) and with filtered water. This ensures the ice is clear and without cloudy sections. Shrine et al. (2002) describes how to form the ice. First, he boiled water for 30 minutes to get rid of impurities, then he placed the water in an ice bat at 277 K. He then transferred the water to a container with plastic sides and lid and an aluminum bottom. The water was kept in this container at 253 K for three days to ensure clear ice. Croft et al. (1979) used

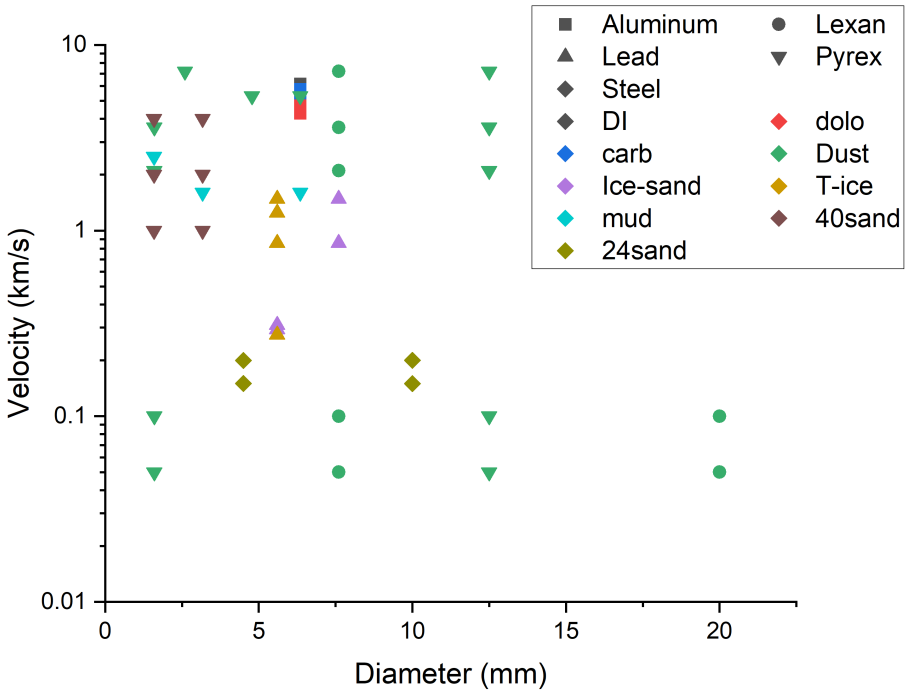

Figure 2.13: Impactor size and velocity distribution of past experiments. Marker color represent target surface type, while marker shape represents projectile composition. Adapted from: Tagliacarne (2021). Data obtained from: Cintala et al. (1985), Croft et al. (1979), Kawakami et al. (1983), Lange and Ahrens (1981, 1987), Shrine et al. (2002).

three different types of ice as it can be seen in Table 2.2. S-ice represents ice that is made by layering water and crushed ice at −70 °C. T-ice is the commercially available clear ice kept at −2.2 C. P-ice is composed of two slightly different types. One is made by compressing crushed ice until fusion, and the other is made by saturating a container filled with crushed ice (i.e. adding water to a container with crushed ice).

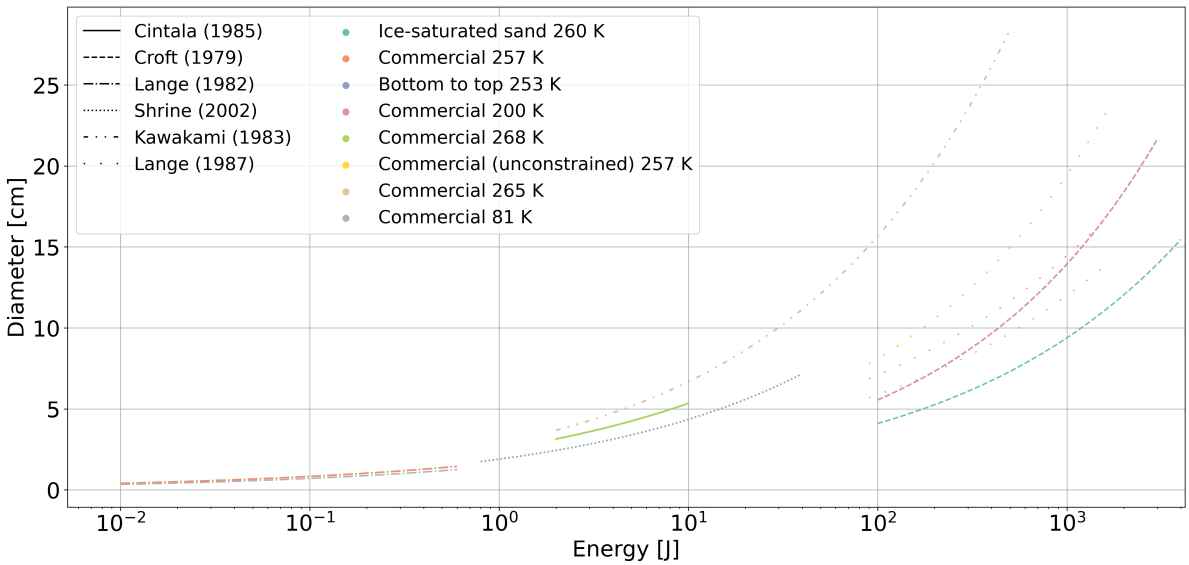

Figure 2.14: Summary of previous work, curves are shown for the energy ranges achieved during the experiments. Color indicates combination of ice type and ice temperature, while line type represents the paper the equation is from.

Paper	Ice	Velocity [m/s]	Energy [J]	Fitted equation [SI units]
Cintala et al. (1985)	Ice formed around 270 K and kept at 262 K before impact	185 - 415	2-10	$D = 2.5 \times 10^{-2} E^{0.33}$
Croft et al. (1979)	S-ice T-ice P-ice	300 - 1500	100 - 3000	$D \sim 8.8 \times 10^{-3} E^{0.4}$
Croft et al. (1979)	Ice-sand mix	300 - 1500	100 - 4000	$D \sim 7.8 \times 10^{-3} E^{0.36}$
Lange and Ahrens (1981)	Ice formed at 257 K	140 - 1050	0.01 - 0.6	$D = 1.7 \times 10^{-2} E^{0.31}$
	Ice formed at 81 K			$D = 1.48 \times 10^{-2} E^{0.32}$
Lange and Ahrens (1987)	Ice formed at 257 K, unconfined	150 - 640	90 - 1700	$D = 1.41 \times 10^{-2} E^{0.38}$
	Ice formed at 257 K, confined			$D = 1.70 \times 10^{-2} E^{0.31}$
	Ice formed at 81 K, confined			$D = 1.41 \times 10^{-2} E^{0.31}$
Kawakami et al. (1983)	Ice formed at 265 K	110 - 680	2 - 500	$D = 2.85 \times 10^{-2} E^{0.37}$
Shrine et al. (2000)	Ice formed at 253 K	1000 - 7300	0.8 - 39	$D \propto E^{0.30 \pm 0.04}$
Shrine et al. (2002)	Ice formed at 253 K	1000 - 7300	0.8 - 39	$D = (1.9 \pm 0.3) E^{0.36 \pm 0.04}$

Table 2.2: A summary of previous work focused on impacts on icy surfaces.

2.5. Knowledge gap

The age of the moons orbiting Jupiter and Saturn is unknown largely due to the uncertainty of the origin of the impactors of these icy moons, as the age of a planetary surface is often determined by counting impact craters and their sizes. From those numbers, the age of the surface can be determined according to a cratering rate model. However, the heliocentric and planetocentric cratering models result in very different relative ages for the moons as expressed by Bell (2020). One of the reasons for the uncertainty in cratering models is that not much is known about how the frequency and size distribution of planetocentric impactors. Another reason is that impacts on icy surfaces still contain large unknowns which result in large errors. These errors then lead to dramatic age estimate ranges like the one by Bell (2020) for Titan which can vary between ≈15 Ma and ≈4 Ga. Previous studies looked at impacts on ice blocks, however, these impacts might be in the strength-dominated regime, while impacts on icy moons are in the gravity-dominated regime. It is therefore important to analyze impact craters on a surface that allows replicating gravity-dominated craters on Earth. Therefore this thesis addresses the following research question to further expand upon our understanding of icy moons cratering mechanics.

> "Can the impact velocity be determined for impactors on icy moons based on crater characteristics, such as crater depth and diameter, by recreating impacts in the lab?"

This research question can be further broken down into the following sub-research questions.

1. What effect does impactor diameter have on the characteristic of the crater?
2. What effect does dampening have on impact craters?
3. Do different materials (e.g. sand, ice, etc.) result in different crater characteristics?
4. Can the depth to diameter ratio of craters be used to validate laboratory craters?
5. Can laboratory experiments be used to infer impactor diameter or velocity for impacts on icy moons?

3

Experimental Setup

Throughout this thesis, two machines are used, both located in the Delft Aerospace Structures and Materials Laboratory (DASML). The drop tower is used for impacts that require a horizontal surface for the sample and it has the advantage of higher impact mass while being limited to a maximum impact velocity of around 6 m/2. This machine is explained in section 3.1. For impact speeds up to 100 m/s the gas gun described in section 3.2 is used instead. Section 3.3 discusses the different containers used for all the experiments. Section 3.4 discusses the different targets and their respective preparation. Finally, the camera setup is discussed in section 3.5.

3.1. Drop Tower

This section discusses the drop tower configuration in subsection 3.1.1, how impact energy is estimated in subsection 3.1.2, and current challenges faced when dealing with the drop tower in subsection 3.1.3.

3.1.1. Drop tower configuration

In order to test materials that required a horizontal surface (e.g. soil), the drop tower shown in Figure 3.1 is used. This drop tower is capable of releasing an impactor from different heights ranging between 0.5 and 2.5 m. The impactor is composed of a rod of fixed weight (1.45 kg), a series of interchangeable tips (the part that impacts the sample), and a series of additional weights that can be combined together (to increase the impactor mass). This results in an impactor mass that can vary between 1.52 kg for the smallest tip and no additional weight, to approximately 5 kg for the largest tip and all the additional weights attached. This combination of varying height and varying impactor mass makes the machine fairly adaptable. The drop tower consists of several components as shown in Figure 3.1:

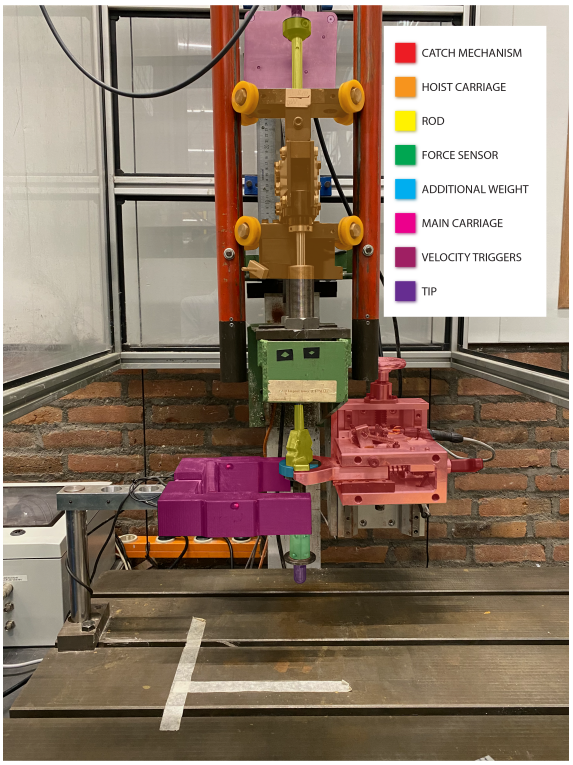

Figure 3.1: Drop tower at DASML. Different components shaded of different colors as per legend.

- **Catch mechanism:**
  Indicated in red in the figure. A C-shaped piece which is retracted before impact. Once the impactor passes the laser sensors, this metal piece springs forward and attempts to catch the impactor via two sections of the rod extending to the sides. These sections are wide enough that the C-shaped piece stops the impactor. When this works, only one impact occurs.

- **Velocity triggers:**
  Indicated in orange in the figure. A pair of laser sensors placed at a known vertical distance between each other. The time between each laser signal is interrupted is used to calculate the impact velocity. These two sensors also trigger the catch mechanism to release and catch the impactor.
- **Rod:**
  Indicated in yellow in the figure. The central piece that holds the tip, force sensor, and weights and magnetically attaches them to the carriage. The rod also allows for the impactor to travel vertically after being released from the carriage. The rod has a mass of 1.45 kg and contributes to the overall mass of the impactor.
- **Force sensor:**
  Indicated in green in the figure. The sensor which reads the impact force over time. Located just above the impact tip.
- **Additional weight(s):**
  Indicated in blue in the figure. These additional weights can be added to the impact rod to increase the impact mass (and therefore the kinetic energy). A list of these weights is provided in Table 3.2.
- **Main carriage:**
  Indicated in pink in the figure. The mechanism that allows the rod to follow the guide rails and fall straight down. Releases the rod about 300 mm above the impact point once it gets stopped by a pair of springs.
- **Hoist mechanism:**
  Indicated in light purple in the figure. The hoisting mechanism hooks to the main carriage, in turn attached to the impact rod, and hoists it up to the required drop height. This hoist mechanism is attached to an electric motor through a steel cable. The motor is not shown in the image as it is located below the table.
- **Tip:**
  Indicated in dark purple in the figure. The tip that impacts the sample. Can be easily switched to allow for different impacts. A list of all available tips is provided in Table 3.1 and two of them are pictured in Figures 3.2 and 3.3 (tip #6 and #11 respectively).
- **Height detector:**
  Not shown in picture. The drop tower has a sensor connected to the hoist mechanism which detects the drop height. This sensor allows to raise the main carriage to selected height automatically, however, the final height is always a few millimeters above the selected height (in the order of 10 mm on average).

ID	Mass [g]	Shape [-]	Outer-Diameter [mm]	Tip-Radius [mm]	Height [mm]	Cone Angle [deg]
1	69.0	spherical	20.1	10.05	40.1	-
2	171.0	spherical	30.1	15.05	40.3	-
3	250.5	spherical	37.5	18.75	40.1	-
4	281.5	spherical	40.1	20.05	40.1	-
5	412.5	spherical	50.1	25.05	40.3	-
6	545.5	spherical	60.1	30.05	40.2	-
7	114.5	cone	25	8	45.5	43
8	264.0	cone	37.6	4.5	52.6	64
9	241.5	cone	34	7	52.5	66
10	380.5	cone	40	12.5	51.85	77
11	86.5	bell-shape	25	5	39.9	-

Table 3.1: A list of all available drop tower tips and their characteristics.

ID	mass [g]	height [mm]
1	57.0	3.0
2	77.0	4.0
3	94.5	5.0
4	194.0	10.2
5	293.5	15.3
6	601.0	15.0
7	600.0	15.0
8	600.5	15.0
9	597.5	15.0

Table 3.2: Mass of the additional weights available for the drop towers.

Figure 3.2: Spherical tip, 545.5 g of mass. Top outer diameter of 60 mm and tip radius of 30 mm. Tip identifier #6.

Figure 3.3: Bell-shaped tip, 86.5 g of mass. Top outer diameter of 25 mm and tip radius of 5 mm. Tip identifier #11.

3.1.2. Impact energy

The impact energy of the impactor can be determined using the kinetic energy of an object as described by Equation 3.1.

$$E_k = \frac{1}{2} m_i V_i^2 \tag{3.1}$$

Where m is the mass, V is the velocity, the subscript i is for impactor, and E_k is the kinetic energy (of the impactor). The impact velocity is determined using the velocity triggers described in subsection 3.1.1 and the mass is determined by weighting the additional weights and the tip and adding that mass to the known mass of the rod (provided in the specifications of the drop tower). Since all the weights are known to a precision of 0.1 g, the error in energy is in the order of 0.1 mJ.

3.1.3. Challenges with drop tower

The first and most important issue of the drop tower has to do with the impact velocity. Due to limitations in the drop tower design, the maximum drop height is 3.1 m meaning that the maximum theoretical impact velocity is 7.8 m/s. This is several orders of magnitude below the ≈10 km/s indicated in Table 2.1. This theoretical maximum impact velocity does not even take into account energy losses due to friction, which would reduce the maximum theoretical impact velocity to around 6 m/s. While the low impact velocity can be compensated with higher mass to increase the impact energy, it remains one of the issues when experimenting with the drop tower.

The second issue, is the impactor shape, size, and overall impact method. As it can be seen in Figure 3.1, a large disk is present on top of the impact tip. This disk can influence the crater formation by impacting the surface. If that happens, the crater formed is considered invalid as it was formed in two separate moments by two different shapes and sizes of impactors. Since the impactor is attached to the rod, the rod assembly often bounces after impact and is forced back into the material, causing a second or third impact. While this should not happen thanks to the catch mechanism, it often happens as the bounce-back effect is too small for the catch mechanism to work properly.

The last issue is related to the catch mechanism. While most times it completely fails to catch the impactor sometimes it only partially fails meaning that the impact rod is pushed to the side by the catch mechanism as the mechanism hits the additional weights on the side trying to catch the rod. This means that not only there are multiple impacts, but the final impact also pushes the impact rod to the side, invalidating the result.

3.2. Gas Gun

This section discusses the configuration of the gas gun in subsection 3.2.1, the challenges faced when dealing with the current setup in subsection 3.2.2, and how the impact energy is calculated in subsection 3.2.3.

3.2.1. Gas gun configuration

To perform higher velocity impacts, the gas gun shown in Figure 3.4 has been used. The gas gun itself is composed by five main components as shown in Figure 3.4.

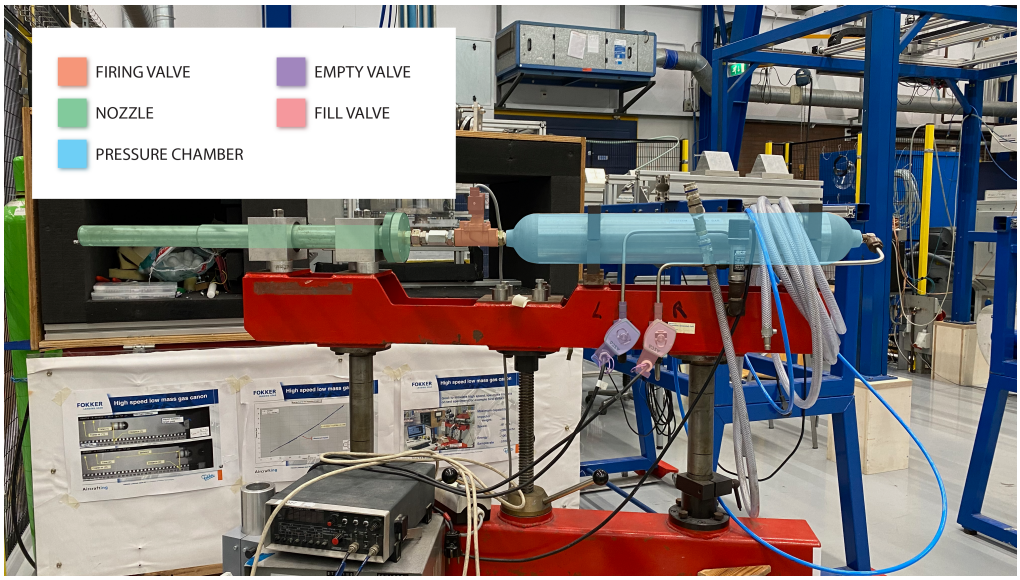

Figure 3.4: Mobile gas gun at DASML. Different components shaded of different colors as per legend.

- **Nozzle:**
  Indicated in green in the figure, it has a length of ≈800 mm and an inner diameter of 25 mm.
- **Pressure chamber:**
  Indicated in blue in the figure, the pressure chamber allows being pressurized up to 30 bar, which allows firing the projectile up to 100 m/s.
- **Firing valve:**
  Indicated in orange in the figure, the firing valve is what keeps the pressure chamber separate from the nozzle until the firing trigger is activated.
- **Fill valve:**
  The fill valve is what is used to fill the pressure chamber to the desired pressure using compressed air either from a central system (maximum pressure of 8 bar), or from a tank of compressed air (maximum of 30 bar).
- **Empty valve:**
  The empty valve can be used to either empty the pressure chamber without firing the gas gun or to slightly reduce pressure, in case the pressure chamber is overfilled.

3.2.2. Challenges with gas gun

The main challenge of the gas gun is the fact that it fires horizontally. This means that impact tests such as the ones on Martian regolith, cement, and icy particles cannot be performed as the target material would fall off. This is also an issue, albeit a smaller one, for ice blocks. That is because if the ice fractures, it risks falling off, meaning it is impossible to obtain a measure for the crater diameter. Gravity scaling relationships are also hard to determine as the gravity vector is pointing perpendicularly to the impact velocity vector instead of being parallel to it.

The second challenge is that the inner tube is 25 mm across, while the projectiles used have a maximum diameter of 8 mm. Two different approaches were attempted to solve this issue as described in subsection 3.2.4. At first, different sabot designs were tested, however, due to the many challenges, an inner acrylic tube with a diameter of 10 mm was used.

3.2.3. Impact energy

The impact energy of the impactor can be determined using the kinetic energy of an object as described by Equation 3.1. In this case, the impact velocity is determined using the high-speed camera as described in section 3.5. This setup results in a maximum measurement uncertainty of 3.9 m/s for a 100 m/s impact (or about 4% of the total velocity). The mass is calculated by weighting each projectile with a scale with an uncertainty of 0.001 g. The maximum impact energy uncertainty is 0.7 J or about 8% of the impact energy.

3.2.4. Projectile

Due to the difference between the projectile diameter and inner muzzle diameter, launching the projectile using the gas gun presented some challenges. To address these challenges, different means of shooting the projectile were attempted. The first one employed a sabot while the second one used an adaptor.

Sabot

A sabot is a means of shooting an oddly shaped projectile from a conventionally shaped muzzle. This method can also be used to shoot a smaller projectile without modifying the entire muzzle as is the case for these experiments. A sabot is typically composed of two halves with an outer shape compatible with the one of the muzzle and an inner shape compatible with the projectile that needs to be carried. The sabot used in these experiments has a familiar outer shape to best interface with the muzzle. The regions of smaller diameters as seen in Figure 3.5 are mainly there to reduce mass and shift the center of mass. Inside the sabot, a cutout can be seen, in the shape of a hemisphere the same size as the projectile. This would allow the projectile to be accelerated to the correct speed before being deployed. Unfortunately, the first iteration of this design did not work as planned as the two sabot halves do not have enough time to separate and release the projectile. Even in the rare occurrences where this happened, the two sabot halves still had considerable speed and impacted the sample, making the test invalid. A second version of the sabot shown in Figure 3.5 was tested. This version has a split-

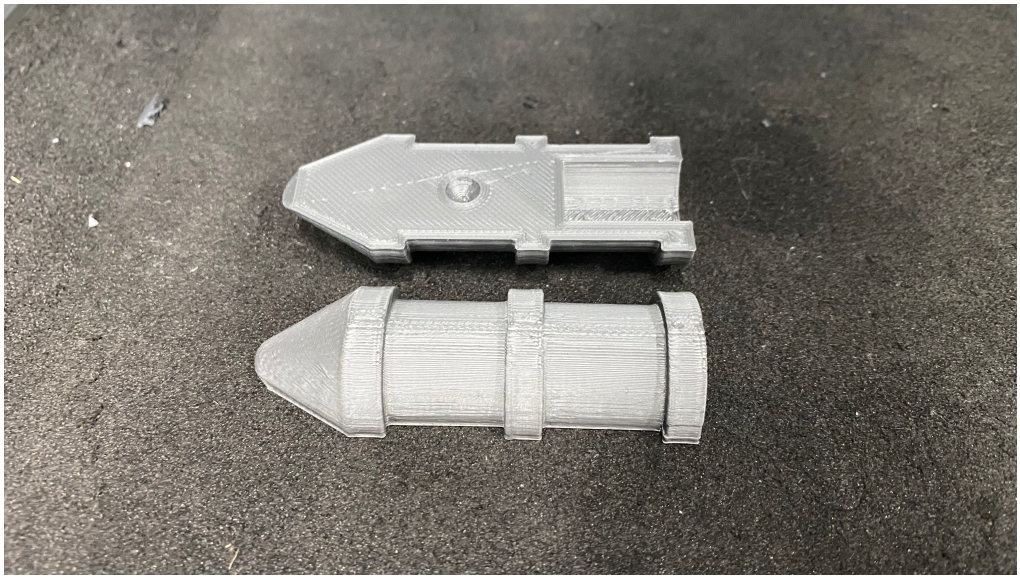

Figure 3.5: Second design of a 3D printed sabot used for this work.

tip and modified center of mass to allow for the two sabot halves to better separate and release the projectile. While this design successfully deployed the projectile most of the time, the two halves still

had too much velocity and kept impacting the target. Therefore, a new design was attempted and is described next.

Adaptor

To overcome the challenges of a sabot, the idea was discarded in favor of an adaptor design. This design consists of a 3D printed hollow cylinder containing an acrylic pipe as shown in Figure 3.6. The acrylic pipe is used to ensure a smooth surface where the projectile can freely travel, without the imperfections of a 3D printed surface. The outer cylinder is 3D printed as it does not have to be very strong and 3D printing allows for very cheap custom parts that take relatively little time to manufacture. The outer diameter of the 3D printed cylinder is 24.9 mm to match the 25 mm inner muzzle diameter. The inner diameter is 12 mm, to match the acrylic outer diameter. Finally, the acrylic inner diameter is 10 mm. This diameter is slightly larger than the maximum projectile diameter of 8 mm due to availability. The mismatch between the projectile diameter and inner tube diameter, resulted in lower top speeds, as upon firing, some air rushes past the projectile even going in front of it and slowing it down. Despite

Figure 3.6: Muzzle adaptor used for the experiments. Inner acrylic tube not pictured.

the diameter mismatch issue, this method was significantly more successful than the sabot and is what was used for all other experiments.

3.3. Containers

The different containers used in the experiments are discussed in this section. The order of the subsections represents the chronological order of when the container was first used.

3.3.1. Plastic container

The plastic container consisted in a trapezoidal container with base length of 116 mm, top length of 127 mm, and 50 mm height [1]. This container was discarded after one test as it broke apart.

3.3.2. Tall cylinder

This container was obtained by using a cylindrical strainer [2] with diameter of 113 mm and height of 130 mm. This strainer had holes, therefore the entire container was covered in painter's tape to ensure all the holes were completely closed. This container was only used for the first six tests and it helped understanding the volume requirements for the sample.

[1] https://www.ikea.com/nl/en/p/ikea-365-food-container-square-plastic-60452174/
[2] https://www.ikea.com/nl/en/p/ordning-kitchen-utensil-rack-stainless-steel-30131716/

3.3.3. Bowl

This container was obtained from an IKEA bowl [3] with an upper diameter of 210 mm, a lower diameter of 90 mm, and a total height of 85 mm. This container was used for a few experiments as it provided a large volume, however, it had to be discarded as its bowl shape made it unstable as soon as it was deformed.

3.3.4. Cylinder

The cylindrical container was obtained from a baking container with a diameter of 22 cm and a depth of 6.5 cm. Although of appropriate size, this container could not be used for ice experiments as it is not water-tight and the water would have leaked before freezing.

3.3.5. Square container

The container used in the drop tower experiments is shaped like an upside-down truncated pyramid (the bottom area is slightly smaller than the top area). The dimensions of the container are shown in Figure 3.8. A variation of the container adds a volume of insulating material (polyurethane foam) around the walls of the container as shown in Figure 3.7. This was done in an attempt to limit cooling from the sides to obtain a clear block of ice. If the ice is allowed to cool from the bottom of the container only, it will freeze from the bottom, allowing air and other impurities to escape to the top (Shrine et al., 2002). However, this method failed as the bottom of the container conducted heat to its sides, allowing them to cool the water.

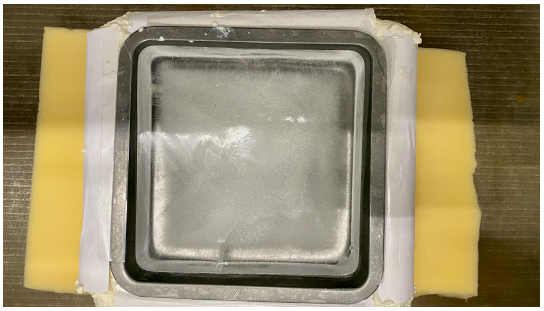

Figure 3.7: Square container, with insulating foam. Here pictured on top of the dampening foam.

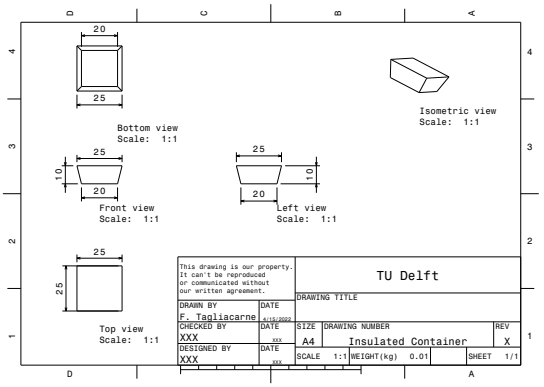

Figure 3.8: Schematics of insulated container. Full paige schematics available in Figure D.1.

3.3.6. Steel container

The final container used for the experiments was custom-made to satisfy all the requirements developed from experience with other containers and previous literature. The container needs to keep the test area temperature below 120 K until the sample is ready to be tested. This is necessary as the ice formed at 77 K will change its structure if heated above 122 K as described by Jenniskens and Blake (1994a). The container also needs to be strong enough to withstand impacts, as well as be able to fit in the drop tower and gas gun. Ideally, the container should also be repairable, as it would allow only part of the container to be substituted in case of damage. The results of these requirements (summarized below) is the container shown in Figure 3.9.

- **Depth:**
  The minimum depth of the container was obtained using the maximum crater depth obtained from craters on rocky surfaces, dividing that by 0.7 to obtain limit interactions with the container (Croft et al., 1979), and adding 5 cm to allow for the use of dampening foam on the bottom (to prevent damage to the container and insulate from the bottom). This resulted in a required depth of 18 cm which was then modified to 21 cm for ease of manufacturing.

[3] https://www.ikea.com/nl/en/p/klockren-double-boiler-insert-00455774/

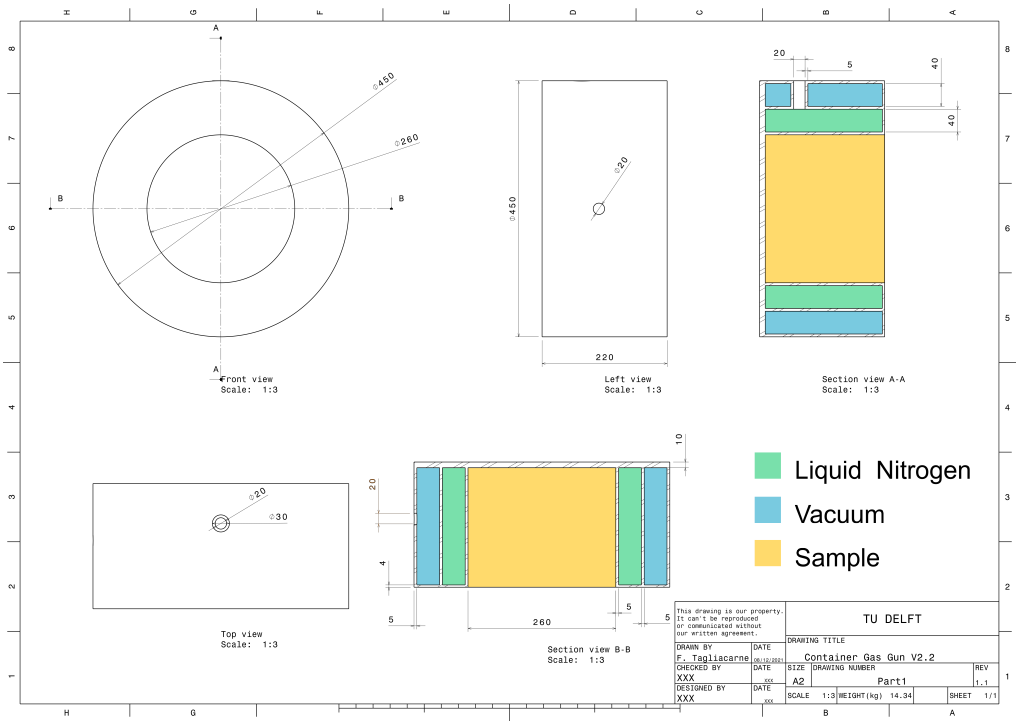

Figure 3.9: Schematic representation of container used in experiments with icy particles (full size image is shown in Figure D.2).

- **Diameter:**
  The minimum diameter was determined using the maximum crater diameter obtained from craters on rocky surfaces, along with the outer radius of the ejecta. The radius of the ejecta must be taken into consideration as the tall walls of the container would reflect ejecta back into the container which would modify the crater. The minimum diameter was estimated around 24 cm and modified to 26 cm for ease of manufacturing.

- **Temperature:**
  This container needs to hold icy particles formed at 77 K. These particles should be composed of a mixture of crystalline and amorphous ice, however, the structure will change if the sample is heated above 122 K (Jenniskens & Blake, 1994a). Therefore, the container needs to keep the sample below that temperature.

- **Repairability:**
  While this was not a primary requirement, making the container repairable means only part of the container should be replaced in case of damage, especially the bottom part which will be subjected to impacts.

This container is made up of three sections, indicated in blue, green, and yellow in the image. The blue section is pumped out of air to reduce the boil-off of the liquid nitrogen, placed in the green section. Finally, the yellow section is where the sample is placed to be tested. Additional insulating material can be placed on the bottom of the container to further reduce the heat flux from that side. The bottom of the container could not be designed as the sides as the risk of rupture during a test was too great. As it can be seen in Figure 3.9, the testing volume consists of a 26 cm inner diameter, and 22 cm depth. The size should allow for craters formed from impact energy up to 3000 J, and a depth up to 15 cm (Croft et al., 1979).

Contrary to all other containers used with the drop tower, this requires some modifications due to its size. The catch mechanism and velocity triggers must be removed to allow the container to fit under the drop tower. This means that the high-speed camera must be used to measure the impact speed. The removal of the catch mechanism also results in the impactor resting on the icy particles after the impact. To minimize melting of the particles the impactor must be quickly removed after each impact.

3.4. Targets

The four different targets used in these experiments, along with the preparation of these targets, are discussed in this section. The order of the subsections represents the order in which the samples were first used.

3.4.1. Martian regolith simulant

The martian regolith simulant used for the first round of experiments is the Mojave Mars Simulant 2 (MMS-2) [4]. This soil is designed to reproduce the chemical properties of Martian soil for agriculture-related research. However, it was immediately available and it possesses some features that make it an attractive candidate for impact crater testing like being a fine powder, similar to sand but with consistent grain size, something that would require sieving for regular sand. The second property is that MMS-2 does not clump, making it much easier to work with. For the experiments, the samples were simply prepared by gently pouring the simulant into the appropriate container, and gently mixing the simulant to allow for uniform density.

3.4.2. Cement powder

Cement powder was used after supplies of the MMS-2 ran out. Cement powder was chosen for three major reasons. The first two are that cement powder is inexpensive and easily accessible, meaning large quantities can be obtained, allowing for more tests to be executed. The third reason is that cement powder was used before, allowing to compare the results obtained in this study with the ones obtained by Vanzant (1962). Due to the clumping nature of the cement powder, the results of the experiments changed drastically depending on the compaction of the material (as described in section 5.2). Therefore the material had to be thoroughly and gently mixed once placed in the container, to ensure uniform distribution of material. An attempt was also made in determining the effect of compaction on the shear stress as described in subsection 5.1.2.

3.4.3. Ice blocks

The ice used in the experiments is obtained by filling a metal container as shown in Figure 3.7. The container filled with water is weighed before being placed in the freezer. The freezer is kept at temperatures between -22 and $-19\,°C$. The low temperature of the freezer, combined with the container characteristics (described more in detail in section 3.3) resulted in ice with a cloudy core enveloped by a clear shroud as seen in Figure 3.11. This cloudy core forms when ice cools rapidly, pushing all the impurities in the ice away from where the ice is freezing. Since the center is the last part that freezes, all the impurities (including air bubbles) are pushed in this volume (Seki et al., 1979). The creation of a

Figure 3.10: Cross-section picture of ice, where cloudy part is present.

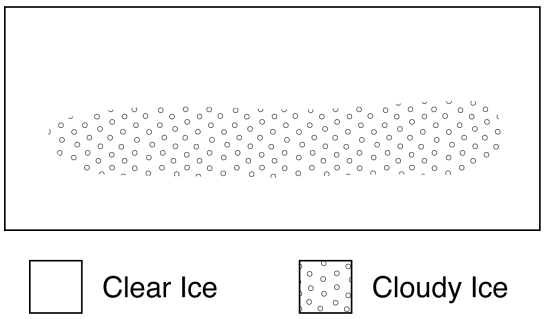

Figure 3.11: Cross-section representation of ice where cloudy part is present.

cloudy core results in significant structural differences in the ice, making that section of the ice weaker. The ice produced weighted between 700 and 1200 g, with a density around 900 kg/m^3.

3.4.4. Icy particles

Ice particles have also been used in the experiments instead of a block of ice. As it will be discussed in chapter 7, this type of surface is used to more closely resemble the conditions found on icy moons

[4] https://www.themartiangarden.com/mms2

(Le Gall et al., 2019). To prepare these icy particles, the method described by Gundlach et al. (2011) is used. This method consists of shooting water droplets in a container filled with Liquid Nitrogen (LN_2) as seen in Figure 3.12. This method rapidly cools the water droplets to 77 K (LN_2 boiling temperature) producing small ice particles. Once most of the LN_2 has evaporated, the ice particles are scooped into

Figure 3.12: Dewar container used to make ice particles.

a container used to keep them at a cold temperature, close to 77 K. A CAD drawing of the container in question is shown in the Figure 3.9. As it can be seen in the image, the icy particles are surrounded by LN_2, which is in turn surrounded by a (near) vacuum to slow boil-off.

3.5. Camera

The camera used in the experiments is a Photron NOVA S6 high speed camera capable of shooting at 1024 pixels $\times$ 1024 pixels at 6400 fps (PHOTRON, 2022). This camera is set up in two different ways for the two tasks it needs to achieve. For the drop tower, the camera does not need to record the impact speed, only the impacting process, meaning it can be placed looking at the surface at different angles to better understand the impact dynamics. Due to the lower impact speeds, the recordings for the drop tower are made at 6400 fps to allow for the maximum resolution. For the gas gun, the camera is placed perpendicular to the velocity vector, to compute the impact velocity with the greatest accuracy. To have more frames where the projectile is visible the frame rate for this setup is increased to 10 000 fps. Increasing the frame rate any further would reduce the image quality, making it unsuitable for obtaining any velocity information. In both setups, the camera is paired with a powerful LED light to increase the picture brightness which is needed for high-speed footage.

4

Verification & Validation

This chapter discusses the verification and validation procedures used throughout this thesis to ensure the data was measured correctly, and that the assumptions made do not yield incorrect results. First, the method of velocity measurement and assumptions made to use this method are verified in section 4.1. Finally, the results obtained with the ice blocks are compared against previous works for validation in section 4.2.

4.1. Velocity verification & validation

This section verifies and validates the method used to obtain the projectile velocity for the gas gun experiments. The assumption of constant velocity is verified in subsection 4.1.1 by analyzing the velocity change over the FOV of the camera. Then the estimated velocity measured by the high-speed camera is compared against the velocity measured by the drop tower in subsection 4.1.2. The drop tower uses a pair of laser sensors as discussed in section 3.1 which are more accurate than the high-speed camera measurements.

4.1.1. Constant velocity approximation

To know the velocity measured with the high-speed camera, an assumption is made that the velocity is constant while the projectile is within the field of view (FOV) of the camera. This assumption must be verified. The main forces acting on the spherical projectile are shown in Figure 4.1 and are drag, lift, and weight. As lift and weight operate in the vertical direction and the velocity vector is in the horizontal direction, only the drag is taken into account. The formula for the drag is given by Equation 4.1 (Anderson & Bowden, 2005), where C_D is the drag coefficient and is 0.47 for a sphere (Baker et al., 2012), ρ is the air density and is 1.225 kg/m^3 (Anderson & Bowden, 2005), V_i is the projectile velocity and can range between 40 and 100 m/s for the gas gun, and A is the surface area perpendicular to the airflow and can be calculated from the formula for the area of a circle from the radius, which comes out to about 5.03×10^{-5} m^2 for a sphere with diameter of 8 mm.

$$D = C_D A \frac{1}{2} \rho V_i^2 \tag{4.1}$$

From Equation 4.1 the change in velocity can be obtained and results in the equation below (see section E.1 for full derivation).

$$\Delta V = \frac{1}{2} \frac{C_D A}{m} \rho V_i \Delta x \tag{4.2}$$

Since the FOV of the camera is at most 20 cm, the change in velocity can be calculated to be 0.142 m/s in the worst-case scenario (highest V_i recorded by camera). This change in velocity is less than 0.2% of the impact velocity (for any V_i assuming all other parameters are the same) which is negligible, especially when compared to other measurement errors as mentioned in subsection 4.1.2.

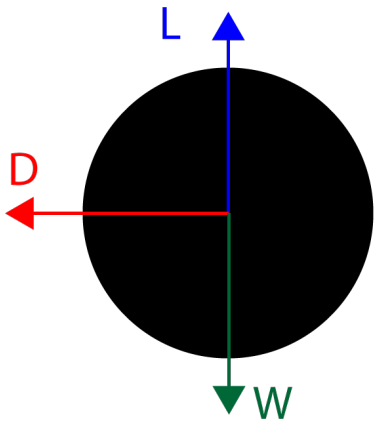

Figure 4.1: Free body diagram of a sphere flying through air.

4.1.2. Velocity validation

To ensure the velocity measured by the high-speed camera is accurate, an object moving with a known velocity can be recorded, and its speed measured by the high-speed camera. While there is no such object with such a predictable speed, the drop tower has a much more accurate method of measuring the velocity, the laser sensors discussed in subsection 3.1.1. Therefore some drop tower tests were recorded and their velocity was measured by the drop tower laser sensors to be compared to the ones obtained by the camera measurements.

The data from several drops are shown in Figure 4.2, where it can be seen that the velocity is within the 1σ uncertainty of the velocity measured by the lasers. These three measurements have a measurement error between 2 and 8% which is significantly higher than the 0.2% discussed in subsection 4.1.1. The measurement uncertainty is similar for drops #44 and #45 (8 and 5% compared to 7.5 and 3% respectively), however, for drop #46 it is significantly higher than the 5% error as the uncertainty is around 25% of the measured velocity. While this uncertainty is high, the calculated value for the velocity is within the measured value when including the 1σ uncertainty. This means that using the 1σ uncertainty is sufficient when estimating the error. For the experiments done with the gas gun, this uncertainty is at most 4.5% which is better performance compared to these three tests, most likely due to the much higher velocities making small errors in measurement less significant.

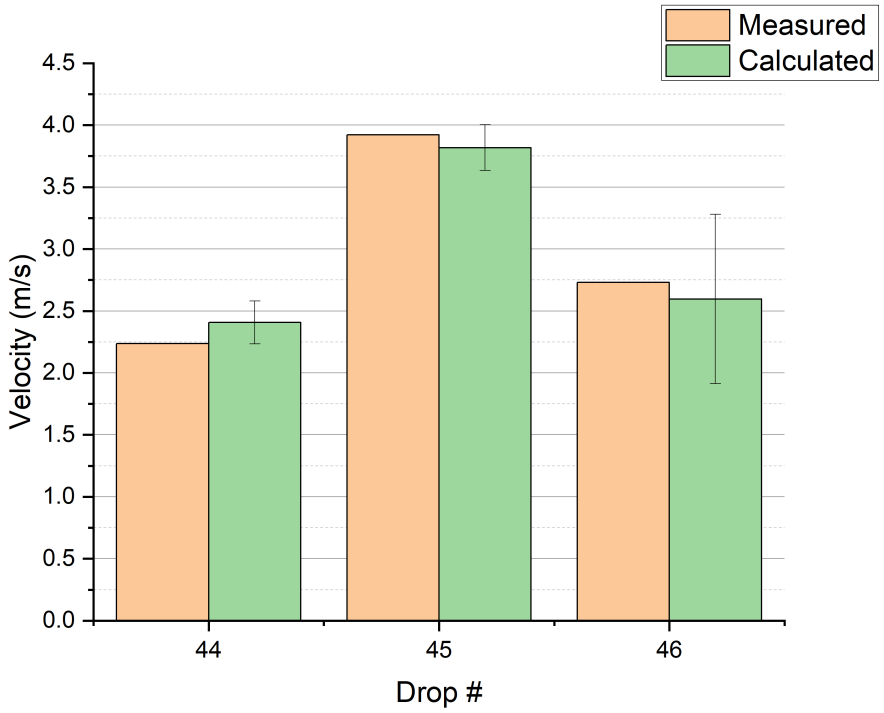

Figure 4.2: Velocity measured by the drop tower (taken as the actual speed) vs the calculated speed (as estimated from the high speed camera).

4.2. Ice blocks experiments validation

The data obtained during the experiments performed on ice throughout this work can be compared to data obtained from previous studies on impacts on ice blocks to validate the experiments. As it can be seen in Figure 4.3 all but a couple of the data points obtained in this work lay below the lowest curve from previous work within the given energy range (Shrine et al., 2002). Part of this difference is explained by the presence of dampening foam in most of the experiments performed in this work. As this foam absorbs some of the energy of the impact, the resulting crater diameter will be smaller. An argument could also be made that while the scaling laws are made from a specific range of energies, they should be valid throughout all energy regimes, so long as the craters are either gravity constrained or strength constrained in both cases. As the craters formed by the drop tower are gravity constrained meaning that in theory the scaling relationships found by other papers could be extended to the range of this work. Doing so reveals that the craters obtained by this work are above the one predicted by Croft et al. (1979) as it can be seen in Figure 4.4. This means that the data produced is valid when expanding the energy ranges of previous works to include the range of this thesis.

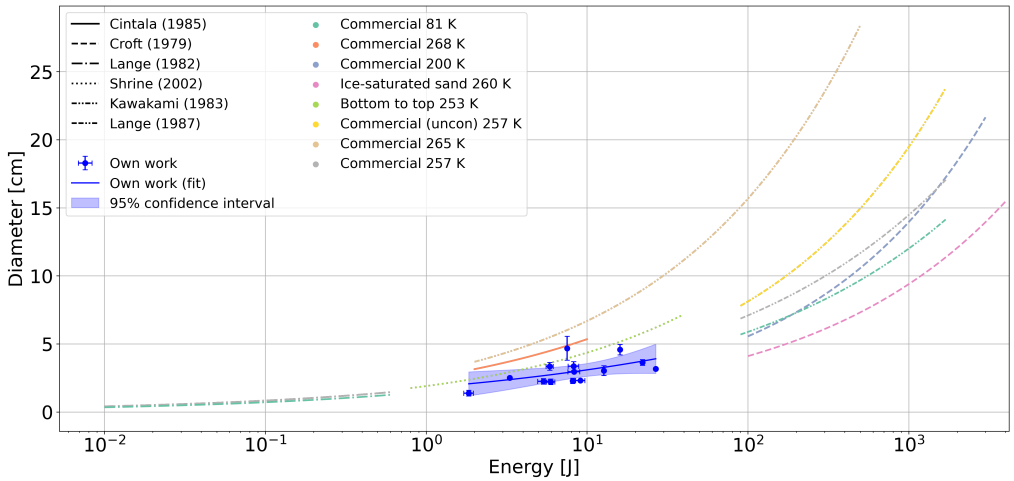

Figure 4.3: Data obtained by impacts in this work alongside best fit equations for previous papers.

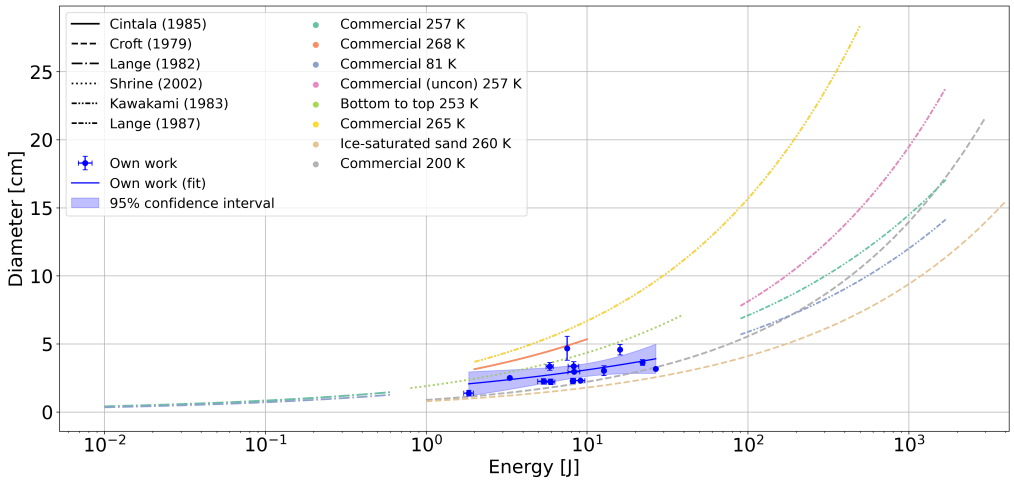

Figure 4.4: Data obtained by impacts in this work alongside best fit equations for previous papers. Ranges for estimate provided by Croft et al. (1979) extended to include energy range of this work.

4.3. Shattering energy verification & validation

In subsection 6.2.1 the shattering energy per kilogram of material is estimated based on the results obtained from the experiments. Later, in section 7.5 this energy is used to estimate whether or not the surface of an icy moon would shatter upon a certain impact (see section 7.5 for a full explanation of how to estimate this). When estimating the shattering energy per kilogram of material in subsection 6.2.1 it is assumed that the entire sample is involved in the impact. For material to be involved in the impact it means that it is within the shock wave produced by the impact. To validate the assumption that the entire sample is involved in the impact, the mass of the material involved in the impact can be calculated and plotted against the actual mass.

Alternatively, the required shattering energy can be plotted against impactor diameter. This is done in Figure 4.5 where three main components can be seen. The points in the plot are obtained from the impact results in ice, where the radius is the radius of the impactor and the energy is the impact energy. The points labeled as *broken* indicate the ice blocks which broke apart as they were unconstrained and should not be classified as being shattered. Then, for each shattering energy (26 J/kg and 52 J/kg) two curves are shown. One for the projected required shattering energy if the sample had (effectively) infinite mass (shown with a dashed line), and one for the required shattering energy considering that the sample has a mass, which cannot be exceeded (shown with a continuous line). Therefore, when the continuous line flattens out, it means that the material involved in the impact is the entire sample. From Figure 4.5 the shattering prediction can also be seen. If a point is above a line, it means that

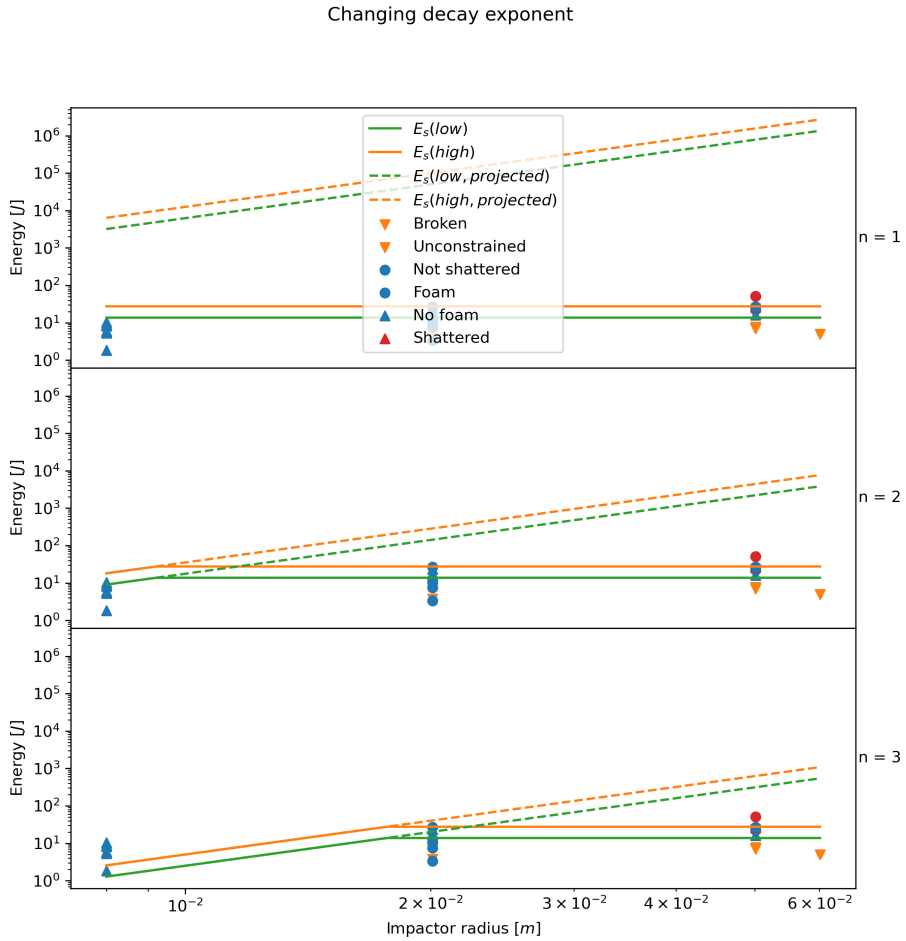

Figure 4.5: Estimated shattering energy for impact experiments in ice with energy of each impact. E_s is the required shattering energy for a given impact radius, *high* and *low* in parenthesis refer to the two different shattering energies per kilogram of material, and *projected* refers to the required shattering energy if the sample was large enough for the shock wave to fully dissipate (i.e. involved mass not capped by sample mass).

according to the model the ice should shatter.

The two instances of shattered ice are in the flat region of the curve for any value of n, meaning that the assumption that the entire sample is involved in the impact can be considered verified. Both points are also above their respective shattering lines for each value of n, meaning that according to the model the ice should have been shattered which validates the model. In Figure 4.5 for $n = 3$, the model estimates that the ice should shatter for impacts with the gas gun which is not what is observed, meaning that the exponent n should be below 3.

5

Craters in rocky surfaces

This chapter covers all the experiments performed on rocky surfaces. This includes the experiments done on MMS-2 and cement, along with the experiments done to measure the yield strength of cement. First, the way the experiments were carried out is described in section 5.1. Then, the results obtained by all the experiments are explained in section 5.2. Finally, these results are discussed in section 5.3. The discussion section also compares the results obtained to previous work to see what the differences are and what can be learned from these experiments.

5.1. Methodology

This section describes how the experiments on rocky surfaces are carried out. First, subsection 5.1.1 describes the experiments performed in MMS-2. Subsection 5.1.2 then describes the setup for the experiments performed to measure the yield strength (via the shear stress). Finally, the experiments performed in cement are described in subsection 5.1.3.

5.1.1. MMS-2

A total of 20 experiments were performed with MMS-2. These experiments served to understand the capabilities of the drop tower, as well as which containers were suitable for the experiments. The first test was done in the plastic container described in subsection 3.3.1 with a bell-shaped tip shown in Figure 5.1 and an additional 601 g. The drop height was set to 1.0 m and ended up being 1.002 m.

The next batch of tests consisted of six experiments in the container described by subsection 3.3.2. The same set-up as for the first test was used for the first five of these six tests. The actual drop heights ranged between 1.002 m and 1.019 m. For the last experiment in this container, a different tip was used. This tip is the smallest spherical tip with a tip radius of 10.05 mm. The actual drop height for this experiment was 1.015 m (the drop height was set to 1.0 m for all these tests).

The next batch of experiments consisted of 10 experiments using the bowl-shaped container described in subsection 3.3.3. For these experiments the tip was kept the same (small spherical tip) and the impact energy was modified by changing the additional masses between 601 g and 1201 g, and by changing the drop height between 0.5 m and 1.5 m in steps of 0.5 m (i.e. 0.5-1.0-1.5 m). The actual drop heights of these experiments varied between 0.508 m and 1.519 m.

The last three experiments used either the square container as described by subsection 3.3.5, or a cylindrical container as described by subsection 3.3.4. These three experiments used the two additional weights for an additional mass of 1.201 kg. These three experiments used a different spherical tip, one with the same radius as the disk on top of the tip mounting point (i.e. 25.05 mm). The drop height was varied between 1.0 and 1.5 m, where the actual heights were 1.002 m, 1.018 m, and 1.019 m.

5.1.2. Shear stress

To test the yield strength of the bulk material, the cone indentation method described by Moore (1965) is used. This method relies on inserting an inverted cone with angle 2α and mass m in the bulk material and measuring the penetration depth h. For small angles of α, the normal stress on the walls of the cone is negligible compared to the shear stress, meaning the method estimates the yield strength.

Figure 5.1: Bell-shaped tip, 86.5 g of mass. Top outer diameter of 25 mm and tip radius of 5 mm. Tip identifier #11.

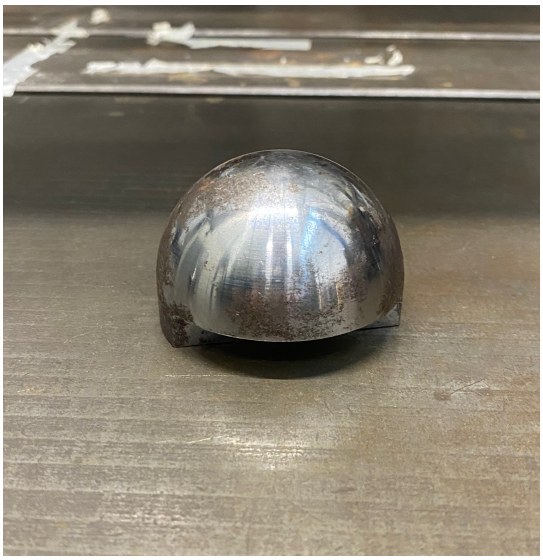

Figure 5.2: Spherical tip, 545.5 g of mass. Top outer diameter of 60 mm and tip radius of 30 mm. Tip identifier #6.

Figure 5.3: Equipment used for cone indentation (numbers are identifiers used in tables 5.1 and 5.2).

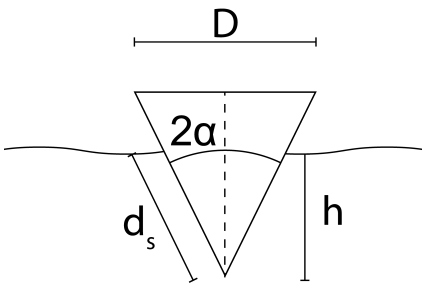

Figure 5.4: Graphical representation of the setup for the cone indentation experiment.

However, this does mean that this method tends to overestimate the shear stress (Fink et al., 1982). The shear stress, and therefore yield strength τ, can be measured according to the following formula.

$$\tau = \frac{mg \cot \alpha}{\pi h^2} \tag{5.1}$$

The vertical penetration depth is obtained using the following formula:

$$h = d_s \cos(\alpha) \tag{5.2}$$

Where d_s is the penetration depth as measured on the side of the cone.

In order to measure the required values, the equipment shown in Figure 5.3 is used. This includes a set of seven penetration cones with characteristics described in Table 5.1 and a set of four weights (number four not pictured) as described by Table 5.2. The extra weights are needed as the 3D printed cones are very light (from ≈1 g to ≈10 g) which would result in a small penetration depth making a successful reading challenging.

ID	α [deg]	$\tan(\alpha)$ [-]	mass [g]
1	10	0.18	0.9
2	15	0.268	1.52
3	20	0.36	2.63
4	20	0.35	3.82
5	25	0.5	2.42
6	30	0.58	5.367
7	45	1	10.22

Table 5.1: Details of penetration cones, $\tan\alpha$ is design value, α is an approximation.

ID	mass [g]
1	14.06
2	13.65
3	14.04
4	217.3

Table 5.2: Mass of the weights used to aid in the measurements.

5.1.3. Cement

A total of 22 experiments were performed on cement, all with the square container described in subsection 3.3.5. All 22 experiments also used the same, 50.1 mm spherical head, and an additional mass of 1.201 kg composed of two weights of 0.6 and 0.601 kg. The first five tests were done with little regard to the compaction of the material. Due to the results obtained after these tests, a series of 16 tests (plus an invalid one) were performed. These tests included four sets of four experiments. Each set had a constant compaction pressure and the drop height was varied between 0.5 and 2.0 m in steps of 0.5 m. The first test of the batch had to be repeated twice as the sample was not prepared correctly, hence 17 tests were performed instead of 16. The compaction pressure was applied before each experiment by placing an object of known mass m on a plate of known area A. The pressure was then computed as

$$p = \frac{mg}{A} \tag{5.3}$$

Where g is the gravitational acceleration (9.81 m/s^2). After each drop, the sample was slowly stirred to remove any compaction left by the compaction pressure and the impact and to remove the crater itself. Slow mixing was required to ensure the sample was not compacted in the process. After mixing, the new experiment could be prepared.

5.2. Results

This section illustrates the results obtained from the experiments explained in section 5.1. An overview of the craters produced from impacts in MMS-2 and cement is provided in Table 5.3. First, subsection 5.2.1 discusses the results obtained from the experiments in MMS-2. This is then followed by the results of the shear stress measurements in subsection 5.2.2. The section concludes with the results obtained from the experiments in cement in subsection 5.2.3.

- **Broke container**:

- COntainer was held by device which allows for deflection of the bottom of the container (i.e. bottom of container is not in contact with the table). The force from the impact was too large and it broke the bottom of the container.

- **Crater too deep**:
  If the final crater depth is more than 70% of the sample depth, the crater is declared invalid as according to Croft et al. (1979) the results produced by such crater are unreliable. This issue also includes craters which depth is the same as the sample depth, as it is an extreme case of the same issue.

- **Container moved**:
  Upon impact, the container either slid sideways or wobbled due to its hemispherical shape. This movement agitates the sample after impact, making the crater invalid.

- **Wrong compaction**:
  When testing the behavior of cement at different compaction pressures, the compaction pressure

had to be carefully controlled before impact. When this was not the case, the crater was deemed invalid as it was not useful for that series of experiments.

ID	Surf.	Cont.	m_i g	d_i mm	V_i m/s	E_i J	D mm	Outcome
1	M2	TP	2137.3	25	3.75	15.1	N/A	Invalid. Broke container.
2	M2	TC	2137.3	25	3.68	14.4	60	Valid.
3	M2	TC	2137.3	25	3.64	14.2	55	Valid.
4	M2	TC	2137.3	25	3.90	16.2	55	Valid.
5	M2	TC	2137.3	25	3.96	16.8	61.5	Valid.
6	M2	TC	2137.3	25	4.00	17.1	N/A	Valid.
7	M2	TC	2119.8	20.1	3.74	14.8	N/A	Valid.
9	M2	BL	2119.8	20.1	5.03	26.8	74	Invalid. Crater too deep.
10	M2	BL	2119.8	20.1	3.65	14.1	N/A	Invalid. Crater too deep.
11	M2	BL	2119.8	20.1	3.55	13.4	66	Invalid. Crater too deep.
12	M2	BL	2119.8	20.1	2.74	7.94	N/A	Invalid. Crater too deep.
13	M2	BL	2719.8	20.1	4.54	28.0	N/A	Invalid. Crater too deep.
14	M2	BL	2719.8	20.1	3.85	20.2	69	Invalid. Crater too deep.
15	M2	BL	2719.8	20.1	4.62	29.0	N/A	Invalid. Crater too deep.
16	M2	BL	2719.8	20.1	4.85	32.0	N/A	Invalid. Container moved.
17	M2	BL	2719.8	20.1	3.79	19.5	90	Valid.
18	M2	BL	2719.8	20.1	2.30	7.21	75	Invalid. Crater too deep.
19	M2	SQ	3063.3	50.1	3.39	17.6	45	Valid.
20	M2	CY	3063.3	50.1	4.60	32.4	60	Valid.
21	M2	CY	3063.3	50.1	4.33	28.7	70	Valid.
22	CM	SQ	3063.3	50.1	4.50	31.0	120	Valid.
23	CM	SQ	3063.3	50.1	4.43	30.0	90	Valid.
24	CM	SQ	3063.3	50.1	5.32	43.3	N/D	No data retrieved.
25	CM	SQ	3063.3	50.1	4.5	31.0	80	Valid.
26	CM	SQ	3063.3	50.1	5.1	39.8	70	Valid.
27	CM	SQ	3063.3	50.1	3.01	13.9	52	Invalid. Wrong compaction.
28	CM	SQ	3063.3	50.1	2.97	13.5	66	Valid.
29	CM	SQ	3063.3	50.1	3.86	22.8	72	Valid.
30	CM	SQ	3063.3	50.1	5.30	42.9	125	Valid.
31	CM	SQ	3063.3	50.1	5.73	50.3	152	Valid.
32	CM	SQ	3063.3	50.1	2.36	8.54	75.5	Valid.
33	CM	SQ	3063.3	50.1	3.47	18.4	76	Valid.
34	CM	SQ	3063.3	50.1	4.40	29.7	95	Valid.
35	CM	SQ	3063.3	50.1	5.44	45.4	135	Valid.
36	CM	SQ	3063.3	50.1	2.30	8.10	69.5	Valid.
37	CM	SQ	3063.3	50.1	3.77	21.7	73	Valid.
38	CM	SQ	3063.3	50.1	4.59	32.3	80.5	Valid.
39	CM	SQ	3063.3	50.1	5.31	43.2	86	Valid.
40	CM	SQ	3063.3	50.1	2.23	7.61	51.5	Valid.
41	CM	SQ	3063.3	50.1	3.77	21.8	51	Valid.
42	CM	SQ	3063.3	50.1	4.33	28.8	50.5	Valid.
43	CM	SQ	3063.3	50.1	4.93	37.3	52.5	Valid.

Table 5.3: Experimental parameters, crater diameter, crater depth, and experiment outcome for impacts on rocky surfaces. Surface: M2 is MMS-2 and CM is cement. Container: TP is tupperware, TC is tall cylinder, BL is bowl, SQ is square, and CY is cylinder. N/A is for not applicable (e.g. no crater diameter due invalid crater) while N/D is for no data for when a measurement was not taken. For a more comprehensive logbook see Appendix A.

5.2.1. MMS-2

The first experiment in MMS-2 broke the container holding it, resulting in a large part of the sample flowing out of the container and did not produce a viable crater. Drops #2 through #7 were performed in the tall cylindrical container described in subsection 3.3.2, and all produced craters with diameters around 55 mm, which is just slightly more than the diameter of the disk on top of the impactor tip.

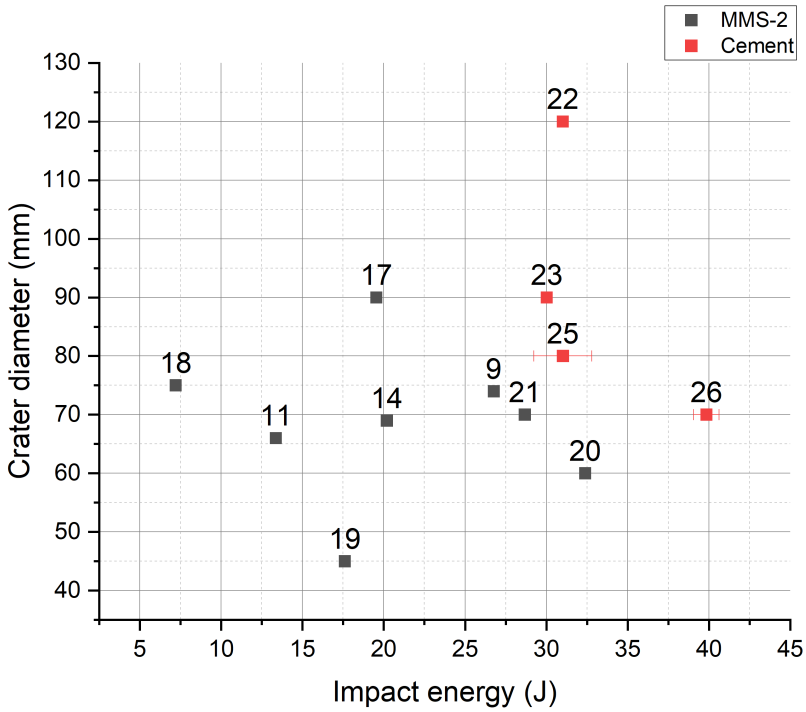

Figure 5.5: Results of drops 9 through 26 for drops. Grey squares indicate drops performed on MMS-2, while red squares indicate impacts on cement powder.

Drops #9 through #18 were performed in the bowl-shaped container described in subsection 3.3.3. Of these ten tests the first seven (#9 to #15), along with the last one (#18), were performed on a sample layer too thin to produce an accurate crater, all creating craters between 65 and 75 mm, regardless of impact energy. Therefore only two tests were performed with an adequate amount of material. Of these, the impactor hit the container off-center in drop #16, causing the container to wobble during impact, effectively ”resetting” the surface right after crater formation. Drop #17 produced a good crater 90 mm across. The crater diameters that could be collected are shown in Figure 5.5 to show how little effect the impact energy had on crater diameter.

The last three drops done with MMS-2 (#19 to #21) were performed with a larger tip as described in subsection 5.1.1. This, along with a thick enough layer, resulted in good craters being formed, with a general trend of larger craters with larger impact energies.

5.2.2. Shear stress

The results of 14 out of the 16 experiments discussed in subsection 5.1.2 are shown in Figure 5.6. Two of the data points were removed as the sample was compressed before measuring, resulting in a different density than the one reported. Despite removing these two data points, some results indicate a shear stress of around 3000 Pa and some indicate a shear stress of 6000 Pa and higher. Therefore, estimating the shear stress solely using the sample volume is not a viable option.

5.2.3. Cement

The first five experiments in cement were done with little regard for compaction as stated in subsection 5.1.3. The first two drops produced a valid crater, however, due to a failure in the drop tower

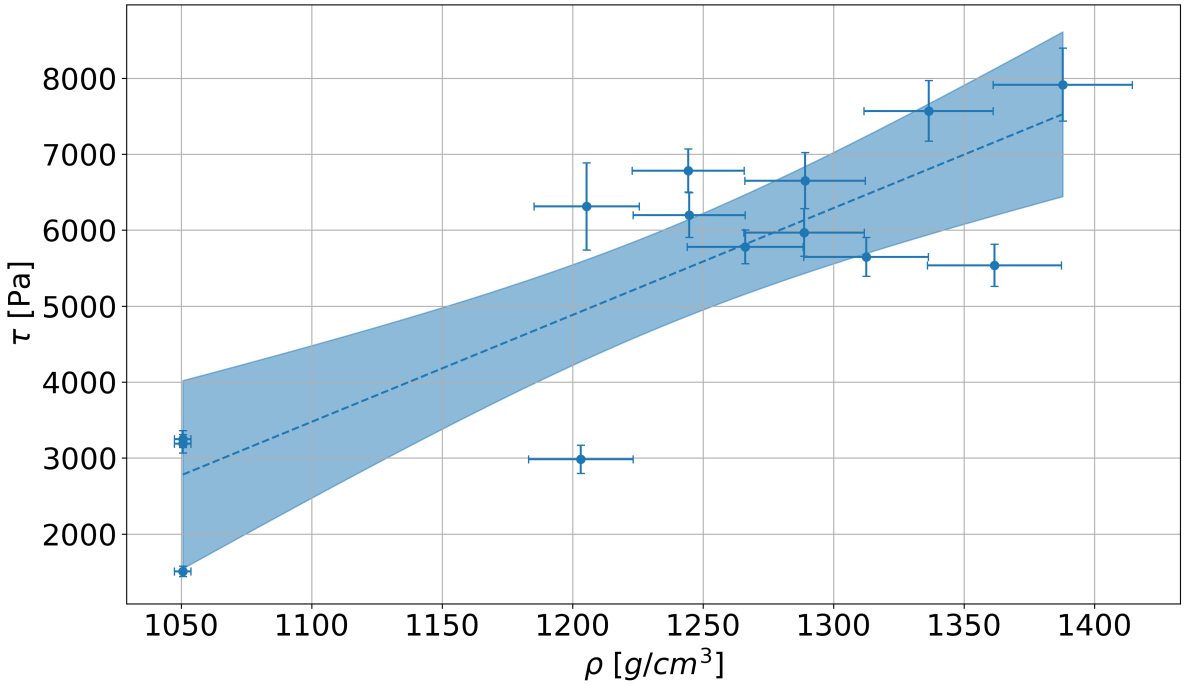

Figure 5.6: Filtered results of shear stress measurement. (Two points were removed as the were invalid.)

system, the impact velocity was not measured for the fourth and fifth drops (#25 and #26 respectively). Their velocity can be estimated using all other data obtained from the drop tower, where the impact velocity is found to be 4.5(8) m/s and 5.1(4) m/s for drop heights of 1.5 m and 2.0 m respectively. Drop #24 did not yield any useful data as the crater diameter was not measurable. The results of the four experiments can be seen in Figure 5.5. From this figure it can be seen that impacts with similar energies have very different diameters, and increasing the energy, as with drop #25, results in a smaller diameter, instead of a larger one. This behavior can be attributed to the lack of consistency in the compaction of the material, where procedures designed for MMS-2 were used for cement.

The first experiment of the next batch was supposed to be a no compaction drop from 0.5 m. However, after the impact, it was clear that something had gone wrong in the preparation of the sample as the cement appeared more compact than expected. Upon revision of the sample preparation strategy, it was discovered that shaking the sample resulted in unwanted compaction. The preparation procedure was therefore updated for the next 16 drops to prevent such issues from occurring again. The results of the 16 experiments are shown in Figure 5.7. The results of the 16 tests in cement can be seen in Figure 5.7, where four curves are plotted, one for each compaction pressure. Those curves represent the best-fit curves obtained by fitting the data to Equation 5.4.

$$D = aE^b \tag{5.4}$$

As it can be seen from Figure 5.7, increasing the compaction pressure flattens the curve, up to the point where for the highest compaction pressures (12 891 Pa) the crater diameter remains almost constant around 50 mm, approximately the diameter of the impactor. This is valid even for the two lowest compaction pressure, where the crater diameters for zero pressures are smaller than for 242 Pa. While this behavior cannot be fully explained, one reason could be that when the compaction pressure is very low, it has a negligible effect, meaning that the difference is only due to measurement errors. The fit equations are provided in Figure 5.7 and reported in Table 5.4 along with the results for π scaling as described in subsection 2.2.4.

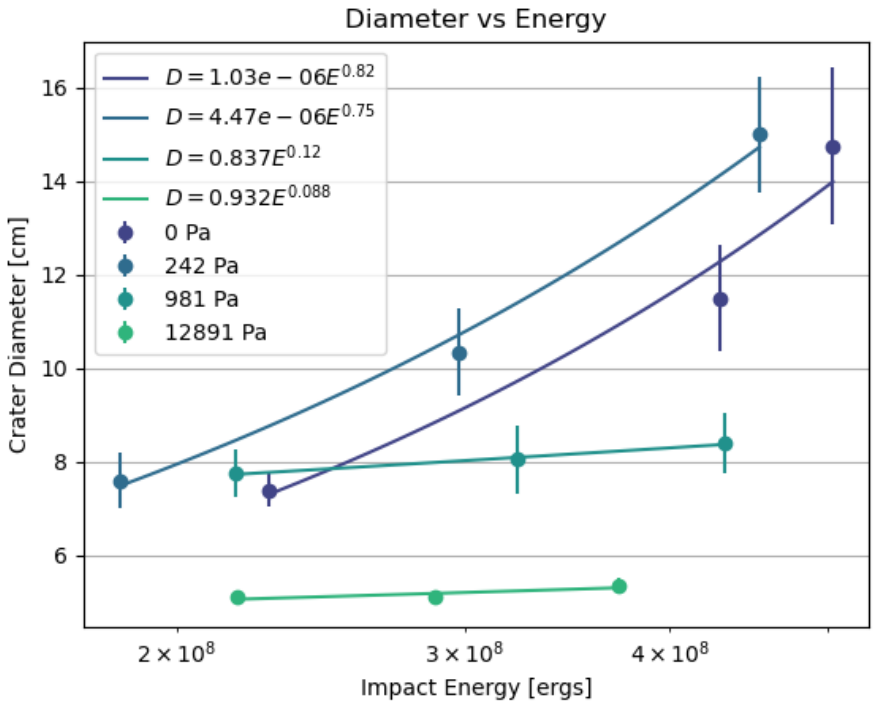

Figure 5.7: Impact energy compared to crater diameter for the 16 impacts in cement.

Compaction [Pa]	D vs. E	π_V vs. π_2
0	$D = 1.03 \times 10^{-6} E^{0.82}$	$\pi_V = 1.71 \times 10^{-5} \pi_2^{-2.4}$
242	$D = 4.47 \times 10^{-6} E^{0.75}$	$\pi_V = 5.28 \times 10^{-5} \pi_2^{-2.2}$
981	$D = 0.837 E^{0.12}$	$\pi_V = 0.009\,08 \pi_2^{-0.35}$
12891	$D = 0.932 E^{0.088}$	$\pi_V = 0.003\,77 \pi_2^{-0.27}$

Table 5.4: Best fit equation for experiments in cement.

5.3. Discussion

Most previous experiments done in cement powder do not deal with compaction. The ones that do use the yield strength of the material as a variable, instead of the compaction pressure. Therefore the results will be compared to the data obtained by Gault et al. (1974) and Vanzant (1962) and a qualitative comparison of the behavior of the material will be done with the results obtained by Richardson et al. (2007). The values of a and b, as defined by Equation 5.4, found by Gault et al. (1974) are 10^{-2} and 0.31 respectively, and the values found by Vanzant (1962) are 6.2×10^{-3} and 0.37 respectively. This comparison can be seen in Figure 5.8, where both the data points and best-fit curve are shown. From the figure, the points are located above the curves predicted by previous work. Looking closer at the curves, it can be seen that the predicted crater (for other works) diameter is below 50 mm for the given impact energy range. Since the impactor has a diameter of 50.1 mm, it is impossible for the craters to have such small diameters. It is therefore possible that decreasing the impactor diameter would result in a smaller crater diameter for the same energy. Along with the absolute value of the curves, the exponent of the curve is also important as it describes how the crater behaves with increasing energy. Using this metric, it can be seen that increasing the compaction decreases the exponent which results in a flatter curve. Unfortunately, none of the equations match the ones provided by either of the two previous studies. However, looking at the curves for the three lowest compaction pressures, it can be seen that the values for b found in previous works are between the ones found in this work, suggesting that with the right compaction pressure a similar curve could be replicated.

Figure 5.9 shows the same curves shown in Figure 5.7 but plotted using π scaling as described in

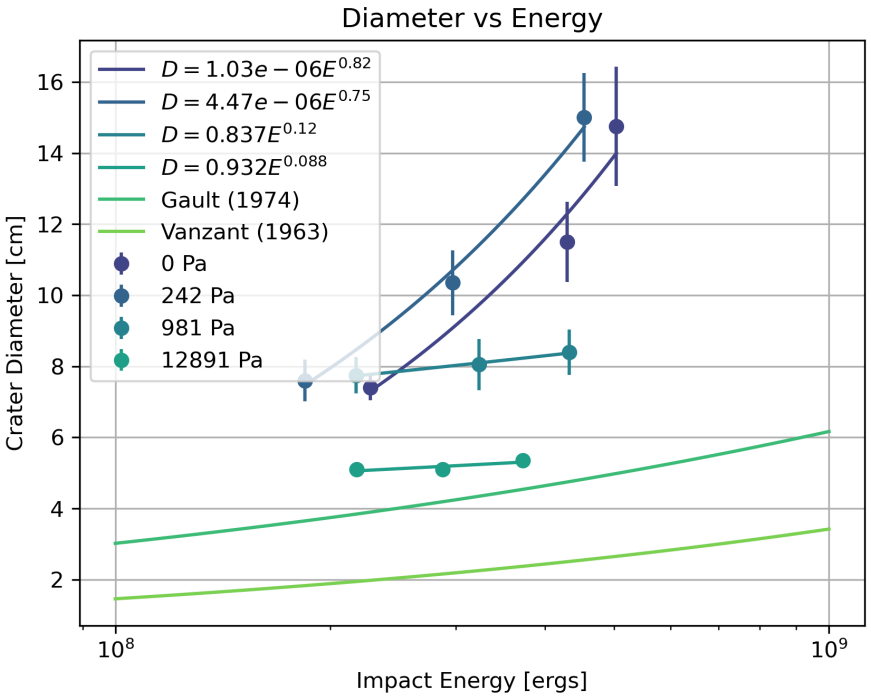

Figure 5.8: Comparison of data found by this work to the one found by Gault et al. (1974) and the one found by Vanzant (1962)

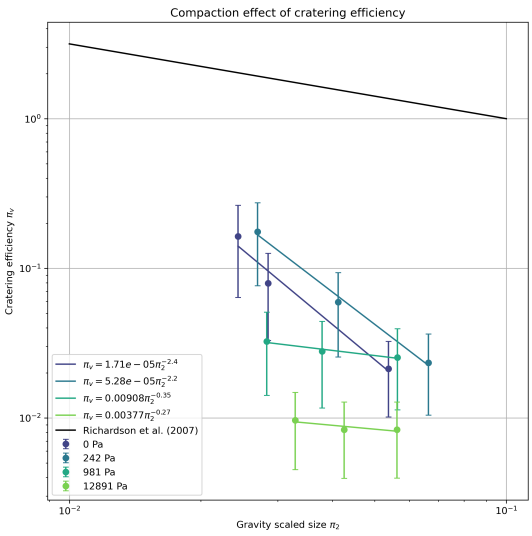

Figure 5.9: Gravity-scaled size Π_2 compared to cratering efficiency Π_V.

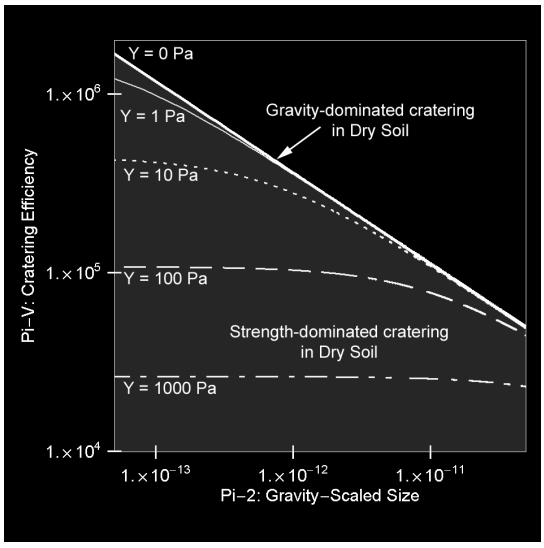

Figure 5.10: Gravity-scaled size Π_2 compared to cratering efficiency Π_V as found by Richardson et al. (2007) for dry soil.

subsection 2.2.4. The scaling parameter π_2 was chosen as it is the equivalent of the impactor size, while π_V was selected in favour of π_D as it was used in Figure 5.10 by Richardson et al. (2007). When the depth of the crater is not known, the two parameters π_V and π_D are equivalent. Comparing Figures 5.9 and 5.10 it can be seen that the same behavior demonstrated by Richardson et al. (2007) can be observed in the data found in this work. The flattening of the curve increases with yield strength (Richardson et al., 2007), which in this work corresponds to the compaction pressure. Therefore, there should be a compaction pressure between ≈200 Pa and ≈1000 Pa where the exponent b is compatible with the ones found by Gault et al. (1974) and Vanzant (1962) as previously mentioned.

6

Laboratory craters on icy surfaces

6.1. Methodology

In this section, the methods in which the experiments are carried out are described. First, subsection 6.1.1 describes the experiments done with the drop tower, then subsection 6.1.2 describes the conditions for the experiments carried out with the gas gun.

6.1.1. Drop tower

A total of 17 experiments on ice blocks were carried out using the drop tower. These ice blocks were prepared using the methods described in subsection 3.4.3. The first two experiments used a plastic container to hold the ice, and the next four were unconstrained tests (no container). Both of these setups had no dampening foam underneath. The impact mass for these six experiments ranged between 1.519 and 1.995 kg, where 1.519 kg is the minimum mass achievable with the drop tower. Since the velocity ranged between 1.6 and 3.6 m/s, the impact energy ranged between 3.5 and 24 J. After these first six tests, another 11 were carried out where the ice was in a metal container as described by subsection 3.3.5. In these tests the mass was varied from 1.519 to 3.533 kg, resulting in energies between 3.2 and 52 J. the upper limit of 52 J was chosen to test the breaking energy of an ice block, estimated to be around 50 J/kg by Kawakami et al. (1983).

Another 12 drops were carried out on icy particles. These particles were prepared using the method described in subsection 3.4.4. The first six experiments were performed in the insulated container described in subsection 3.3.5 with drop heights between 400 and 1500 mm and no additional weights added. This resulted in impact energies between 2.8 and 13.5 J. The other six experiments were performed in the custom-built steel container described in subsection 3.3.6. This container allowed to experiment on more sample (volume-wise), which in turn means the sample thickness is higher compared to the other container. The drop heights for these six experiments were between 500 and 2000 mm, with the last two drops being performed with an additional 600 g weight. This resulted in impact energies between 4 and 23.7 J. For this set of experiments, the dampening foam was employed, however, it was placed inside the container rather than outside. This was done in an effort to protect the container from damage.

6.1.2. Gas gun

A total of nine experiments on ice blocks were performed with the gas gun, of which one was unconstrained and one shattered the ice. The impact velocities ranged between 40 and 100 m/s obtained by having chamber pressures between 5 and 13 bar. Since the projectile used was always the same 8 mm projectile with a mass of 2.035 g, the variations in impact energy were solely driven by the changes in impact velocity. This resulted in impact energies between 1.4 and 10 J. None of the nine experiments were performed with dampening foam, and the ice samples were prepared in the square insulated container (subsection 3.3.5) for all the experiments, where the ice was kept during the experiment (except for the unconstrained one).

6.1.3. Measurement uncertainties

All the impacts made with the drop tower and the gas gun were made from a vertical impact (i.e. 90° inclination), meaning that the crater should be circular (Schultz, 1996). Therefore after each impact, a minimum of three measurements were taken and the crater dimension was taken as the average of the measurements with the error being the 1σ standard deviation of the measurements. Some of the craters were not circular, however, and in those cases, each measurement is used to characterize the shape, therefore the measurement uncertainty is much larger.

The uncertainty in impact energy is related to the uncertainty in impactor mass and impact velocity. For both the gas gun and drop tower the uncertainty in mass is very low (one ten-thousandth of the measurement), however, the uncertainty in impact velocity is much higher for the gas gun as the velocity is measured by the high-speed camera. The 1σ standard deviation of the impact energy is obtained using Equation 6.1 from the standard deviation of the velocity as mentioned in subsection 3.2.3. The 1σ standard deviation of the velocity is obtained by assuming the velocity is constant as the projectile passes through the FOV of the camera as discussed in section 4.1. For the drop tower, the velocity uncertainty is much lower, resulting in a negligible error in impact energy as discussed in subsection 3.1.2.

$$\delta E = m V_i \delta V_i \tag{6.1}$$

Where E is the kinetic energy, m_i is the impactor's mass, V_i is the impact velocity, and $\delta(x)$ is the variance (or uncertainty) of the value x.

6.2. Results

Table 6.1 is a summary of the data provided in Appendix A, for the drop tower, and Appendix B, for the gas gun, showing only the most useful data. The outcome column shows for each experiment if it is considered valid, and if not, why that is the case. There are four main reasons why an experiment could be considered invalid listed below. The letters in parenthesis indicate which machine the issue can occur in, DT for drop tower and GG for gas gun.

- **Disk impact** (DT):
  Disk above the impact tip of the drop tower impacts the ice after the tip, resulting in two impacts and potential shattering of (part) of the ice due to the second impact.
- **Crater too deep** (DT, GG):
  If the final crater depth is more than 70% of the sample depth, the crater is declared invalid as according to Croft et al. (1979) the results produced by such crater are unreliable. This issue also includes craters which depth is the same as the sample depth, as it is an extreme case of the same issue.
- **Ice depression** (DT):
  Issue occurs when drop tower impact head creates a depression in the ice rather than an impact. This is caused by the impact head not having enough energy to break the ice and create a crater (higher energy requirement for a larger impact head).
- **Moving target** (DT, GG):
  Issue with ice block which moves during impact. Mostly caused by the ice block being placed vertically for the gas gun and sliding out of the container during the firing sequence. However, this can also happen for the drop tower, especially if the ice block is unconstrained.

This section discusses the results obtained from the various experiments performed on ice blocks and icy particles with the drop tower and gas gun. The results obtained by the experiments on shattering energy are discussed in subsection 6.2.1. The results obtained from the ice blocks are then discussed in subsection 6.2.2, followed by the results obtained from icy particles in subsection 6.2.3. Finally, the depth to diameter ratio is discussed for all the experiments in subsection 6.2.4. The interpretation and implication of these results are discussed in chapter 7.

ID	Machine	Surf.	Cont.	Foam	m_i g	d_i mm	V_i m/s	p_i kgm/s	E_i J	D mm	d mm	Outcome
44	DT	IB	PC	N	3063.3	50.1	2.17	6.65	7.23	N/A	N/A	Valid. Ice block broke apart due to weak container.
45	DT	IB	PC	N	3063.3	50.1	3.92	12.0	23.6	N/A	N/A	Valid. Ice block broke apart due to weak container.
46	DT	IB	U	N	1862.3	50.1	2.73	5.08	6.94	N/A	N/A	Valid. Ice block broke apart as it was unconstrained.
47	DT	IB	U	N	1862.3	50.1	2.85	5.32	7.59	N/A	N/A	Valid. Ice block broke apart as it was unconstrained.
48	DT	IB	U	N	1518.8	20.1	2.23	3.39	3.78	N/A	N/A	Valid. Ice block broke apart as it was unconstrained.
49	DT	IB	U	N	1995.3	60.1	2.22	4.43	4.91	N/A	N/A	Valid. Ice block broke apart as it was unconstrained.
50	DT	IB	SC	F	1518.8	20.1	2.09	3.17	3.31	25	N/D	Valid.
51	DT	IB	SC	F	1518.8	20.1	3.15	4.78	7.54	46.8	N/D	Valid.
52	DT	IB	SC	F	1518.8	20.1	4.10	6.22	12.8	30.3	13.33	Valid.
53	DT	IB	SC	F	1518.8	20.1	3.69	5.61	10.4	16.4	1.87	Invalid. Ice depression.
54	DT	IB	SC	F	2119.3	20.1	5.01	10.6	26.6	59	37	Invalid. Disk impact.
55	DT	IB	SC	F	2331.8	50.1	4.36	10.2	22.1	36.3	21.29	Valid.
56	DT	IB	SC	N	2331.8	50.1	3.71	8.65	16.0	45.7	15.33	Valid.
57	DT	IB	SC	N	2331.8	50.1	4.76	11.1	26.4	N/A	N/A	Valid. Ice block shattered.
58	DT	IB	SC	F	2331.8	50.1	4.79	11.2	26.8	31.6	9	Valid.
59	DT	IB	SC	F	3532.8	50.1	5.40	19.1	51.6	N/A	N/A	Valid. Ice block shattered.
60	DT	IB	SC	N	1518.8	20.1	5.53	8.40	23.2	48.7	7.95	Invalid. Disk impact.
61	DT	IP	SC	N	1862.3	50.1	3.43	6.40	11.0	80.4	21.8	Invalid. Crater too deep.
62	DT	IP	SC	N	1862.3	50.1	3.95	7.35	14.5	121	N/D	Invalid. Crater too deep.
63	DT	IP	SC	N	1862.3	50.1	2.75	5.12	7.04	75.9	19.14	Invalid. Crater too deep.
64	DT	IP	SC	N	1862.3	50.1	3.44	6.41	11.0	98.0	36.93	Invalid. Crater too deep.
65	DT	IP	SC	N	1862.3	50.1	2.09	3.89	4.06	115	47.1	Invalid. Crater too deep.
66	DT	IP	SC	N	1862.3	50.1	1.75	3.25	2.84	97.3	47.1	Invalid. Crater too deep.
67	DT	IP	IS	F	1862.3	50.1	2.11	3.93	4.16	133	N/D	Valid.
68	DT	IP	IS	F	1862.3	50.1	3.17	5.91	9.38	143	N/D	Valid.
69	DT	IP	IS	F	1862.3	50.1	4.06	7.57	15.4	153	N/D	Valid.
70	DT	IP	IS	F	1862.3	50.1	4.49	8.37	18.8	162	N/D	Valid.
71	DT	IP	IS	F	2462.3	50.1	4.38	10.8	23.7	128	N/D	Invalid. Crater too deep.
72	DT	IP	IS	F	2462.3	50.1	3.37	8.31	14.0	125	N/D	Invalid. Crater too deep.
20	GG	IB	SC	N	2.035	8	75.9	0.15	5.87	33.4	10.3	Valid.
21	GG	IB	SC	N	2.035	8	76.6	0.16	5.96	22.1	8.2	Valid.
22	GG	IB	U	N	2.035	8	94.6	0.19	9.11	23.1	11.6	Valid.
23	GG	IB	SC	N	2.035	8	89.5	0.18	8.15	22.7	11	Valid.
24	GG	IB	SC	N	2.035	8	42.5	0.09	1.84	13.8	3.6	Valid.
25	GG	IB	SC	N	2.035	8	72.6	0.15	5.36	22.5	7.1	Valid.
26	GG	IB	U	N	2.035	8	101	0.21	10.3	47.7	14.2	Invalid. Moving target.
27	GG	IB	SC	N	2.035	8	90.1	0.18	8.26	33.7	15.95	Valid.
28	GG	IB	SC	N	2.035	8	90.4	0.18	8.31	29.5	12.85	Valid.

Table 6.1: Experimental parameters, crater diameter, crater depth, and experiment outcome. Machine: DT is drop tower and GG is gas gun. Surface: IB is ice block and IP is icy particles. Container: PC is plastic container, U is unconstrained, SC is square container, and IS is insulated steel container. Foam: N is for experiments without foam present and F is for experiments with foam present. N/A is for not applicable (e.g. no crater diameter due to the ice shattering) while N/D is for no data for when a measurement was not taken. For a more comprehensive logbook see Appendix A and Appendix B.

6.2.1. Impact energy required to shatter ice blocks

The shattering energy, or the energy required to shatter the ice block, can be obtained from these experiments. In previous works, this shattering energy was measured in J/kg, suggesting that the mass of the ice block was the only factor in determining the shattering energy for a given ice block. However, from the data obtained in this work the shattering energy is between 24 and 27.3 J/kg (drop #57) in the case where no dampening foam is present. This value is about half of the 50 J/kg that Kawakami et al. (1983) found in his research. One reason for this difference is the ice types used in the experiments. In his experiments, Kawakami et al. (1983) used uniform ice blocks cut out from a large commercially-made ice block, while in the experiments performed for this work the ice was much less uniform as described in subsection 3.4.3. This difference in ice uniformity changes the properties of the ice, with the more uniform ice having a higher ultimate strength, which allows the ice to absorb more energy before braking. Another reason for this difference could be the presence of foam under the ice block. In his experiment, Kawakami et al. (1983) used a 5 mm polyurethane foam sheet under the ice block, while in the experiment where the braking energy was found to be around 25 J/kg no foam was used.

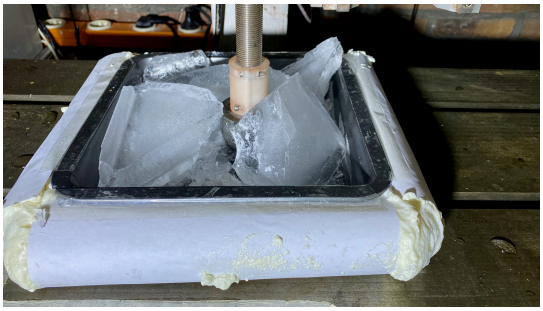

Figure 6.1: Shattered ice for the experiment performed without dampening foam, obtained for 26.4 J impact energy (drop #57).

Figure 6.2: Shattered ice for the experiment performed with dampening foam, obtained for 51.6 J impact energy (drop #59).

As mentioned above, one of the reasons for the discrepancy in shattering energy between this work and the work done by Kawakami et al. (1983), was the absence of dampening foam under the ice block in the experiment carried out in this work. Therefore, another experiment was conducted with dampening foam (drop #59). Using the foam, the shattering energy was found to be below 56 J/kg, however, the lower value is hard to constrain further than 30 J/kg. Above this value, the foam is heavily compressed, and when the impact tip is lifted from the impact, the foam springs back pushing the container upwards. This makes it hard to determine if the ice block has shattered during the impact or afterward when coming down after being launched up, even when using the high-speed camera.

Figure 6.3: Cross-sectional view of shattered ice formed in plastic container (drop #45).

Figure 6.4: Cross-sectional view of shattered ice formed in metal container (drop #57).

The first six experiments (drops #44 through #49) also resulted in the ice breaking apart. In the constrained experiments the shattering energy was found to be below 11.4 J/kg. However, it is hard to determine if this is the shattering energy or simply the energy required to fracture the ice as the plastic container broke apart, which would have failed to keep the ice together even after a nominal impact. For the unconstrained case the shattering energy is even lower, only 7.14 J/kg. However, this

can hardly be considered shattering energy, instead, it is simply the energy required to break the ice throughout its thickness.

6.2.2. Ice blocks

Experiments on icy particles were carried out using the drop tower (subsection 6.1.1) and gas gun (subsection 6.1.2). The two machines produced very different data, with the gas gun producing a higher rate of valid craters compared to the drop tower (89% compared to 47%) as it can be seen in Table 6.1. The difference between craters produced by the drop tower and gas gun can be seen

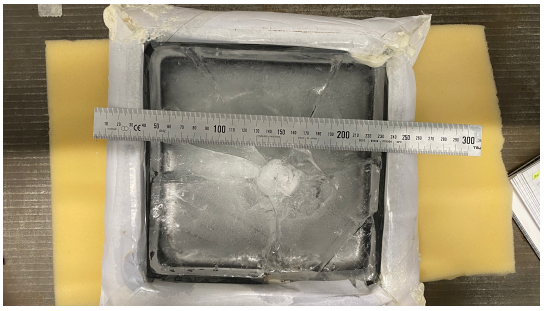

Figure 6.5: Impact crater produced by drop tower in drop #56.

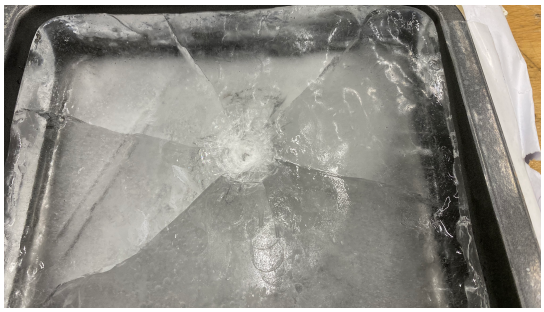

Figure 6.6: Impact crater produced by gas gun in shot #22.

comparing Figure 6.5 to Figure 6.6. The crater in Figure 6.5 has a clearer crater rim, due to the large size of the impact head combined with the slight melting of the ice block by the head, compared to the crater produced by the gas gun. While not easily visible in the figures, the crater produced by drop #56 is closed to a hemisphere than the typical bowl shape of a crater-like the one pictured in Figure 6.7.

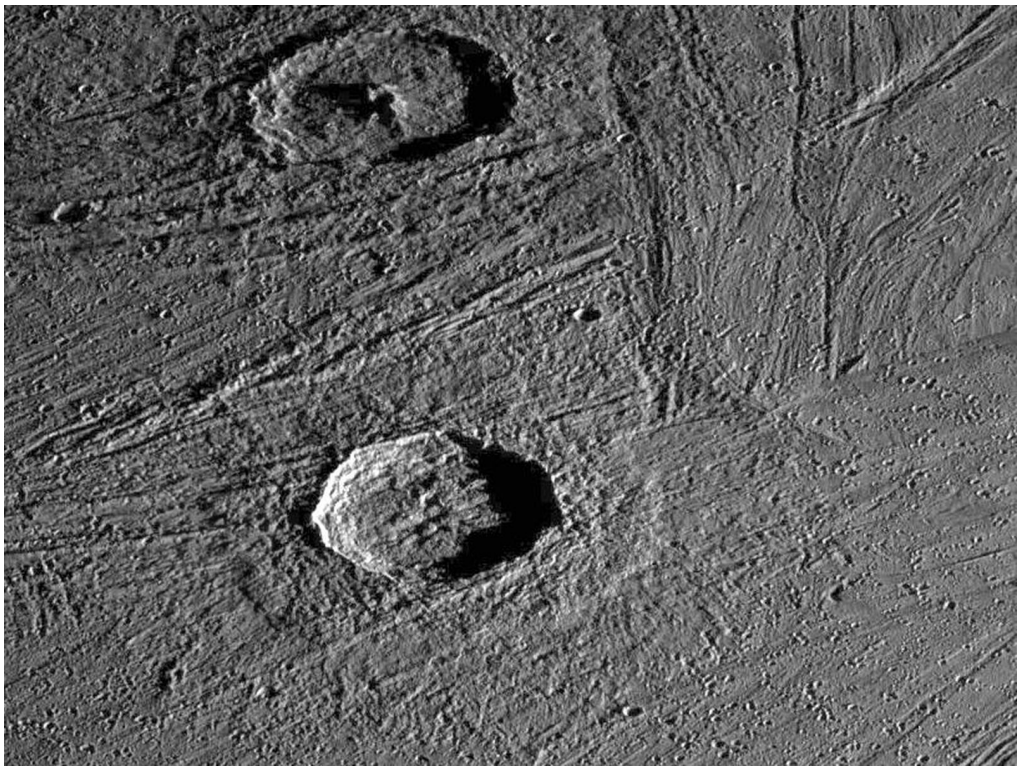

Figure 6.7: Two craters on Ganymede. Gula crater (top) with crater diameter of 38 km, and Achelous crater (bottom) with outer crater diameter of 32 km. Credit: NASA/JPL/Brown University

The crater information can then be processed to produce a line of best fit, useful when analyzing craters on icy moons in chapter 7. In order to improve the prediction accuracy, the data is split into

different categories, based on how the crater was formed. Each crater was formed by an impact head or projectile of a given diameter, either with or without dampening foam. Therefore, five different best-fit curves are provided, plus an overall fit, three for each impactor diameter and two for the presence of dampening foam. The scaling relationships for the diameter-energy scaling are provided in Table 6.2, while the ones obtained via π scaling are provided in Table 6.3.

Data set	a	b	R^2
$d_i = 8.0$ mm	0.015 ± 0.0070	0.24 ± 0.22	0.26
$d_i = 50.1$ mm	0.34 ± 0.0065	-0.72 ± 0.0060	0.99
$d_i = 20.1$ mm	0.020 ± 0.0052	0.18 ± 0.18	-0.22
Foam	0.022 ± 0.0026	0.12 ± 0.044	-0.39
No foam	0.012 ± 0.0062	0.33 ± 0.23	0.37
All	0.018 ± 0.0027	0.18 ± 0.065	0.11

Table 6.2: Best fit equations for ice blocks with energy-diameter scaling, along with coefficient of determination (i.e. R^2).

Data set	α	β	R^2
$d_i = 8.0$ mm	2.5 ± 4.1	0.00010 ± 0.00028	0.21
$d_i = 50.1$ mm	1.1 ± 4.3	0.00010 ± 0.0024	-0.61
$d_i = 20.1$ mm	1.1 ± 2.5	0.00010 ± 0.0013	-0.14
Foam	1.1 ± 1.4	0.0001 ± 0.0072	-0.13
No foam	2.5 ± 3.6	0.0001 ± 0.00072	0.34
All	$0 \pm 0.$	$0. \pm 0.$	0.0

Table 6.3: Best fit equations for ice blocks with π scaling, along with coefficient of determination (i.e. R^2).

6.2.3. Icy particles

Experiments in icy particles were performed in two different containers as described in subsection 6.1.1. Unfortunately, only some of the experiments performed with the insulated steel container produced valid data as shown in Table 6.1. The difference between a valid and invalid experiment due to the crater being too deep can be seen in Figures 6.8 and 6.9 respectively. While visual inspection is not enough to determine whether or not a crater is invalid due to its depth, in the case of drop # 70 the crater is deep enough that the dampening foam underneath is visible as it can be seen in Figure 6.9, meaning the crater depth is as deep, or almost as deep, as the available sample depth.

Figure 6.8: Crater in icy particles where the crater depth is shallow enough for the crater to be valid (drop #67).

Figure 6.9: Crater in icy particles where the crater depth is too deep, making the crater invalid (drop #70).

With the remaining four data points, a best-fit curve of the data can be created for the energy-diameter scaling and π scaling. As it can be seen in Figure 6.10, all the four experiments fit on the fit curve within their error bars. This is reflected in the low uncertainties and high coefficient of determination shown in Table 6.4. The same can be said for the π scaling relationship shown in Figure 6.11 where the data points lie on the curve within their error bars. These two best-fit curves are the ones that match the data the closest compared to the ones described in subsection 6.2.2.

Data set	a	b	R^2
Steel container	0.11 ± 0.0057	0.13 ± 0.021	0.95

Table 6.4: Best fit equations for icy particles with energy-diameter scaling, along with coefficient of determination (i.e. R^2).

Data set	α	β	R^2
Steel container	2.5 ± 0.45	$8.5 \times 10^{-5} \pm 1.0 \times 10^{-4}$	0.95

Table 6.5: Best fit equations for icy particles with π scaling, along with coefficient of determination (i.e. R^2).

6.2.4. Depth to diameter ratio for ice blocks

The depth to diameter (d/D) ratio for a crater is mostly used to determine the volume of a crater, however, it can also be used to have more information about the crater. This ratio should always be

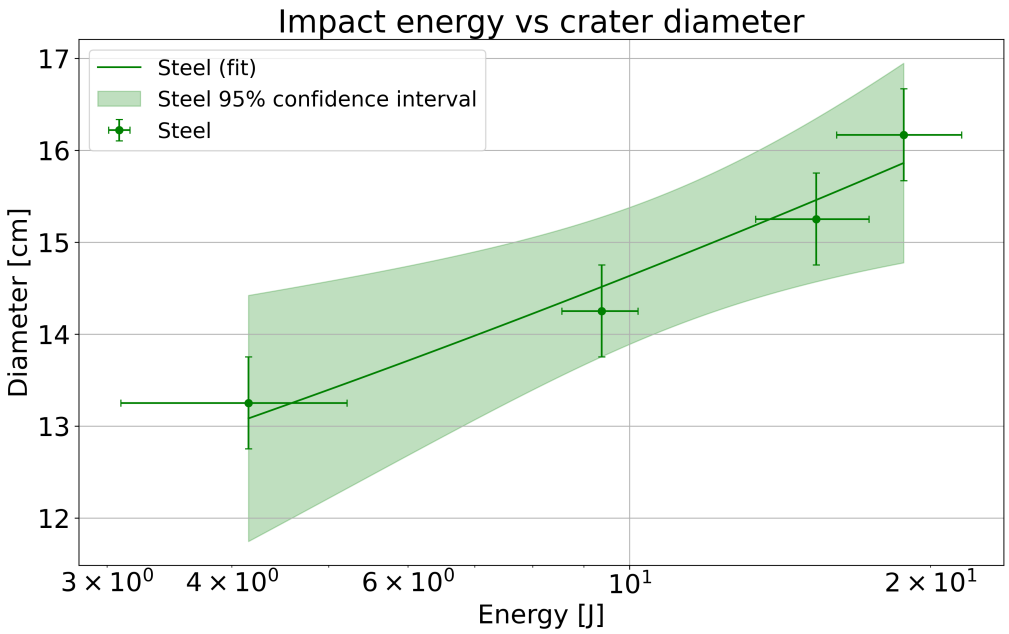

Figure 6.10: Results of impacts in icy particles along with energy-diameter scaling relationship and 95% confidence interval for prediction.

smaller than 1 as a crater is never deeper than it is wide. This value was found to be between $1/4$ and $1/3$ for impacts in rocky surfaces (Melosh, 1989; Schmidt & Housen, 1987). From the experiments performed in ice by both the drop tower and gas gun, this ratio is found to be between 0.25 and 0.50 for most cases, with an average of 0.38 and a 1σ standard deviation of 0.086. Only a few drops are not within these bounds. Drop #53 ($D = 16.4$ mm) has a very low d/D, as the impactor did not create a crater, but instead only a depression in the ice caused by the head resting on the ice after the impact. Drop #54 ($D = 59.0$ mm) has a very high depth to diameter ratio as it was produced by the small impact head which fully penetrated the ice resulting in a deep crater. Something similar happened to drop #60 ($D = 48.7$ mm), however, in this case, some of the ice shattered from the walls filled the crater, resulting in a lower apparent depth which does not correspond to the transient crater depth (and diameter) than all the other experiments measure. The last anomaly with the drop tower is the one obtained by drop #55 ($D = 36.3$ mm), where the depth to diameter ratio is 0.59. While the exact reason for this anomaly is not clear, one explanation could be the higher depth due to the ice cracking to the bottom of the container, combined with the slightly smaller crater diameter that was expected for a crater made with that impact energy. As discussed in subsection 7.1.1, the larger impact head is the cause of the smaller crater diameter. Another anomaly worth mentioning is the one produced by shot #24 ($D = 13.8$ mm), where the error bars are much larger compared to other shots. This shot resulted in a crater with a few cracks which made it hard to precisely measure the crater diameter. This is most likely a result of the ice used and how it was hit in a weak spot, allowing the cracks to spread more easily.

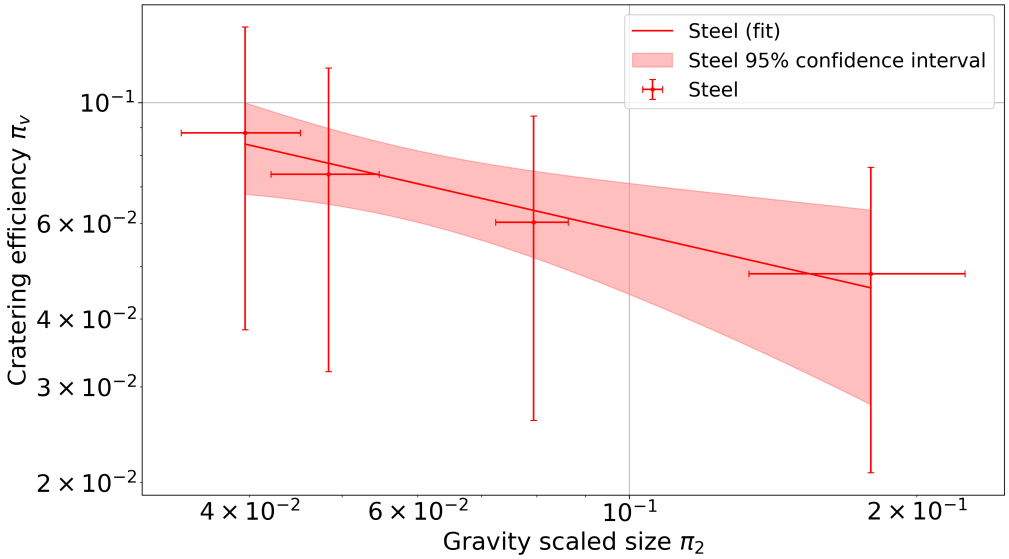

Figure 6.11: Results of impacts on icy particles using π dimensionless parameters.

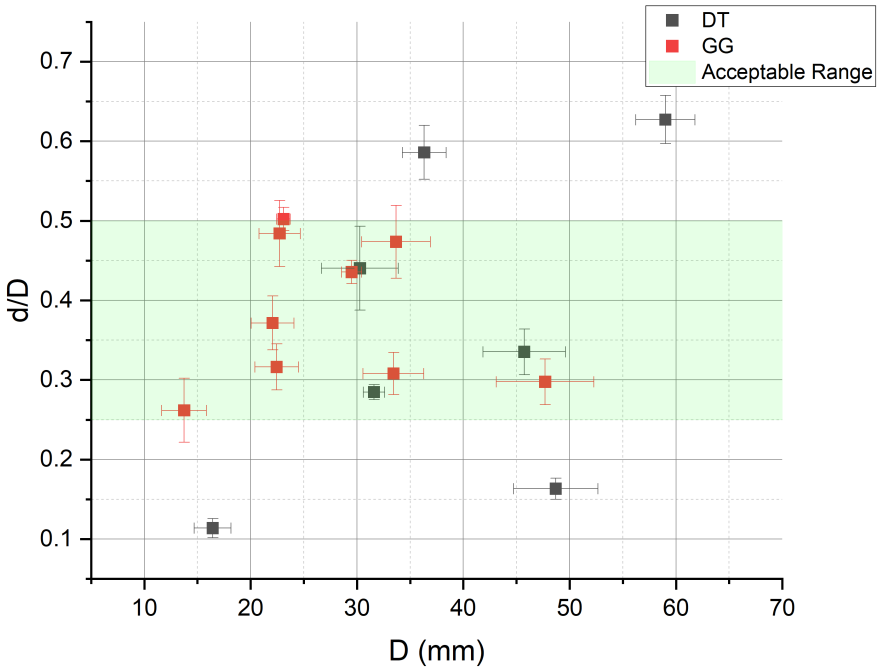

Figure 6.12: Depth to diameter ratio for experiments performed with drop tower and gas gun.

7

Discussion

This chapter discussed the results obtained in chapter 6. First, the interpretation of the data is discussed in section 7.1, both from an experimental point of view and from a scientific one. Next, the data obtained from icy impacts are compared to the one found by previous researchers in section 7.2. The limitations of the experiments are then explained in section 7.3. The data is then applied to icy moons in sections 7.4 and 7.5. In section 7.4 the diameter of impactors is estimated for different impacts on Ganymede and Enceladus, while in section 7.5 a prediction of the required impactor size to shatter a given surface is provided.

7.1. Interpretation

The data obtained in chapter 6 is interpreted in this section. First, the effect of the impactor diameter is discussed in subsection 7.1.1. This is more important from an experimental point of view, rather than for the final scientific objective. Next, the effect of the dampening foam used in the experiments is discussed in subsection 7.1.2, both from a cratering perspective and from the perspective of required shattering energy. Finally, the differences between the icy particles and ice blocks are discussed in subsection 7.1.3.

7.1.1. Effect of impactor diameter

The effect of the impactor diameter on the final crater is more interesting from an experimental perspective than from a scientific one. To analyze the effect of the impactor diameter, the crater diameter data can be plotted and separated by impactor diameter.

The effect of the impactor diameter can be studied by analyzing each set of points separately and then comparing them. Figure 7.1 shows the results for all experiments performed with the drop tower and gas gun, separating the points by impactor diameter (d_i). Starting from the large head of the drop tower (50.1 mm indicated in red in Figure 7.1), one would expect the craters to be larger than the rest, or at least that the minimum crater diameter would be no smaller than the impactor diameter. However, looking at the data this is not the case. This is because the head does not fully penetrate the ice upon impact, resulting in a depression in the ice rather than an impact crater which is the reason these points are excluded from the results. The reasons for the decreasing diameter with increasing energy are unclear, however, one reason could be the length of time before the impactor was raised above the ice. Since the catch mechanism failed for all three drops, the impact head came to rest on the ice after the impact, which continued to melt the ice. The more time the impactor stayed on the ice, the further down it melted the ice, and the larger the depression became.

Comparing the 20.1 mm impact head from the drop tower to the 8 mm projectile used by the gas gun, it can be seen that the rate at which the crater diameter increases with increasing energy is lower for the larger impact head compared to the small projectile. This is partially because the least energetic impact for the drop tower should have resulted in a crater smaller than the impactor diameter which is not possible.

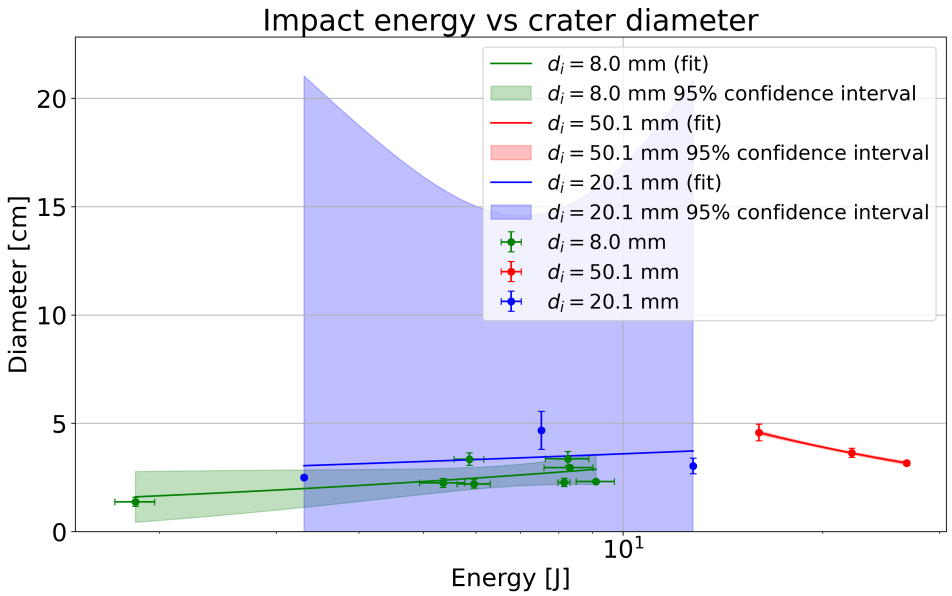

Figure 7.1: Results of all (valid) impact experiments in ice blocks divided by impactor diameter. Also included are impacts with 50.1 mm head from the drop tower.

7.1.2. Effect of foam

Dampening foam was used in the experiments performed with the drop tower to see how the cratering behaves when some of the energy is absorbed, and to simulate a deeper ice block or an interface that is not steel (e.g. a subsurface ocean). Figure 7.2 shows the data obtained without foam (this includes the data obtained by the gas gun) in red, while the data obtained with dampening foam is shown in blue. Due to the lower shattering energy of the experiments with no foam as mentioned before, not many drops could be performed with this setup.

Comparing the experiments performed with and without dampening foam it can be seen that the craters are of comparable sizes as they do not differ much. However, craters formed without dampening foam tend to show a trend that would results in larger craters (compared to their counterparts formed with dampening) for higher impact energies.

7.1.3. Effect of surface

The data obtained from impacts on icy particles can be compared to the one obtained from ice blocks to determine the effect the surface has on the final crater diameter. This comparison is done in Figure 7.3 where it can be seen that, for the same energy, the crater diameter on icy particles is about five times larger than for ice blocks. In subsection 5.2.3 it was discussed how the shear strength of the target affects the final crater diameter, where it was concluded that increasing the shear strength of the target decreased the final crater diameter. While the shear strength of the ice blocks and icy particles was not measured in these experiments, the ice block is a solid material with shear strength in the order of 10^5-10^6 Pa (Frederking et al., 1988), while icy blocks are comparable to the cement powder (although the actual shear strength is most likely much lower than for cement) with shear strength measured in this work in the order of 10^3 Pa. Therefore, the expected crater diameter for icy particles should be larger compared to the ice block, which is exactly what can be seen in Figure 7.3.

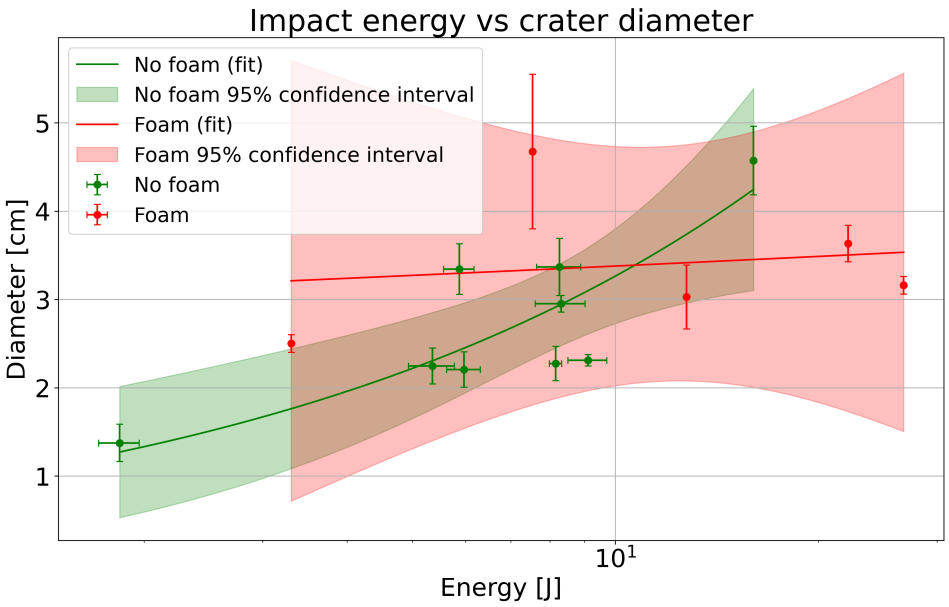

Figure 7.2: Results of all impact experiments in ice blocks divided by presence or absence of dampening foam.

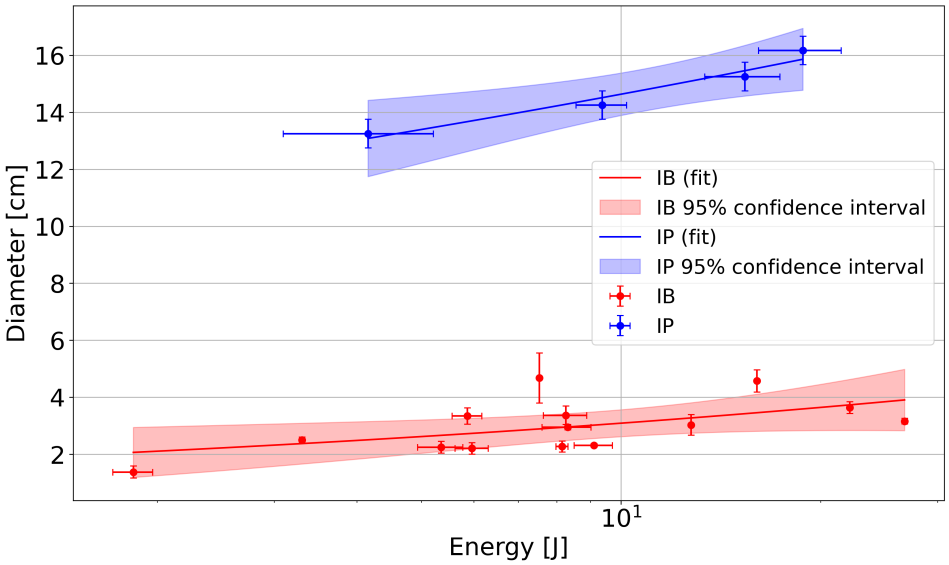

Figure 7.3: Results of impacts classified by surface type. IB stands for Icy blocks, while IP stands for icy particles.

7.2. Comparison

This section compares the data obtained from this work to the data obtained in previous works. First, subsection 7.2.1 compares the results obtained with ice blocks to the ones obtained in literature (also made using ice blocks). Then, subsection 7.2.2 discusses the same but using the results obtained on icy particles rather than on ice blocks.

7.2.1. Ice blocks to literature

The data obtained during the experiments performed on ice blocks throughout with work can be compared to data obtained from previous studies on impacts on ice blocks. Figure 4.3 (reported below as Figure 7.4) shows the results of this work alongside the best-fit curves produced by the other experiments. The figure also shows an area around the best-fit curve for the data obtained in this work which represents the 95% confidence interval (or 2σ) of the fit. Most of the points shown in Figure 7.4

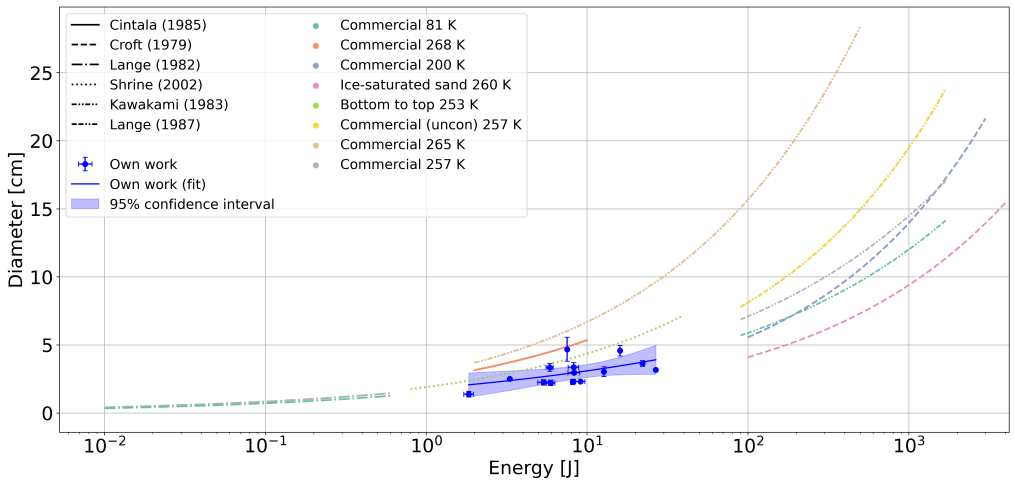

Figure 7.4: Data obtained by impacts on ice blocks in this work alongside best-fit equations for previous papers. Line type indicates the paper, line color indicated ice temperature, and the blue data is the results of this work.

are below the curves provided by previous works. This is at least partially because many impacts in this work are performed on dampening foam which tends to decrease crater diameter as described in subsection 7.1.2. The data obtained in this work is closest to the data obtained by Shrine et al. (2002), with parts of the curve included in the 95% confidence interval of the curve made from the data obtained in this work. However, when it comes to the slope of the curve, the data in this work matches the curve provided by Lange and Ahrens (1987) the closest, as that curve has an exponent of 0.31.

7.2.2. Icy particles to literature

The same comparison done in subsection 7.2.1 can be done for the results in icy particles. In subsection 7.1.3 it was concluded that impacts on icy particles produce craters about five times larger compared to their counterparts formed in ice blocks. Therefore, the results obtained in icy particles should be larger than the ones obtained by previous works. This is exactly what can be seen in Figure 7.5 where even the lower estimation of crater diameter of the 95% confidence interval is at least twice as large as the estimates provided by previous work by Kawakami et al. (1983) (largest crater at the given range).

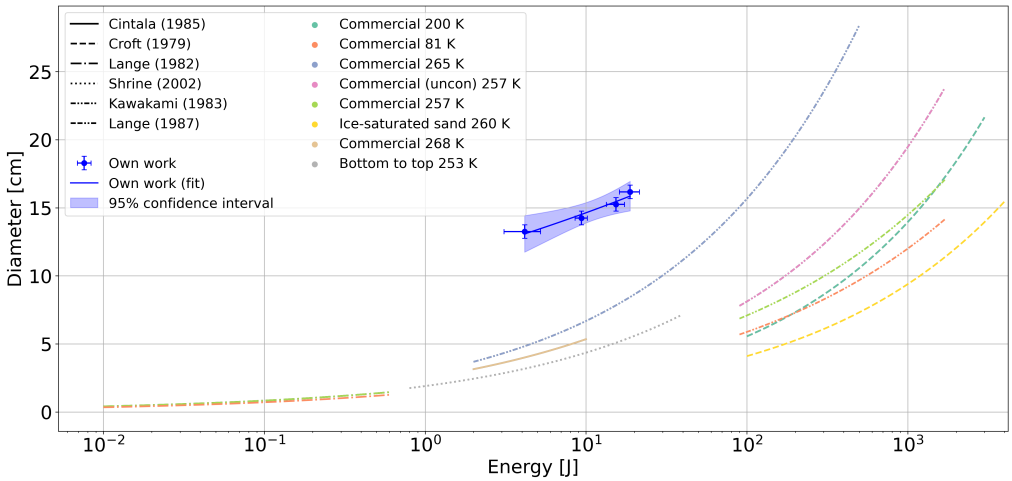

Figure 7.5: Data obtained by impacts on icy particles in this work alongside best-fit equations for previous papers. Line type indicates the paper, line color indicated ice temperature, and the blue data is the results of this work. (Note: uncon is short for unconstrained).

7.3. Limitations

The limitations of this work are discussed in this section, with the ones related to the lab conditions discussed in subsection 7.3.1 and the ones due to the scaling laws behavior discussed in subsection 7.3.2.

7.3.1. Ranges of scaling parameters

The π scaling parameters discussed in subsection 2.2.4 can be used to determine how the data obtained in this work compares to the craters seen on icy moons. To generate the ranges of the scaling parameters obtained on icy moons, the data provided by Zahnle et al. (2003) is used. This data contains a series of cratering parameters for the moons of Jupiter, Saturn, Uranus, Neptune, and Pluto. Among these values, the impactor velocity, impactor diameter, target density, and gravitational acceleration (of the moon) are provided. The value for the impactor diameter is the value required to form a 20 km crater, meaning smaller impactors forming smaller craters, and vice versa, are not accounted for. Despite this limitation, this data set can be useful in determining the ranges for these scaling parameters across all the moons. Two parameters are missing from this data set to fully compute all the necessary parameters, the impactor density and the depth to diameter ratio of the craters. The scaling parameters are then computed with the minimum and maximum values found for these two parameters to better represent the range of values these scaling parameters can be. The minimum density is taken as 0.3 g/cm^3 for an icy comet (D. Britt et al., 2006; Thomas et al., 2013) and the maximum density is taken as 8 g/cm^3 for an iron-based comet (D. T. Britt & Consolmagno, 2004). The depth to diameter ratio is taken between 0.25 and 0.5 as discussed in subsection 6.2.4. Another parameter has to be estimated, however, as the data set provided by Zahnle et al. (2003) only accounts for heliocentric impactors. Using the data shown in Table 2.1, the ratio between heliocentric and planetocentric velocity can be calculated to be between 2.87 and 4.45. To keep the same crater diameter the impactor's diameter must be increased by a factor of $k^{2/3}$ to keep the same impact energy. Here k is the ratio of planetocentric to heliocentric impact velocity (i.e. $k = v_{pl}/v_{he}$).

π_2 scaling

The π_2 dimensionless parameter depends on three parameters, gravity, impactor size, and impactor velocity. Considering all the ranges of parameters discussed before, and using Equation 2.10, the values for π_2 for heliocentric impactors ranges between 10^{-6} and 10^{-2} for an impactor producing a 20 km crater. The same range of values, scaled for planetocentric impactors produces a range of values for π_2 between 10^{-5} and 1.

In a laboratory setting on Earth, the gravity is fixed at 9.81 m/s^2, therefore the impactor diameter and velocity must be adjusted to obtain similar π_2 values. The value of π_2 can be calculated for the drop tower and gas gun. For the drop tower this value is between 10^{-2} and 10^{-1} while for the gas gun π_2 is between 10^{-5} and 10^{-4}. Both values are within the bounds obtained before for crater formation

on icy moons, with the drop tower being close to the upper bound and the gas gun being close to the lower bound.

π_V scaling

The cratering efficiency parameter depends on the target density, crater volume, and impactor mass. The data provided by Zahnle et al. (2003) does not provide crater volumes or impactor mass, therefore these need to be estimated to obtain a range of π_v. The impactor volume is easy to estimate as the diameter of the impactor is provided and it is always assumed the impactors are spherical. From the volume, the mass can be calculated by using the ranges of densities provided above. Finally, the crater volume can be estimated from the crater diameter, using the ranges of depth to diameter ratio provided. Using these parameters, and Equation 2.9, π_v ranges between 1 and 10^5 for a crater of 20 km and a heliocentric impactor, and 10^{-1} and 10^5 for a planetocentric impactor resulting in the same size crater. The range for the planetocentric case is one order of magnitude below the one for the heliocentric impactor.

The values obtained in the lab for the craters created in this work range between 10^{-1} and 10^1 for the gas gun, and between 10^{-5} and 10^{-2} for the drop tower. These numbers are much smaller than the ones observed for real craters. To obtain values in the range of the planetocentric and heliocentric craters, the crater volume could be increased. Alternatively, the impactor mass could be decreased or the target density increased.

7.3.2. Best-fit limitations

In section 6.2 the best-fit curves is provided for different experiments (e.g. icy particles, foam, etc.). However, it is important to know what the limitations of these best-fit curves are. In this work two types of best-fit curves are used, one using π scaling and one using the simple energy-diameter scaling. Both these scaling relationships have two scaling parameters, each one with its uncertainty. The uncertainty for these parameters is based on the least square method supplied with the uncertainties in the y-direction (i.e. π_v for π scaling and D in the energy-diameter scaling). As it can be seen in tables Table 6.2 and Table 6.3, the scaling relationships for ice blocks have a low coefficient of determination, both for energy-diameter scaling and π scaling relationships. A low R^2 value means high uncertainty in the scaling parameters which produce large confidence intervals as can be seen in Figure 7.6. These large uncertainties than have a significant impact when used to determine impactor diameter in section 7.4. The fit provided for icy particles, on the other hand, has much lower uncertainties ($R^2 \approx 0.95$) as can be seen in Figure 7.7.

The best-fit equations obtained from the data collected in this work also tend to have a low exponent (for diameter-energy scaling) compared to other works. This means that in order to create very large craters much more energy is required compared to other models.

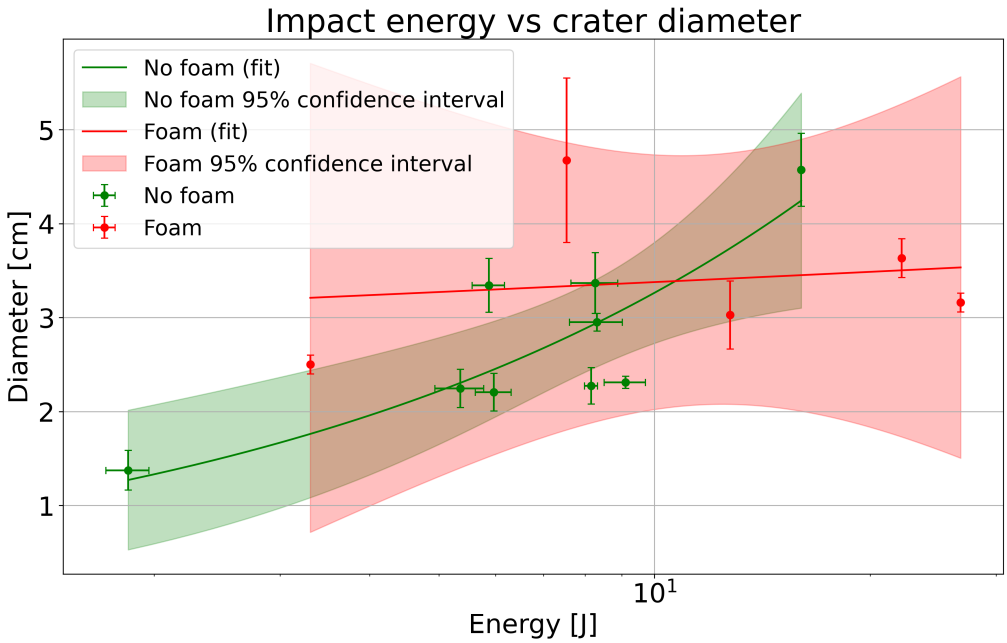

Figure 7.6: Energy-diameter scaling fit depending on presence of foam for ice blocks, along with the confidence interval of the prediction.

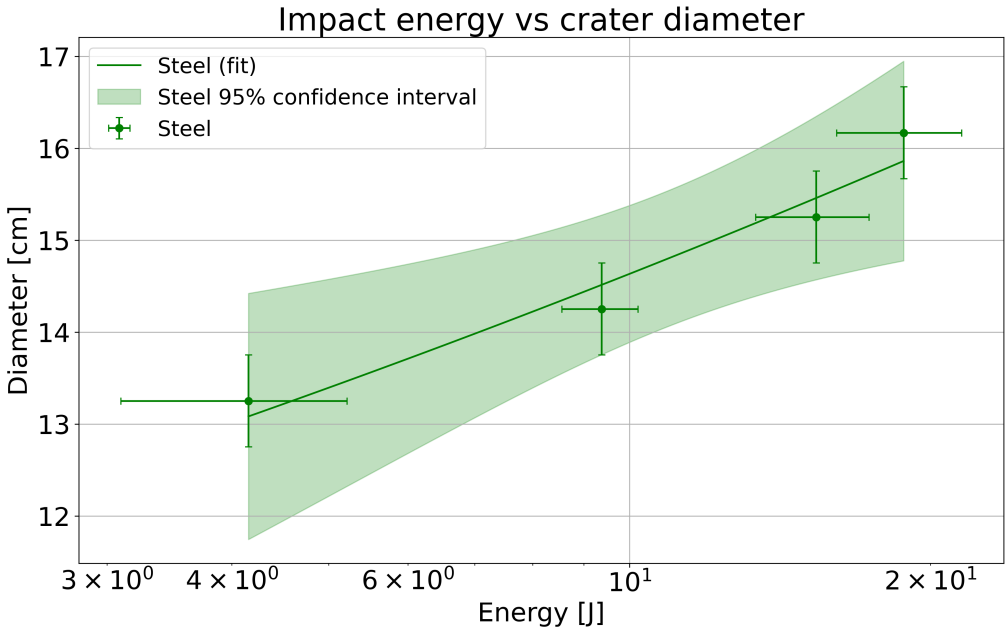

Figure 7.7: Energy-diameter scaling fit for icy particles, along with the confidence interval of the prediction.

7.4. Estimating impactor diameters

Using the largest craters on Ganymede and Enceladus, the size of the largest impactors can be estimated using the scaling laws found in chapter 6. In order to know whether the craters found on Enceladus and Ganymede were formed by gravity-dominated cratering or strength-dominated cratering, the method discussed in subsection 2.2.5 of using the transition diameter between simple and complex craters can be used. Zahnle et al. (2003) showed that for Ganymede the transition diameter is around 2.5 km while for Enceladus this diameter is around 15 km. All the craters discussed in this study are above those two transition diameters, meaning that the craters were formed by gravity-dominated cratering. Since the experiments were performed on a different body compared to where they are being applied, the π scaling relationships should be used. To obtain the impactor diameter from the crater diameter, the two dimensionless parameters of π_2 and π_v can be used using the relationship shown below where the values for α and β are obtained from experiments.

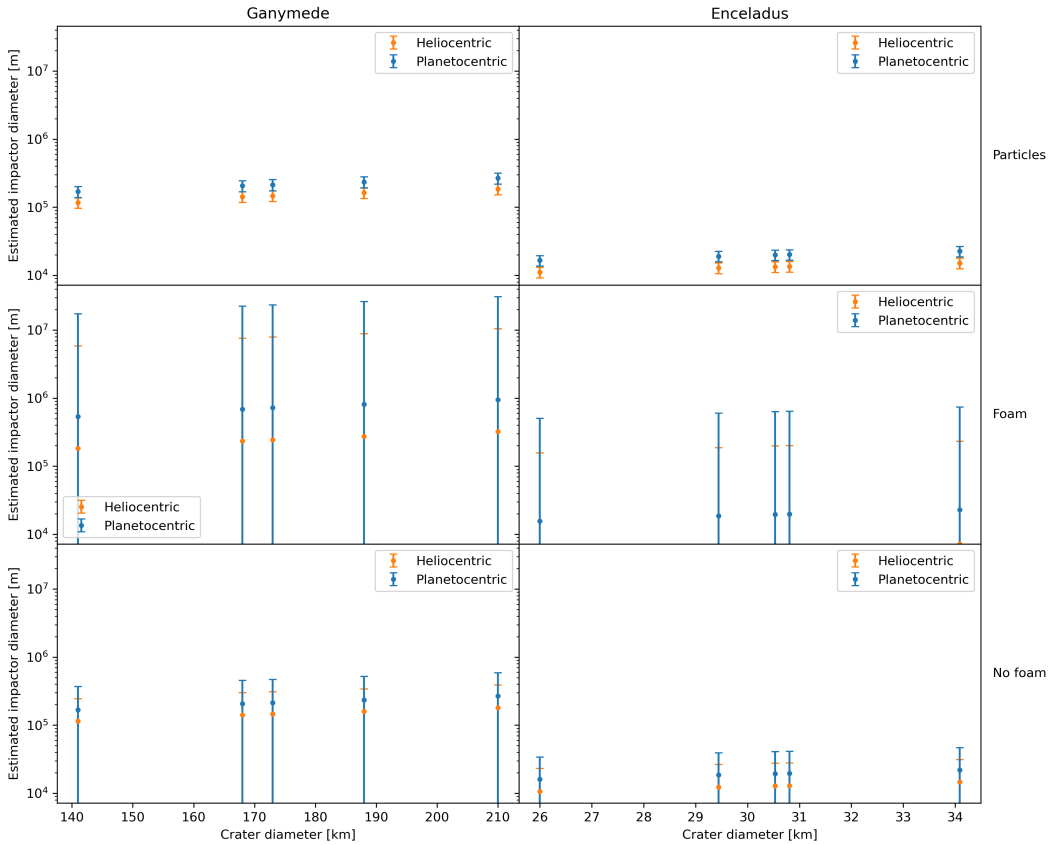

Figure 7.8: Estimated impactor diameters for craters of a given size for different scaling laws found in chapter 6. Impact velocities are moon-dependant and are obtained from Table 2.1 (Note: errors bars are symmetrical in linear space). For Ganymede: V_{he} = 20.0 km/s, V_{pl} = 5.76 km/s, and g = 1.428 m/s^2. For Enceladus: V_{he} = 22.3 km/s, V_{pl} = 5.86 km/s, and g = 0.113 m/s^2. For both: ρ_t/ρ_i = 1.

$$\pi_2 \pi_V^{\alpha} = \beta \tag{7.1}$$

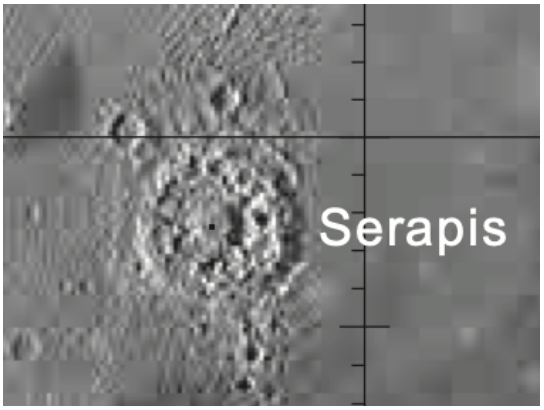

Figure 7.9: A picture of the Serapis crater on Ganymede, with a diameter of 169 km. Image credit: NASA/JPL.

Figure 7.10: A picture of the Ali-baba crater (center) on Enceladus, with a diameter of 34 km. Image credit: NASA/JPL.

Working out Equation 7.1 results in the equation below.

$$L = \left(\beta \left(1.61 \left(\frac{\rho_t}{\rho_i} \right)^{\alpha} \left(D^3 \left(\frac{d}{D} \right)^2 \left(3 - 2\frac{d}{D} \right) \right)^{\alpha} \frac{g}{v_i^2} \right)^{-1} \right)^{1/(1-3\alpha)} \tag{7.2}$$

Where ρ_t/ρ_i is the ratio between target and impactor density, D is the crater diameter, d/D is the depth to diameter ratio, g is the gravitational acceleration at the surface of the body, and v_i is the impact velocity. The error bars are calculated from the errors in α and β (full derivation in Appendix E). Using the π scaling relationships found in sections 6.2.2 and 6.2.3, the size of impactor diameter can be estimated for the five largest craters on Ganymede (like Serapis [1] shown in Figure 7.9) and Enceladus (like Ali-baba [2] shown in Figure 7.10). Figure 7.8 shows different estimates for crater diameters, two for each scaling relationship, one for the planetocentric velocity, and one for the heliocentric velocity. Impacts in icy particles produced larger craters as discussed in subsection 7.1.3, therefore the impactor diameter required is smaller compared to impacts in ice blocks, which is what can be seen in Figure 7.8. The results obtained from impacts on foam are the opposite of the ones in icy particles, as the foam absorbs some of the energy, more energy (and therefore a larger impactor) is required to make a crater of a certain size. Finally, the impactor diameters obtained from the scaling relationships found by impacts on ice blocks without foam are smaller than the ones from impacts with foam, as the scaling exponent α is higher for no foam, meaning that craters grow faster for a given change in energy compared to their counterparts formed with foam.

The impactor diameter can also be estimated using previous works. However, since no π scaling relationships were given, the energy-diameter scaling must be used. Doing so results in the estimates shown in Figure 7.12. This estimate produces impactors with more likely diameters. However, these estimated are provided without π scaling and therefore do not take into consideration different gravitational accelerations. Doing so would result in much smaller impactors (due to the lower gravity).

In the best-case scenario (icy particles scaling), Figure 7.8 shows that the diameter of an impactor needed to produce the large craters on Ganymede is around 10^5 m while for Enceladus this is around 10^4 m. These values are very large, especially when considering that only two comets have been found with a diameter larger than 100 km (Lellouch et al., 2022; Stansberry et al., 2008) and only one object in the main belt is that large as it can be seen in Figure 7.11. This could either mean that very large impactors are required which are no longer seen in the solar system of today, or that the values for α

[1] https://planetarynames.wr.usgs.gov/Feature/5436
[2] https://planetarynames.wr.usgs.gov/Feature/184

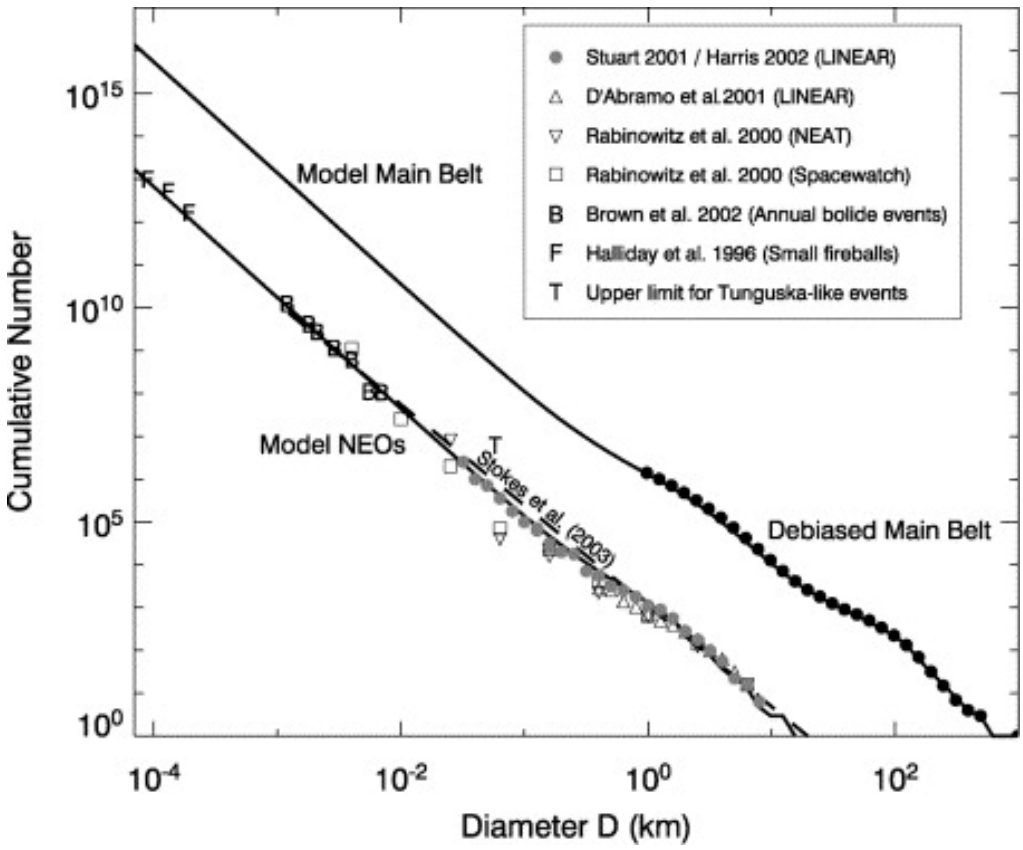

Figure 7.11: Asteroid sizes and their cumulative number. Debiased refers to the fact that all type of MBAs are represented in the plot. Image credit: Bottke et al. (2005)

and β found in this work are incorrect. The latter is the most likely, as the fit obtained in this work has some limitations as described in subsection 7.3.2.

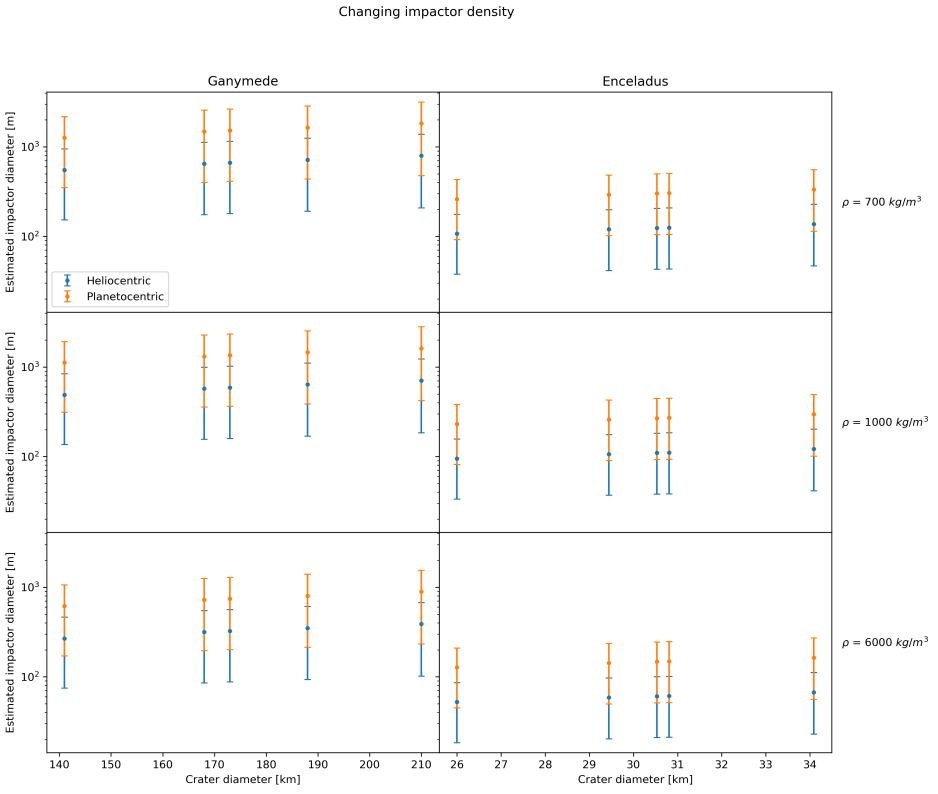

Figure 7.12: Estimated impactor diameters for craters of a given size for different scaling laws found by Shrine et al. (2002). Impact velocities are moon-dependant and are obtained from Table 2.1 (Note: errors bars are symmetrical in linear space). For Ganymede: V_{he} = 20.0 km/s, V_{pl} = 5.76 km/s, and g = 1.428 m/s^2. For Enceladus: V_{he} = 22.3 km/s, V_{pl} = 5.86 km/s, and g = 0.113 m/s^2.

7.5. Predicting surface shattering

The shatter condition on the icy moons can be estimated based on the results obtained by the experiments. In the experiments, the shattering energy is given in J/kg, meaning that an equivalent to the sample mass must be determined for the moon upon impact. One way to achieve that is to analyze the shock wave propagating upon impact and use that to determine what volume of the ice interacts with the impact. The pressure of a shock wave propagates according to exponential decay following the equation below (Kraus et al., 2011).

$$P(R) = P_{ic}\left(\frac{R_{ic}}{R}\right)^{n} \tag{7.3}$$

Where P_{ic} and R_{ic} are the pressure and radius of the isobaric core respectively, P is the pressure at a given position R radially from the center of the impact, and n is the decay exponent and can vary between 1 and 3 (Pierazzo et al., 1997). The radius of the isobaric core mostly depends on the radius of the impactor R_i, along with the impact velocity V_i, and material porosity ϕ according to the following equation (Kraus et al., 2011).

$$\log\left(\frac{R_{ic}}{R_i}\right) = 0.22 - 0.13\phi - 0.18\log\left(V_i[\text{km/s}]\right) \tag{7.4}$$

To obtain a radius for the material involved in the impact, a certain pressure is chosen. As the pressure upon impact is hard to estimate without simulations, instead of choosing a final pressure, the ratio of P/P_{ic} was chosen to be 0.02 (Grieve, 1999). Meaning that the final pressure is taken to be 2% of the initial pressure. This eliminates the need to calculate the pressure at the isobaric core, along

with choosing a final pressure. Using a final pressure that is 2% of the initial one ensures that the final pressure is below the shattering pressure (not energy) of ice. The radius can be calculated using Equation 7.3, and the volume of the material involved in the impact can be computed using the equation below.

$$V = \begin{cases} \frac{2}{3}\pi R^3, & R \leq D \\ \pi\left(R^2 D - D^3/3\right), & R > D \end{cases} \tag{7.5}$$

Where D is the depth of the ice layer, as only the ice is considered in the impact. The equation is continuous at the boundary $R = D$. Since the depth of the ice sheet changes per moon, two moons were considered in this study, Enceladus and Ganymede. The depth of Enceladus' ice shell was taken to be 25 km (Thomas et al., 2016), while Ganymede's ice thickness was taken as 150 km (Schenk, 2002).

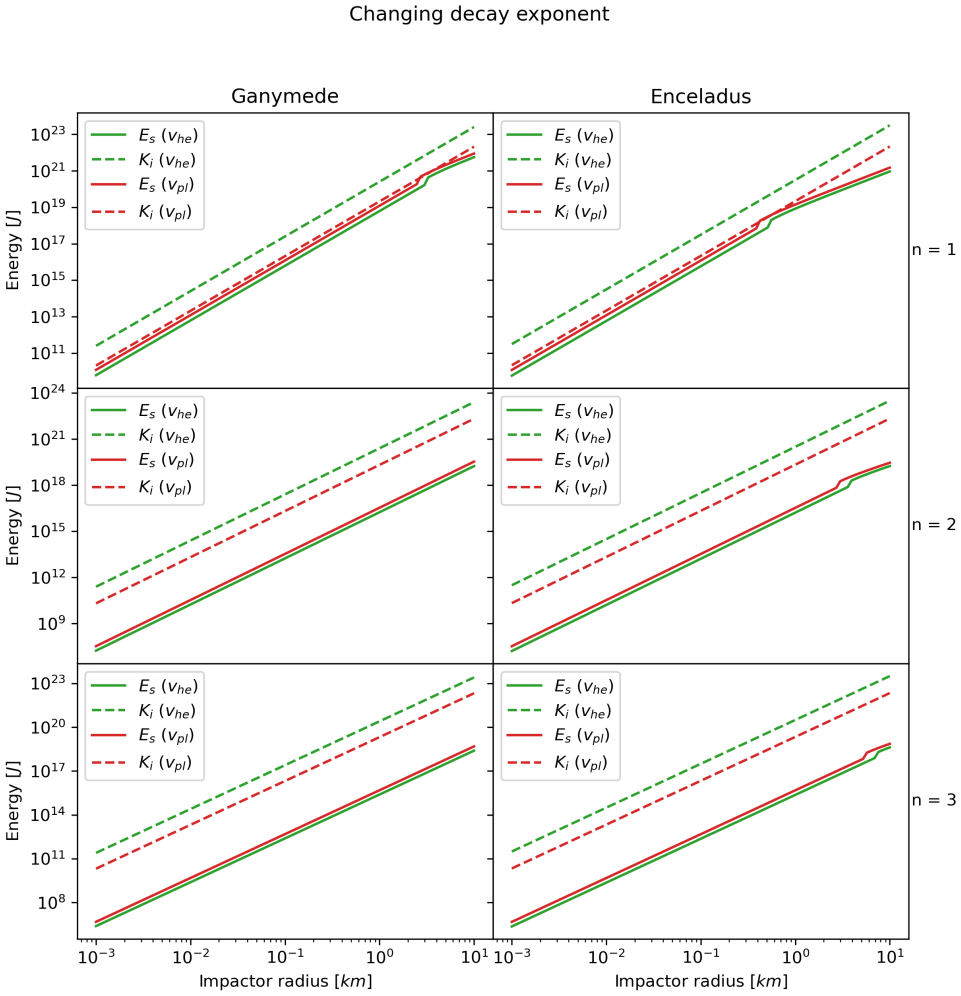

Figure 7.13: Required shattering energy (E_s) and impactor kinetic energy (K_i) compared to impactor radius for Ganymede and Enceladus. Each row represents a different decay exponent. Plots obtained with impactor density of 300 kg/m^3. Impact velocities (both heliocentric (V_{he}) and planetocentric (V_{pl})) are moon-dependant and are obtained from Table 2.1.

Using the information given above, a plot of energy versus impactor diameter can be made. Figure 7.13 shows the required shattering energy for the heliocentric and planetocentric velocities as shown in Table 2.1 (E_s, indicated by a continuous line), along with the kinetic energy of the impactor (K_i indicated by a dashed line).

Looking at Figure 7.13 and analyzing the equations, it can be noted that both curves for the kinetic and required shattering energy proportionally to R^3 until $R > D$, at which point the required shattering

energy scales proportionally to R^2. However, an interesting difference between the two curves is that the kinetic energy increases for increasing velocity, while the required shattering energy decreases due to the scaling of the isobaric core (Kraus et al., 2011). From Figure 7.13 it is clear that the kinetic energy of the impactor is always greater than the required shattering energy when the decay exponent is above 2. For the case where $n = 1$, the impactor's kinetic energy is always greater than the required shattering energy in the heliocentric case. However, that is not the case for the planetocentric case where the kinetic energy line is below the required shattering energy just when the shock wave reaches the bottom of the ice shelf. When that happens the shattering energy per kilogram goes from 25 J/kg to 50 J/kg, this is done to reflect the effect of the foam that was found in subsection 6.2.1. If the same energy of 50 J/kg is used regardless of how deep the shock wave propagates, the impactor kinetic energy will be below the required shattering energy until the radius of the impactor becomes large enough (just like in the case shown in Figure 7.13). However, the only way to get the kinetic energy low enough that it is ever below the required shattering energy is to use a low density for the impactor body. In Figure 7.13, the impactor density is taken to be 300 kg/m^3 (the minimum value discussed in subsection 7.3.1), however, if a larger value is taken, the kinetic energy will always be greater than the required shattering energy. On the other hand, one must take into account that not all of the kinetic energy from the impactor goes into the ice, meaning the lines could intercept once again.

Figure 7.14: An image of the surface of Ganymede, with many impact craters and no sign of ice shattering. Image Credit: NASA/JPL/ESA/ASI.

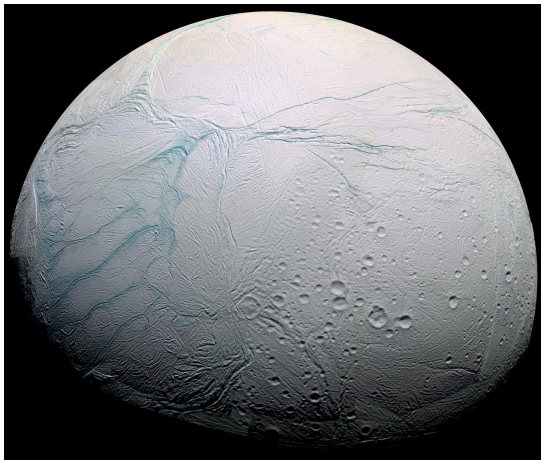

Figure 7.15: An image of the surface of Enceladus from the Cassini-Huygens space probe, with some impact craters visible but no sign of ice shattering. Image Credit: NASA/JPL.

These results seem to point out that except for a very small window in the case where $n = 1$, the surface of icy moons will always shatter no matter the origin of the impactor. However, this is not what is observed on the icy moons as it can be seen in Figures 7.14 and 7.15. This means that either there is an issue in the model, or the shattering is not visible on the moons (less likely). If the model is incorrect the most likely cause is the simplistic approach to measuring the volume of surface involved in the impact. Despite the shortcomings of this model, one conclusion that can be drawn is that it is more likely that there is less shattering for planetocentric impacts compared to heliocentric ones as the distance between the shattering energy and impact energy is smaller for the planetocentric case. In other words, in the planetocentric case, the required shattering energy for a given impactor diameter is larger than for the heliocentric case, while the kinetic energy is smaller compared to the heliocentric case.

8

Conclusion and Recommendation

This chapter wraps up this thesis with conclusions and recommendations for future works. The first section summarizes the findings of this thesis and section 8.2 discusses recommendations for future work.

8.1. Conclusions

The answers to the questions formulated in section 2.5 are summarized in this section. Separate answers are given for each sub-question, before answering the overall research question.

1. **What effect does the impactor diameter have on the characteristic of the crater?**
   In the laboratory setting, large-diameter impactors have been found to produce craters with a low degree of success. This low success rate can be attributed to two different reasons, depending on the type of material tested. For a more solid material like ice, the issue with a large impactor stems from its inability to completely penetrate the surface, meaning that what is created is not an impact crater but rather a small depression in the material. This effect can be seen in subsection 7.1.1, where for the largest 50 mm impactor there appears to be a negative correlation between impact energy and impactor diameter. For more loosely-bound materials, such as cement powder or icy particles, the issue arises from the fact that the minimum crater diameter is heavily constrained by the impactor diameter. While this does not matter for impacts with higher impact energy, it does matter for low-energy impacts as the crater diameter seems to stay almost unchanged around the impactor diameter.

2. **What effect does dampening foam have on impact craters?**
   As the name suggests, dampening foam is used to dampen an impact in the laboratory setting. Because part of the energy is temporarily stored in the foam, impact craters created with foam underneath the sample increase in size slower, compared to their undamped counterparts, when compared to the kinetic energy of the impactor. Since every impact has a certain crater efficiency, or the amount of energy that goes into making a crater, adding dampening foam acts to decrease that efficiency by absorbing some of the energy.

   The dampening foam has the additional effect of increasing the shattering energy. The dampening foam almost doubles the required shattering energy for one kilogram of ice, also making it a good way to perform impact tests with higher impact energies without risking shattering the ice.

3. **Do different materials (e.g. sand, ice, etc.) result in different crater characteristics?**
   Different materials have been found to behave very differently and one of the main drivers of this difference is the shear strength of the material. This behavior was particularly targeted in some experiments performed in cement, discussed in section 5.3. During those experiments, the compaction pressure of the material was used as a proxy for shear strength (see subsection 5.2.2 for the reason) and those experiments demonstrated that upon reaching a certain compaction strength the cratering was strength-dominated rather than gravity-dominated.

At low impact energies, such as the ones at which the experiments were performed, craters formed differently depending on the material. Ice, being one solid block, shattered either partially or completely upon impact which resulted in two features not present on craters formed on cement powder or icy particles. The first is the presence of fracture lines propagating from the center of the impact and the second is a more jagged look of the crater walls. Icy particles also have a unique characteristic when impacted upon. Particles tend to melt together during an impact, however, it is unclear if the melting is due to the energy added to the system via the impact, thermal energy from the impactor itself, or a combination of both.

4. **Can the depth to diameter ratio of craters be used to validate laboratory craters?**
   The depth to diameter ratio has been found to be a great tool to determine the validity of impact craters created in the laboratory. Impacts that resulted in shallow craters ($d/D < 0.25$) usually do not have enough energy to break the ice, therefore resulting in an indent on the surface rather than an actual crater. On the other hand, deep craters ($d/D > 0.5$) are a result of either the ice cracking all the way to the bottom of the sample, therefore allowing the projectile to penetrate further, or of the projectile creating a crater deeper than 70% of the sample depth which often produces erroneous results. Therefore craters that lie outside the selected range on $0.25 < d/D < 0.5$ can most likely be excluded from valid craters.

5. **Can laboratory experiments be used to infer impactor diameter or velocity for impacts on icy moons?**
   Experiments from this work were used to develop scaling relationships both in the energy-diameter and π spaces. The π scaling relationships were then used, together with estimated impact energies for heliocentric and planetocentric impactors, to determine the impactor diameter from a given crater on icy moons. Using this method, it was found that there is a significant difference in impactor diameter for heliocentric and planetocentric impactors. However, more research is needed to improve the predictions to know whether heliocentric or planetocentric impactors can be ruled out.

   Data from this work was also used to determine the energy per kilogram of ice required to shatter a surface. This data was then applied to icy moons to see if shattering behavior could be predicted for the surface of these icy moons. While the model always predicted shattering (which is not observed on the icy moons), the difference between the required shattering energy and the impactor energy was much smaller for planetocentric impactors compared to heliocentric ones, suggesting planetocentric impactors are less likely to shatter an icy surface.

   "Can the impact velocity be determined for impactors on icy moons based on crater characteristics, such as crater depth and diameter, by recreating impacts in the lab?"

This work has looked at various crater parameters such as crater diameter and crater depth. The influence of different factors during the impact process was also analyzed to observe how the crater formation behaves under different circumstances. The results obtained in the experiments were then applied to the icy moons by analyzing the estimated required shattering energy given an impactor of a given size. From the results obtained in the laboratory, it appears that the ice will always shatter which is not what is observed. However, given the assumptions stated in section 7.5, it is more likely that no, or less, shattering occurs in the planetocentric case compared to the heliocentric case since the kinetic energy of a planetocentric impactor is lower and the required shattering energy is higher, compared to the heliocentric case. The results obtained in the lab were also used to estimate the impactor diameter for given craters on Ganymede and Enceladus. However, even the best results showed required impactor diameters in the same order of magnitude of the crater, resulting in the impactor size estimate for Ganymede around 100 km which is unlikely as only very few objects exist in the Solar System which are that large and have the required orbital velocity. For Enceladus the required impactor size is smaller, around 10 km across, however, the distinction between planetocentric and heliocentric velocities is not enough to draw any solid conclusions. Therefore, from the results obtained in this work, it appears that the velocity of impactors on icy moons cannot be determined with the results obtained. However, the recommendations laid out in section 8.2 could help in answering the research question.

8.2. Recommendations

The results of the work done in this thesis could be further investigated in studies following this one. Each section describes one of the possible further investigations, ordered from least to most complex, as of the writing of this thesis. Subsection 8.2.1 describes how the impact energy range can be expended for both the drop tower and gas gun. This is followed by subsection 8.2.2 which describes how more sample could be produced in the case of icy particles. The last two sections both have to do with observations, where subsection 8.2.3 describes how to improve the quality of current observations, subsection 8.2.4 presents the methods available to detect ice transition in the sample.

8.2.1. Extending impact energy range

The experiments performed in this work were executed in a limited energy range, limited both at the minimum and maximum impact energy by both machines. To extend the available energy range of the drop tower one solution would be creating an impact rod (see Figure 3.1 for description) without the attached cable to allow the impactor to be dropped from significantly higher. Since the drop tower is much taller than the current 2.5 m limitation, this would allow achieving impact energies in the order of 100 J as it can be seen in Figure 8.1. This new rod design could also remove the large disk above the tip, meaning that even smaller tips could be used, without worrying the disk could ruin the experiment. Decreasing the impact head diameter reduces the value of the π_2 dimensionless scaling parameter making it more in line with real-world situations. The energy range of the gas gun can be increased by

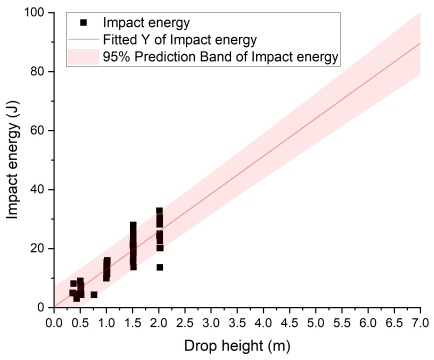

Figure 8.1: Proposed extended energy range for drop tower, for a 2 kg impactor, as a function of drop height.

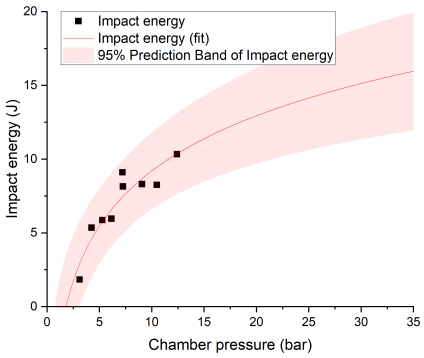

Figure 8.2: Proposed extended energy range for gas gun, with a 2 g impactor (8 mm diameter) as a function of chamber pressure.

improving the nozzle configuration. The current muzzle supports projectiles that are 25 mm in diameter, allowing for only one impactor diameter. The solution used in this work to use an adaptor could be modified to make the gas gun able to shoot different projectiles and shoot them faster. The projectile's speed is greatly reduced if the projectile diameter is smaller than the nozzle diameter as air rushes in front of the projectile when the valve is opened. By using different nozzle adaptors a wider range of impactor diameters can be used and the efficiency of the shot can be maximized (or the wasted air minimized). Figure 8.2 shows the projected impact energy for higher chamber pressure, however, this estimate does not take into account the new nozzle, which will most likely increase the impact energy as the velocity would be higher.

8.2.2. Increasing sample quantity

One of the issues experienced with the experiments in icy particles was the lack of sample material. Since all the particles were made by hand, producing $\approx$1 kg of it took almost 3 hours. Combining this with the fact that the pressurized container could not be left in the lab overnight, meaning that experiments done using icy particles were limited in the amount of sample available. To increase the amount of available sample material a semi-automatic system could be implemented to create the icy particles. This system would consist of a nozzle to spray the water in the LN_2 bath and a system to resupply the LN_2 when it runs out. A system like the one shown in Figure 8.3 could be used. This system would have the following advantages.

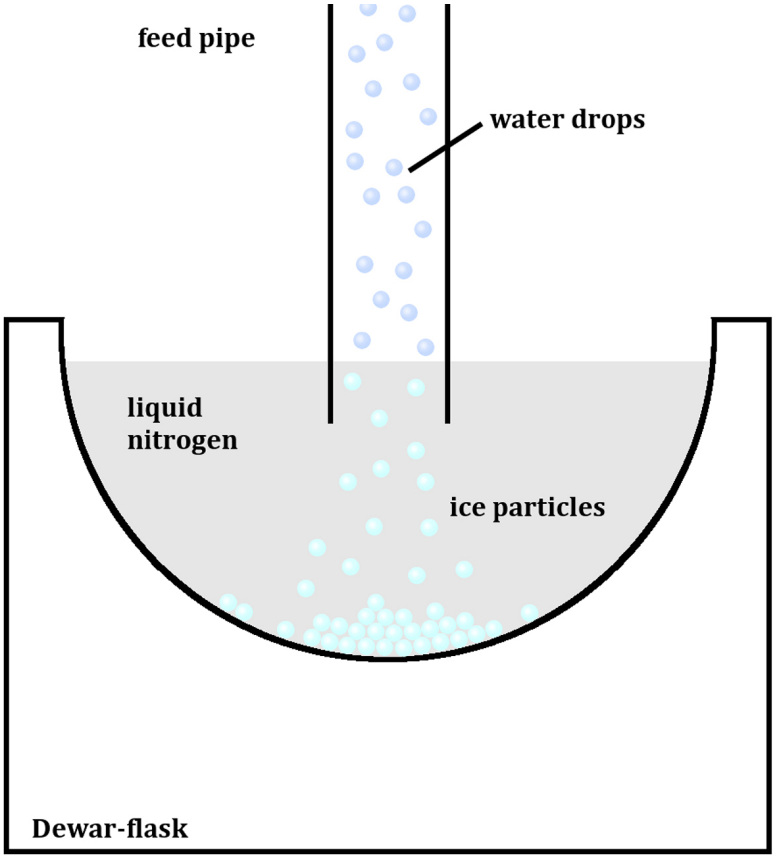

Figure 8.3: Simple schematic of semi-automatic icy particles maker. Image credit: Häßner et al. (2018).

- **Better particle consistency**:
  Using a pump-fed nozzle to spray the water would result in much more consistent water droplet sizes and shapes which would then turn into more consistent icy particles.
- **continuos operation**:
  Having an automated system allows for no pauses during ice production which will allow producing more ice per hour compared to a person manually spraying the water.
- **Longer operation**:
  Using this system will allow keeping the ice production going for longer, allowing it to produce much more ice than previously possible.
- **Control over particle size**:
  Using this setup could also allow exchanging nozzle types to allow for different water droplets sizes which in turn would produce icy particles with different diameters.
- **Better control over produced quantity**:
  By measuring the water used, the amount of produced ice mass can be estimated with more precision, allowing to ask the system for a specific amount of mass, instead of producing a semi-arbitrary amount of ice.

This system would allow for testing ice for the full depth of the steel container ($\approx$22 cm) which will be necessary if the impact energy is to be increased. Using more sample will also produce more reliable results as it will decrease the interaction between the shock wave and table.

8.2.3. Improving quality of observations

Uncertainty is an inevitable part of every experiment, however, two things could be done for future experiments to decrease some of the uncertainties observed in this work. Adding a couple of laser

sensors to the gas gun would allow knowing the impact velocity with a much higher degree of certainty compared to the camera used currently. This will not only improve the knowledge of the impact speed, and therefore impact energy, but will also free up the camera to measure the impact from a different angle where more information on the impact itself can be seen, like in the footage captured for the drop tower.

A camera mounted on a rotating crane could be used to image the impact crater from different angles and produce a virtual reproduction of the crater. A similar effect could also be achieved by using one distance sensor which moves across the surface and measures the depth at each point (or an array of sensors would do the same). Either of these methods would allow measuring the crater volume with much better precision compared to the current method of estimating it based on the crater diameter and depth. Using this sort of imaging system will also allow measuring the crater diameter even when doing so by hand is complicated like in the case of the surface being lower down in the container.

8.2.4. Detecting ice transition

One of the reasons for producing icy particles by spraying water directly into a pool of LN_2 is to produce some amorphous ice. This ice is different from crystalline ice and the difference between these two types could be used to further study impact craters on icy moons. Therefore future experiments could look at the behavior of amorphous ice during or after an impact. The setup for the experiment can be similar to the other ones done with icy particles in this work with one change. Different materials should be tested for the impactor as materials with higher thermal conductivity will transfer more of their thermal energy to the ice compared to materials with lower thermal conductivity. This means that for a material like steel, the ice will be heated not only by the impacts but also by the impactor itself, while if a material like Pyrex is used this effect will be smaller. After the impact, the ice should be analyzed to detect the fraction of amorphous to crystalline ice and compare it to before the impact. Key points in the impact should be analyzed, such as the crater rim, pit, (eventual) central dome, and crater walls. This will allow to also study how the distribution of amorphous ice varies after an impact. One way to detect crystalline and amorphous ice is by using infrared spectroscopy as the two types of ice have different spectra as shown in Figure 8.4. Other methods use either electron or x-ray diffraction to achieve the same result as was done by Jenniskens and Blake (1994b) and Mishima et al. (1984).

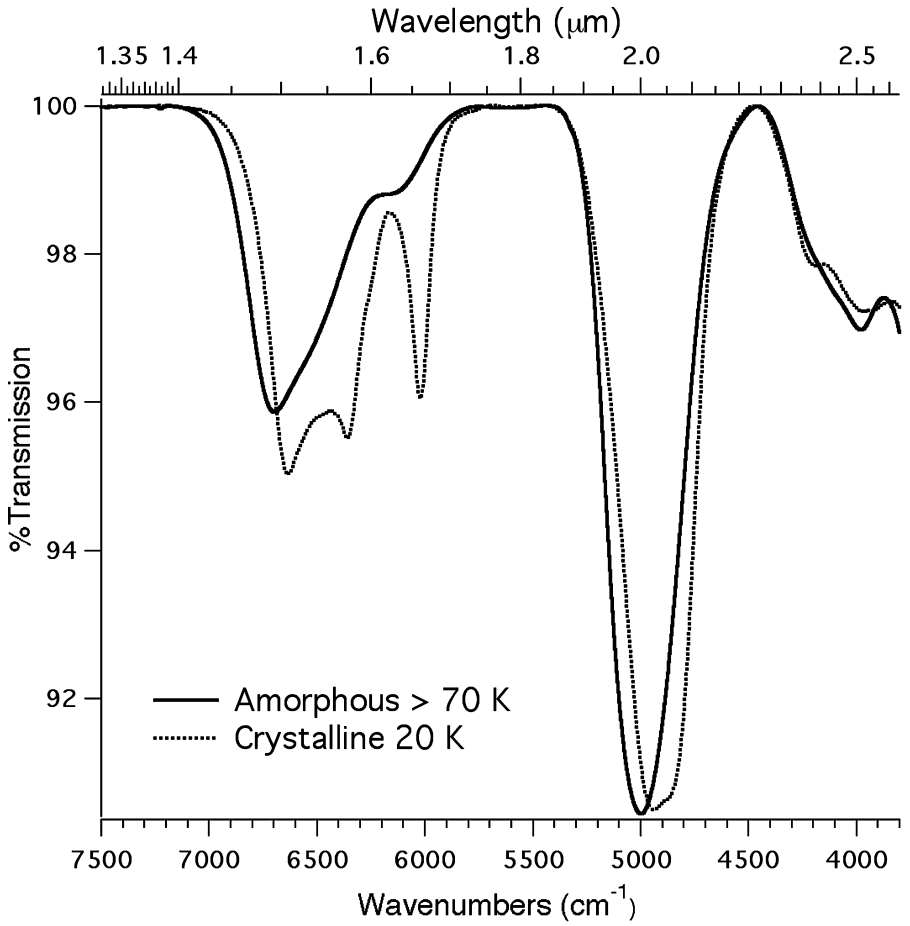

Figure 8.4: Comparison of amorphous and crystalline H2O-ice. The 20 K crystalline spectrum (dotted line) has stronger bands near 6600 cm^{-1} (1.5 μm), 6400 cm^{-1} (1.56 μm), and 6050 cm^{-1} (1.65 μm). The >70 K amorphous H2O-ice (solid line) has a slightly stronger near 4900 cm^{-1} (2.0 μm) and all amorphous bands are shifted to shorter wavelength when compared to the crystalline bands (Mastrapa et al., 2008).

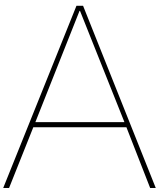

Drop Tower LogBook

This page was intentionally left blank.

ID	Date	Time	SurfaceID	RodMass [g]	HeadMass [g]	WeightsMass [g]	ImpactorMass [g]	DropHeight [mm]	Hprime [mm]	ContainerID	SampleVolume [L]	Volume_error [L]	ContainerM [g]	TotalM0 [g]	TotalM1 [g]	Mass loss [g]	Density [kg/m^3]	Density_error [kg/m^3]	V0 [m/s]	V1 [m/s]
0001	2021_09_15	16_03	1	1449.8	86.5	601	2137.3	1002	26	Tupperware	0.350949			500.48	500.48	0	1426.076154		0	0.199836	3.55663
0002	2021_09_20	11_34	1	1449.8	86.5	601	2137.3	1003	63	Tall Cylinder	0.7080773			1014.69	1011.27	3.42	1433.021508		0	0.436244	3.23924
0003	2021_09_20	12_10	1	1449.8	86.5	601	2137.3	1002	68	Tall Cylinder	0.6552357			1011.27	1007.36	3.91	1543.368287		0	-0.01124	3.67609
0004	2021_09_20	12_28	1	1449.8	86.5	601	2137.3	1004	70	Tall Cylinder	0.6340991			1007.36	1005.25	2.11	1588.647579		0	0.262425	3.63408
0005	2021_09_20	12_40	1	1449.8	86.5	601	2137.3	1016	50	Tall Cylinder	0.8454654			1174.83	1154.9	19.93	1389.566031		0	0.432661	3.5286
0006	2021_09_20	13_00	1	1449.8	86.5	601	2137.3	1019	54	Tall Cylinder	0.8031921			1165.83	1149.05	16.78	1451.49585		0	0.412271	3.59114
0007	2021_09_22	15_00	1	1449.8	69	601	2119.8	1015	55	Tall Cylinder	0.7926238			1149.38	1148.52	0.86	1450.095241		0	-0.038898	3.7816
0008	2021_09_29	14_08	3	1449.8	69	601	2119.8	1508		3D printed						0	#DIV/0!	#DIV/0!		-0.031006	4.74417
0009	2021_09_29	14_42	1	1449.8	69	601	2119.8	1515	31	Bowl	1.35			1287.7	1269	18.7	953.8518519		0	0.340824	4.6849
0010	2021_09_29	15_35	1	1449.8	69	601	2119.8	1006	35	Bowl	1.22			1269	1252.5	16.5	1040.163934		0	0.143008	3.50755
0011	2021_10_04	10_53	1	1449.8	69	601	2119.8	1005	40	Bowl	1.07			1247.57	1245.46	2.11	1165.953271		0	0.20521	3.34522
0012	2021_10_04	11_49	1	1449.8	69	601	2119.8	510	40	Bowl	1.07			1245.46	1245.21	0.25	1163.981308		0	0.547508	2.19179
0013	2021_10_04	12_04	1	1449.8	69	1201	2719.8	1519	45	Bowl	0.93			1245.21	1242.02	3.19	1338.935484		0	0.0598928	4.48163
0014	2021_10_04	13_33	1	1449.8	69	1201	2719.8	1005	38	Bowl	1.13			1242.02	1237.62	4.4	1099.132743		0	-0.037527	3.89055
0015	2021_10_04	13_54	1	1449.8	69	1201	2719.8	1515	40	Bowl	1.07			1237.62		1237.62	1156.654206		0	-0.031564	4.64965
0016	2021_10_04	14_25	1	1449.8	69	1201	2719.8	1514	40	Bowl	1.07			1417.91	1405.09	12.82	1325.149533		0	-0.030142	4.88019
0017	2021_10_04	14_59	1	1449.8	69	1201	2719.8	1005	34	Bowl	1.26			1405.09	1396.04	9.05	1115.150794		0	-0.038411	3.8296
0018	2021_10_04	15_11	1	1449.8	69	1201	2719.8	508	42	Bowl	1.01			1396.04	1389.24	6.8	1382.217822		0	-0.062172	2.36455
0019	2021_10_15	14_40	1	1449.8	412.5	1201	3063.3	1002	N/A	Square	0.764		246	1311.95	1311.25	0.7	1395.222513		0	-0.042461	3.43324
0020	2021_10_15	15_00	1	1449.8	412.5	1201	3063.3	1519	N/A	Cylinder	1.15		325.17	1599.3	1596.8	2.5	1107.93913		0	-0.031772	4.62988
0021	2021_10_15	15_20	1	1449.8	412.5	1201	3063.3	1518	N/A	Cylinder	1.15		325.17	1596.8	1594.14	2.66	1105.765217		0	-0.033735	4.36047
0022	2021_10_19	11_22	2	1449.8	412.5	1201	3063.3	1513	N/A	Square	1.671	0.12	246	1827.15	1751.2	75.95	946.2298025	67.95187092	-0.032458	4.53177
0023	2021_10_19	14_24	2	1449.8	412.5	1201	3063.3	1514	N/A	Square	1.671	0.12	246	1872.36	1825.5	46.86	973.2854578	69.89482641	-0.032981	4.46012
0024	2021_10_19	15_00	2	1449.8	412.5	1201	3063.3	2020	N/A	Square	1.671	0.12	246	1816.77	1603.2	213.57	940.0179533	67.50577762	-0.027521	5.3449
0025	2021_10_19	16_10	2	1449.8	412.5	1201	3063.3	2030	N/A	Square	1.671	0.12	246	1986.4	1979.6	6.8	1041.532017	74.79583603	N/A	N/A	
0026	2021_10_25	17_30	2	1449.8	412.5	1201	3063.3	1512	N/A	Square	1.671	0.12	246	2008.6	2003.5	5.1	1054.817475	75.74990841	N/A	N/A	
0027	2021_10_27	10_43	2	1449.8	412.5	1201	3063.3	503	N/A	Square	1.671	0.12	246	2250.5	2249.8	0.7	1199.581089	86.14585919	0.524059	2.4901	
0028	2021_10_27	11_10	2	1449.8	412.5	1201	3063.3	504	N/A	Square	1.671	0.12	246	1903.2	1898.2	5	991.7414722	71.22021344	0.53879	2.42853	
0029	2021_10_27	11_22	2	1449.8	412.5	1201	3063.3	1005	N/A	Square	1.671	0.12	246	1871.56	1864.55	7.01	972.8067026	69.86044543	0.418045	3.43748	
0030	2021_10_27	11_36	2	1449.8	412.5	1201	3063.3	1514	N/A	Square	1.671	0.12	246	1859.9	1791.35	68.55	965.828845	69.35934255	0.33377	4.96056	
0031	2021_10_27	11_50	2	1449.8	412.5	1201	3063.3	2015	N/A	Square	1.671	0.12	246	1820.8	1664.5	156.3	942.4296828	67.67897184	0.251271	5.48211	
0032	2021_10_27	13_38	2	1449.8	412.5	1201	3063.3	507	N/A	Square	1.671	0.12	246	1924	1921	3	1004.189108	72.11411909	-0.0487	2.41085	
0033	2021_10_27	13_55	2	1449.8	412.5	1201	3063.3	1002	N/A	Square	1.671	0.12	246	1893	1889.12	3.88	985.6373429	70.78185586	-0.038721	3.50936	
0034	2021_10_27	14_13	2	1449.8	412.5	1201	3063.3	1514	N/A	Square	1.671	0.12	246	1901.8	1887.85	13.95	990.9036505	71.16004672	-0.030452	4.43474	
0035	2021_10_27	14_29	2	1449.8	412.5	1201	3063.3	2018	N/A	Square	1.671	0.12	246	1851.45	1741.05	110.4	960.7719928	68.99619338	-0.025791	5.46999	
0036	2021_10_27	15_08	2	1449.8	412.5	1201	3063.3	507	N/A	Square	1.551	0.208	246	1834.47	1833.25	1.22	1024.158607	137.3468667	-0.062124	2.36206	
0037	2021_10_27	15_26	2	1449.8	412.5	1201	3063.3	1003	N/A	Square	1.551	0.208	246	1809.59	1807.66	1.93	1008.117344	135.1956206	-0.038277	3.80538	
0038	2021_10_27	16_02	2	1449.8	412.5	1201	3063.3	1505	N/A	Square	1.551	0.208	246	1778.9	1774.25	4.65	988.3301096	132.5420134	-0.031777	4.62528	
0039	2021_10_27	16_18	2	1449.8	412.5	1201	3063.3	2017	N/A	Square	1.551	0.208	246	1819	1803.7	15.3	1014.184397	136.0092551	-0.02754	5.34119	
0040	2021_10_28	10_22	2	1449.8	412.5	1201	3063.3	515	N/A	Square	1.166	0.187	246	1604.75	1602.36	2.39	1165.308748	186.8891388	-0.064156	2.29282	
0041	2021_10_28	10_39	2	1449.8	412.5	1201	3063.3	1011	N/A	Square	1.166	0.187	246	1602.95	1602.77	0.18	1163.765009	186.641558	0.399574	3.37198	
0042	2021_10_28	11_00	2	1449.8	412.5	1201	3063.3	1513	N/A	Square	1.166	0.187	246	1601.85	1601.68	0.17	1162.821612	186.4902586	0.155082	4.17816	
0043	2021_10_28	11_15	2	1449.8	412.5	1201	3063.3	2015	N/A	Square	1.166	0.187	246	1605.75	1605.1	0.65	1166.166381	187.0266837	0.0884049	4.84353	
0044	2022_01_21	15_30	3	1449.8	412.5	1201	3063.3	460	N/A	Plastic AH	0.8	0.1	36.6	671.99	0	671.99	794.2375	99.2796875	-0.065736	2.2377	
0045	2022_01_21	15_50	3	1449.8	412.5	1201	3063.3	1010	N/A	Plastic AH	0.8	0.1	36.6	586.11	0	586.11	686.8875	85.8609375	0.321874	3.59968	
0046	2022_01_21	16_05	3	1449.8	412.5	0	1862.3	508	N/A	Unconstrained	0.8	0.1	36.6	603.48	0	603.48	708.6	88.575	0.526333	2.19406	
0047	2022_01_21	16_19	3	1449.8	412.5	0	1862.3	373	N/A	Unconstrained	0.8	0.1	36.6	595.93	0	595.93	699.1625	87.3953125	1.18665	1.66813	
0048	2022_01_21	16_32	3	1449.8	69	0	1518.8	355	N/A	Unconstrained	0.8	0.1	36.6	566.28	0	566.28	662.1	82.7625	0.656968	1.57368	
0049	2022_01_21	16_49	3	1449.8	545.5	0	1995.3	355	N/A	Unconstrained	0.8	0.1	36.6	599.74	0	599.74	703.925	87.990625	0.615791	1.60205	
0050	2022_01_31	16_20	3	1449.8	69	0	1518.8	764	N/A	Square	1.343	0.21	246	1438.1	1437.2	0.9	887.6396128	138.796961	-0.06812	2.15451	
0051	2022_01_31	17_10	3	1449.8	69	0	1518.8	1000	N/A	Square	1.343	0.21	246	1437.2	1435.8	1.4	886.9694713	138.6921735	-0.046025	3.19605	
0052	2022_02_09	11_43	3	1449.8	69	0	1518.8	1515	N/A	Thermal	1.671	0.21	289	1442.5	1402	40.5	690.3052065	86.75289848	-0.035443	4.1333	
0053	2022_02_09	12_12	3	1449.8	69	0	1518.8	2022	N/A	Thermal	1.671	0.21	300.5	1380.5	1345	35.5	646.3195691	81.2250805	-0.039397	3.73371	
0054	2022_02_09	12_28	3	1449.8	69	600.5	2119.3	2020	N/A	Thermal	1.671	0.21	302	1411.5	1373.5	38	663.9736685	83.44372853	-0.029202	5.03725	
0055	2022_02_10	15_23	3	1449.8	281.5	600.5	2331.8	1517	N/A	Thermal	1.671	0.21	300.5	1090.5	1091	-0.5	472.7707959	59.41464222	-0.033507	4.39007	
0056	2022_02_10	15_48	3	1449.8	281.5	600.5	2331.8	1519	N/A	Thermal	1.671	0.21	289	1250	1249.5	0.5	575.1047277	72.27527996	-0.039255	3.74718	
0057	2022_02_10	16_04	3	1449.8	281.5	600.5	2331.8	2022	N/A	Thermal	1.671	0.21	302	1268	1257.5	10.5	578.0969479	72.651322	-0.030731	4.78664	
0058	2022_02_14	11_30	3	1449.8	281.5	600.5	2331.8	2022	N/A	Thermal	1.671	0.21	300.5	1291	1286.5	4.5	592.758827	74.493928	-0.030358	4.82123	
0059	2022_02_14	11_54	3	1449.8	281.5	1801.5	3532.8	2023	N/A	Thermal	1.671	0.21	289	1210.5	1198.5	12	551.4661879	69.30454785	-0.027073	5.43348	
0060	2022_02_14	12_15	3	1449.8	69	0	1518.8	2020	N/A	Thermal	1.671	0.21	302	1277	1275	2	583.4829443	73.32819767	0.235709	5.29551	
0061	2022_02_25	16_06	4	1449.8	412.5	0	1862.3	1012	N/A	Thermal			302			0	234	58	-0.042305	3.47711	
0062	2022_02_25	16_15	4	1449.8	412.5	0	1862.3	1511	N/A	Thermal			302			0	234	58	-0.036919	3.98434	
0063	2022_02_25	16_28	4	1449.8	412.5	0	1862.3	517	N/A	Thermal			302			0	234	58	-0.62315	2.12723	
0064	2022_04_20	14_59	4	1449.8	412.5	0	1862.3	1014	N/A	Thermal	1.671	0.21	N/A	N/A	N/A	#VALUE!	234	58	-0.042079	3.48408	
0065	2022_04_20	15_16	4	1449.8	412.5	0	1862.3	519	N/A	Thermal	1.671	0.21	N/A	N/A	N/A	#VALUE!	234	58	-0.068189	2.1572	
0066	2022_04_20	15_52	4	1449.8	412.5	0	1862.3	433	N/A	Thermal	1.671	0.21	N/A	N/A	N/A	#VALUE!	234	58	-0.080472	1.82795	
0067	2022_05_03	15_48	4	1449.8	412.5	0	1862.3	514	N/A	Steel	N/A	N/A	N/A	N/A	N/A	#VALUE!		#VALUE!	N/A	N/A	
0068	2022_05_03	15_53	4	1449.8	412.5	0	1862.3	1000	N/A	Steel	N/A	N/A	N/A	N/A	N/A	#VALUE!		#VALUE!	N/A	N/A	
0069	2022_05_03	16_01	4	1449.8	412.5	0	1862.3	1514	N/A	Steel	N/A	N/A	N/A	N/A	N/A	#VALUE!		#VALUE!	N/A	N/A	
0070	2022_05_03	16_18	4	1449.8	412.5	0	1862.3	2020	N/A	Steel	N/A	N/A	N/A	N/A	N/A	#VALUE!		#VALUE!	N/A	N/A	
0071	2022_05_03	16_23	4	1449.8	412.5	600	2462.3	1517	N/A	Steel	N/A	N/A	N/A	N/A	N/A	#VALUE!		#VALUE!	N/A	N/A	
0072	2022_05_03	16_30	4	1449.8	412.5	600	2462.3	1015	N/A	Steel	N/A	N/A	N/A	N/A	N/A	#VALUE!		#VALUE!	N/A	N/A	

ImpactVelocity [m/s]	PeakForce [N]	Impact Energy [	Crater diameter [mm]	sigma_D [mm]	Crater depth [mm]	Compaction	Notes
3.75647	28548	15.0797916	#DIV/0!	#N/A	#N/A		
3.67549	22778.9	14.43663516	60	#N/A	#N/A		
3.64485	15379	14.19694207	55	#N/A	#N/A		
3.89651	7610	16.22508873	55	#N/A	#N/A		
3.9612	7504.83	16.76829983	61.5	#N/A	#N/A		
4.00341	6155.4	17.1275652	#DIV/0!	#N/A	#N/A		
3.7427	2961.55	14.84687071	#DIV/0!	#N/A	#N/A		
4.71316	2596.16	23.54448843	70	#N/A	#N/A		
5.02572	3346.16	26.77080742	74	#N/A	#N/A		
3.65056	31403.9	14.12485095	#DIV/0!	#N/A	#N/A		
3.55053	23601	13.36137845	66	#N/A	#N/A		
2.7373	14182.7	7.941630686	#DIV/0!	#N/A	#N/A		
4.54152	14730.8	28.04848678	#DIV/0!	#N/A	#N/A		
3.85302	41327	20.18875327	69	#N/A	#N/A		
4.61809	3250.01	29.00225446	#DIV/0!	#N/A	#N/A		
4.85005	16467	31.9889073	#DIV/0!	#N/A	#N/A		
3.79118	34990.5	19.54590497	90	#N/A	#N/A		
2.30238	17913.5	7.208766888	75	#N/A	#N/A		
3.39078	10187.5	17.60997587	45	#N/A	#N/A		
4.59811	25423.2	32.38308714	60	#N/A	#N/A		
4.32673	26605.8	28.67339549	70	#N/A	#N/A		
4.49931	20062.6	31.00640168	120	#N/A	#N/A		
4.42714	28533.7	30.01967921	90	#N/A	#N/A		
5.31738	11927.9	43.30668397	#DIV/0!	#N/A	#N/A		
4.5	N/A	31.0159125	80	#N/A	#N/A		
5.1	N/A	39.8382165	70	#N/A	#N/A		
3.01416	5322.13	13.91528609	52	#N/A	#N/A	No compaction	Invalid
2.9675	10735.6	13.48779606	66	#N/A	#N/A	No compaction	
3.85552	17793.3	22.76803005	72	#N/A	#N/A	No compaction	
5.29433	38269.3	42.93204251	125	#N/A	#N/A	No compaction	
5.73338	35038.6	50.34785694	152	#N/A	#N/A	No compaction	
2.36215	21966.4	8.546228104	75.5	#N/A	#N/A	A 17.5^2 cm2; m 0.7552 kg	
3.47064	32822.2	18.44924809	76	#N/A	#N/A	A 17.5^2 cm2; m 0.7552 kg	
4.40429	25110.7	29.71059504	95	#N/A	#N/A	A 17.5^2 cm2; m 0.7552 kg	
5.44419	17706.8	45.39688796	135	#N/A	#N/A	A 17.5^2 cm2; m 0.7552 kg	
2.29993	17192.4	8.101935316	69.5	#N/A	#N/A	A 17.5^2 cm2; m DT	
3.7671	25687.6	21.73571011	73	#N/A	#N/A	A 17.5^2 cm2; m DT	Catch mechanism pushed rod to left
4.5935	30827	32.31818604	80.5	#N/A	#N/A	A 17.5^2 cm2; m DT	
5.31365	28014.5	43.24594832	86	#N/A	#N/A	A 17.5^2 cm2; m DT	No camera footage
2.22867	9317.34	7.607659553	51.5	#N/A	#N/A	d = 70 mm; m = 5.0573 kg	
3.77155	6495.21	21.78709236	51	#N/A	#N/A	d = 70 mm; m = 5.0573 kg	
4.33324	9274.07	28.75974441	50.5	#N/A	#N/A	d = 70 mm; m = 5.0573 kg	
4.93194	12389.5	37.25590386	52.5	#N/A	#N/A	d = 70 mm; m = 5.0573 kg	
2.17196	2134.62	7.225421397	0	#N/A	#N/A		Ice shattered container, no data retrieved
3.92155	34024.1	23.55456285	0	#N/A	#N/A		Ice shattered container, no data retrieved
2.72938	504.809	6.936616064	0	#N/A	#N/A		Ice shattered, no data retrieved
2.85478	-326.924	7.588657263	0	#N/A	#N/A		Ice shattered, no data retrieved
2.23065	4129.82	3.778622081	0	#N/A	#N/A		Ice shattered, no data retrieved
2.21785	1360.58	4.907299305	0	#N/A	#N/A		Ice shattered, no data retrieved
2.08639	2365.39	3.305685842	25	1	0		
3.15002	668.271	7.535242185	46.75	8.757139944	0		
4.09786	2423.08	12.75219153	30.274	3.614551701	13.33		
3.69431	3528.86	10.36423529	16.4325	1.72769174	1.87		
5.00805	2293.28	26.57662049	59	2.788108678	37		Top ring impacted surface
4.35657	3152.86	22.12843475	36.33	2.064897092	21.29		
3.70792	2745.2	16.0295752	45.72666667	3.881858089	15.33		No foam
4.7559	2721.16	26.37100803	#DIV/0!	#DIV/0!	0		Ice shattered, no data retrieved; No foam
4.79088	3187.51	26.7603561	31.6	1	9		
5.40641	3605.78	51.63058092	#DIV/0!	#DIV/0!	0		Ice shattered, no data retrieved
5.53122	10495.2	23.23338333	48.6875	3.963485682	7.95		No foam
3.43481	8302.91	10.98563296	80.3875	5.813064489	21.8		No foam
3.94742	22437.6	14.50929537	120.5	9.969453345	0		No foam
2.75036	12086.6	7.043665673	75.935	1	19.14		No foam
3.442	19687.6	11.03167299	98.04	5.904447476	36.93		No foam
2.08901	14057.7	4.063503943	114.8366667	6.085969292	47.1		No foam
1.74748	14312.5	2.843440045	97.27	8.405768852	47.1		No foam
2.112709954	N/A	4.156228388	132.5	2.5	0		
3.173055958	N/A	9.37508275	142.5	2.5	0		
4.062776524	N/A	15.36970445	152.5	2.5	0		
4.493649669	N/A	18.80260705	161.6666667	2.357022604	0		
4.382960211	N/A	23.65081036	127.5	2.5	0		
3.373536434	N/A	14.01140799	125	5	0		

B

Gas Gun LogBook

This page was intentionally left blank.

ID	Date	Time	SurfaceID	Projectile size [mm]	ProjectileMass [g]	ChamberPressure (se	ChamberPressure [bar]2
0001	2021_11_08	10:57	Ice		30.37		2.8
0002	2021_11_12	15:24	Ice		30.37		4.36
0003	2021_11_17	16:14	dampener		#N/A		
0004	2021_11_17	16:24	dampener		#N/A		
0005	2021_11_18	10:30	dampener		#N/A		
0006	2021_11_18	10:57	dampener		#N/A		
0007	2021_11_18	11:06	dampener		#N/A		
0008	2021_11_18	11:18	dampener		#N/A		
0009	2021_12_10	15:55	dampener	8	2.035		2.74
0010	2021_12_10	16:05	dampener	8	2.035		2.79
0011	2021_12_10	16:13	dampener	8	2.035		2.8
0012	2021_12_10	17:09	dampener	8	2.035		1.73
0013	2022_01_13	16:10	Ice		0.5102		
0014	2022_01_13	16:51	Ice		0.5102		
0015	2022_01_26	10:42	dampener	8	2.035		1.79
0016	2022_01_26	11:15	dampener	8	2.035		1.78
0017	2022_01_26	11:24	dampener	8	2.035		3.53
0018	2022_01_26	11:30	dampener	8	2.035		7.02
0019	2022_01_26	11:34	dampener	8	2.035		6.8
0020	2022_02_24	11:17	Ice	8	2.035	5.28	5.46
0021	2022_02_24	11:50	Ice	8	2.035	6.15	6.33
0022	2022_02_24	12:16	Ice	8	2.035	7.2	7.38
0023	2022_02_24	15:47	Ice	8	2.035	7.25	7.43
0024	2022_02_24	16:25	Ice	8	2.035	3.11	3.29
0025	2022_02_24	16:40	Ice	8	2.035	4.25	4.43
0026	2022_02_25	10:20	Ice	8	2.035	12.41	12.59
0027	2022_02_25	10:37	Ice	8	2.035	10.49	10.67
0028	2022_02_25	11:09	Ice	8	2.035	9.07	9.25

Container	Volume [L]	Volume Error [L	ContainerM [g]	TotalM0 [g]	TotalM1 [g]	MassLoss [g]	Density [kg/m^3]
3D printed box			98			0	#DIV/0!
3D printed box			102	677.56		677.56	#DIV/0!
3D printed box						0	#DIV/0!
3D printed box						0	#DIV/0!
3D printed box						0	#DIV/0!
3D printed box						0	#DIV/0!
3D printed box						0	#DIV/0!
dampener			N/A	N/A		#VALUE!	#VALUE!
dampener			N/A	N/A		#VALUE!	#VALUE!
dampener			N/A	N/A		#VALUE!	#VALUE!
dampener			N/A	N/A		#VALUE!	#VALUE!
IKEA						0	#DIV/0!
IKEA						0	#DIV/0!
dampener			N/A	N/A		#VALUE!	#VALUE!
dampener			N/A	N/A		#VALUE!	#VALUE!
dampener			N/A	N/A		#VALUE!	#VALUE!
dampener			N/A	N/A		#VALUE!	#VALUE!
dampener			N/A	N/A		#VALUE!	#VALUE!
Cont1	1.551	0.21	300.5	1382.02	1382.02	0	697.3049645
Cont3	1.551	0.21	289	1356	1355.13	0.87	687.9432624
Cont2	1.551	0.21	302	1320.3	N/A	#VALUE!	656.5441651
Cont1	1.551	0.21	300.5	1414.1	1407.1	7	717.9883946
Cont3	1.551	0.21	289	1407	1407	0	720.825274
Cont2	1.551	0.21	302	1565.8	N/A	#VALUE!	814.8291425
Cont3	1.551	0.21	289	1311.12	N/A	#VALUE!	659.0070922
Cont1	1.551	0.21	300.5	1289.4	1285.9	3.5	637.5886525
Cont2	1.551	0.21	302	1373.8	1372.7	1.1	691.03804

Density Error [kg/m^3]	ImpactVelocity [m/s]	sigma_V [m/s]	Velocity_err [%]	Impact Energy [J]
#DIV/0!	35		0	18.601625
#DIV/0!	70		0	74.4065
#DIV/0!			#DIV/0!	#N/A
#DIV/0!			#DIV/0!	#N/A
#DIV/0!			#DIV/0!	#N/A
#DIV/0!			#DIV/0!	#N/A
#DIV/0!			#DIV/0!	#N/A
#DIV/0!			#DIV/0!	#N/A
#DIV/0!			#DIV/0!	0
#DIV/0!			#DIV/0!	0
#DIV/0!			#DIV/0!	0
#DIV/0!			#DIV/0!	0
#DIV/0!			#DIV/0!	0
#DIV/0!			#DIV/0!	0
#DIV/0!			#DIV/0!	0
#DIV/0!	30.13	0.255	0.846332559	0.923703696
#DIV/0!	53.68	0.336	0.625931446	2.931969392
#DIV/0!	73.92	0.33	0.446428571	5.559789312
#DIV/0!	84.49	1.93	2.284293999	7.263484902
94.41266444	75.94454374	1.969940724	2.59392002	5.868506264
93.14512257	76.56217101	2.2007361	2.874443177	5.964346935
88.89379411	94.60781564	3.131407832	3.309882816	9.107274959
97.21312886	89.51328624	0.942869822	1.053329468	8.152849411
97.59723246	42.53293415	1.470558466	3.45745831	1.840708871
110.325029	72.55220032	2.839892972	3.914275459	5.355938652
89.22726587	100.7999932	1.489360795	1.477540571	10.33844981
86.3272837	90.09716702	3.383791037	3.755713025	8.259555746
93.56414468	90.3768541	3.833059366	4.241195828	8.310915333

Energy_err [J]	Energy_err [%]	Crater diameter [mm]	sigma_D [mm]	Diameter_err [%]
0	0	#N/A	#N/A	#N/A
0	0	#N/A	#N/A	#N/A
#N/A	#N/A	#N/A	#N/A	#N/A
#N/A	#N/A	#N/A	#N/A	#N/A
#N/A	#N/A	#N/A	#N/A	#N/A
#N/A	#N/A	#N/A	#N/A	#N/A
#N/A	#N/A	#N/A	#N/A	#N/A
#N/A	#N/A	#N/A	#N/A	#N/A
0	#DIV/0!	#N/A	#N/A	#N/A
0	#DIV/0!	#N/A	#N/A	#N/A
0	#DIV/0!	#N/A	#N/A	#N/A
0	#DIV/0!	#N/A	#N/A	#N/A
0	#DIV/0!	#N/A	#N/A	#N/A
0	#DIV/0!	#N/A	#N/A	#N/A
0	#DIV/0!	#N/A	#N/A	#N/A
0.01563521	1.692665118	#N/A	#N/A	#N/A
0.036704237	1.251862891	#N/A	#N/A	#N/A
0.049640976	0.892857143	#N/A	#N/A	#N/A
0.3318387	4.568587999	#N/A	#N/A	#N/A
0.304448718	5.18784004	33.43333333	2.862496967	8.561805486
0.342883527	5.748886353	22.06666667	2.007209229	9.096114331
0.602880258	6.619765632	23.1	0.637704216	2.76062431
0.171752731	2.106658937	22.725	1.938265978	8.529223224
0.127283484	6.914916619	13.75	2.109798569	15.34398959
0.419292385	7.828550919	22.45	2.041751699	9.094662356
0.305509581	2.955081143	47.7	4.589117562	9.620791535
0.620410422	7.51142605	33.675	3.233902441	9.603273768
0.704964389	8.482391657	29.5	0.95131488	3.224796202

Notes	Video
	file
Projectile deflected upwards	file
Sabot did not open	
Sabot did not open	
Sabot did not open	
Sabot opened but impacted before projectile	
Inner tube launched with projectile	
Success	
Success	
Success	
Success	
No container (unconstrained) therefore the melt means mass loss is meaningless	
Shattered	

C

Additional plots

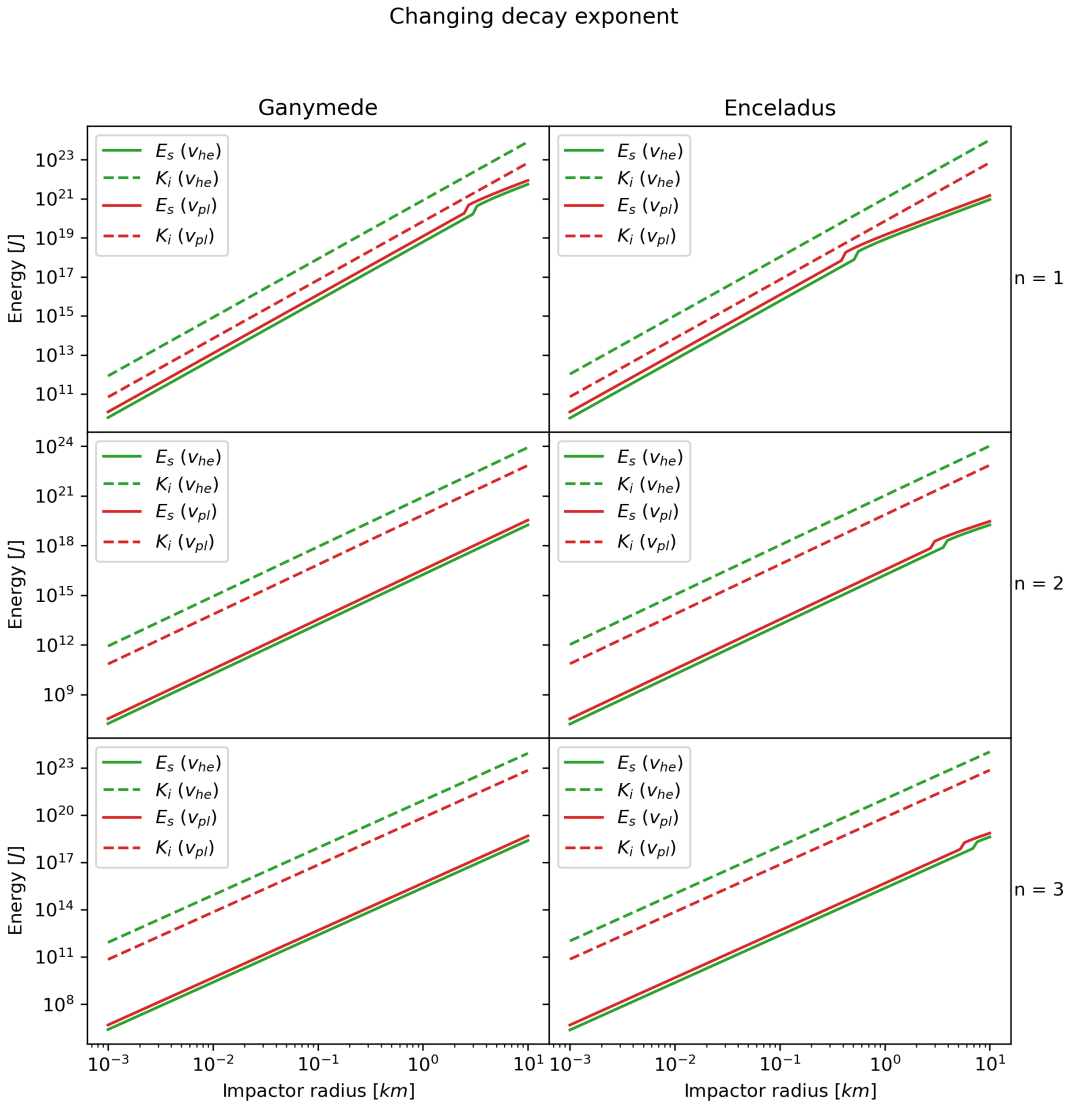

Figure C.1: Required shattering energy and impactor kinetic energy compared to impactor radius for Ganymede and Enceladus. Each row represents a different decay exponent. Plots obtained with impactor density of 1000 kg/m^3.

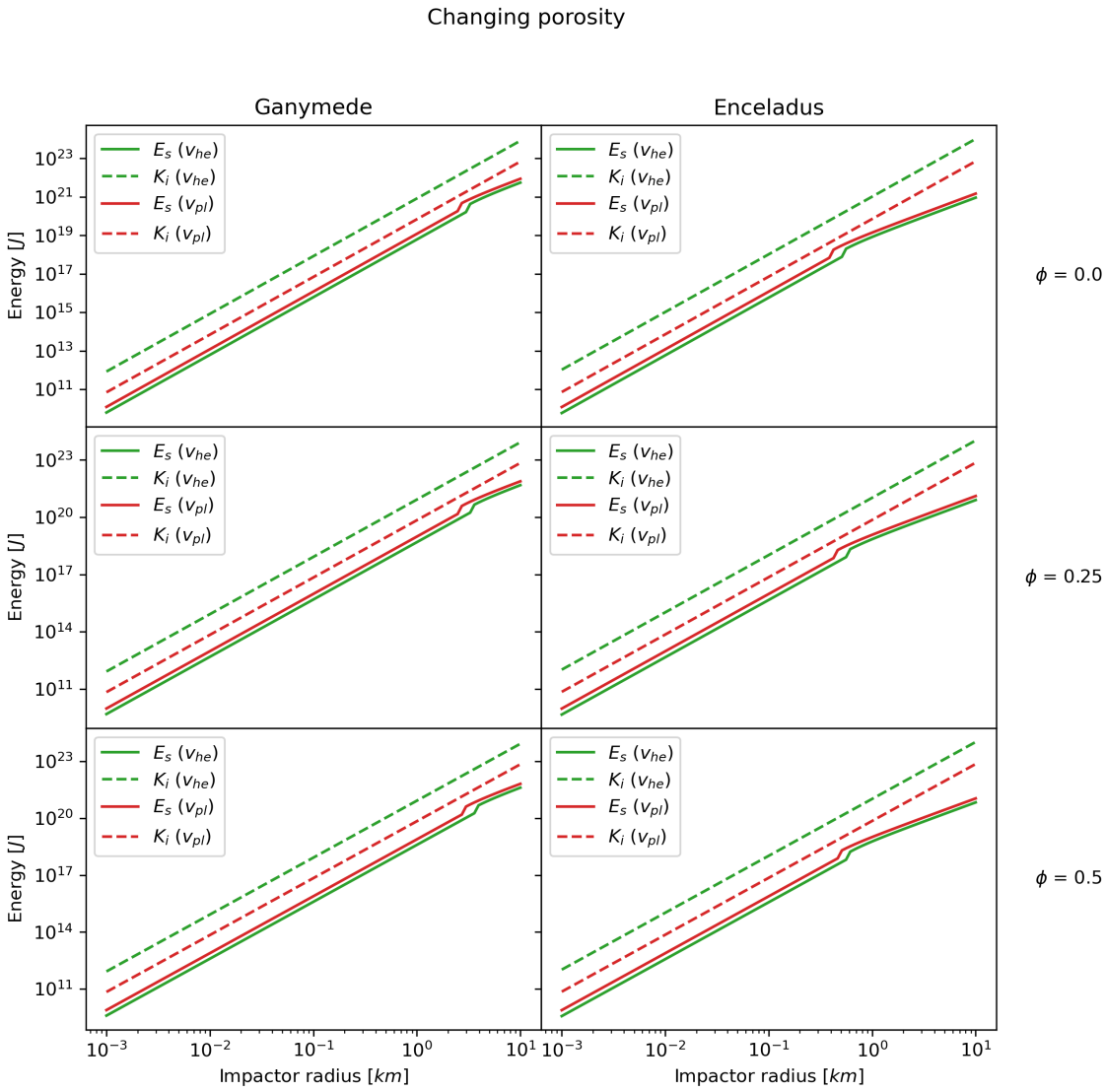

Figure C.2: Required shattering energy and impactor kinetic energy compared to impactor radius for Ganymede and Enceladus. Each row represents a different ice porosity. Plots obtained with impactor density of 300 kg/m^3.

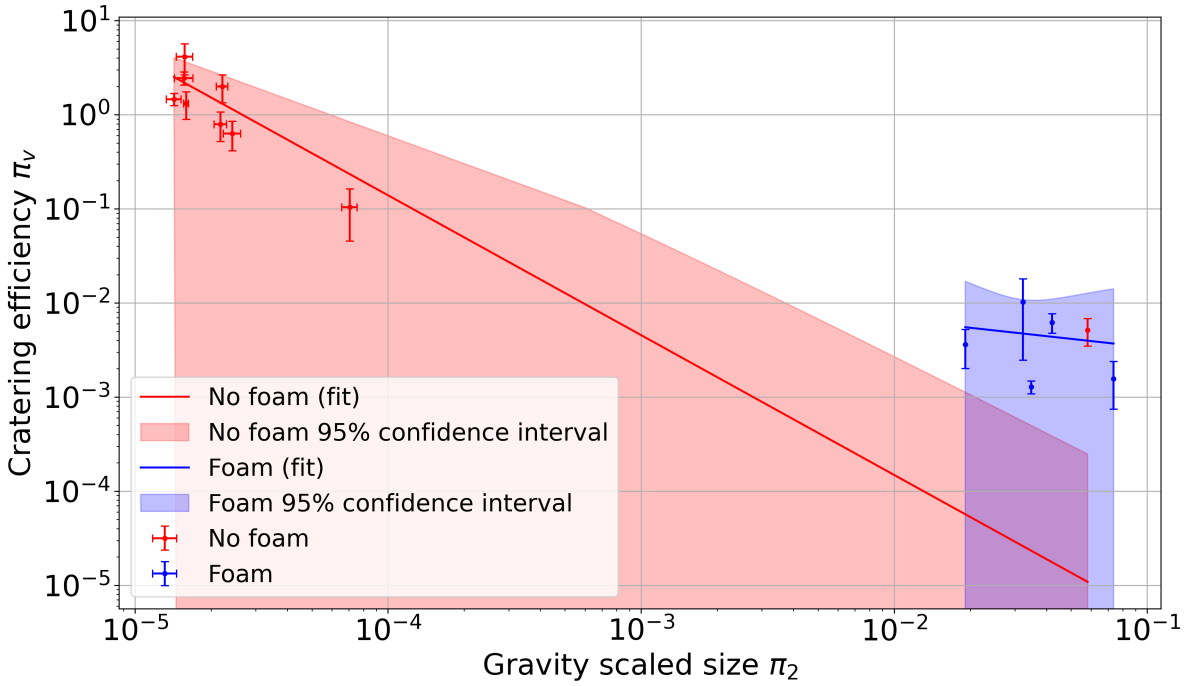

Figure C.3: Results of all (valid) impact experiments in ice blocks divided by container (foam/no foam), along with π scaling relationships and 95% confidence intervals.

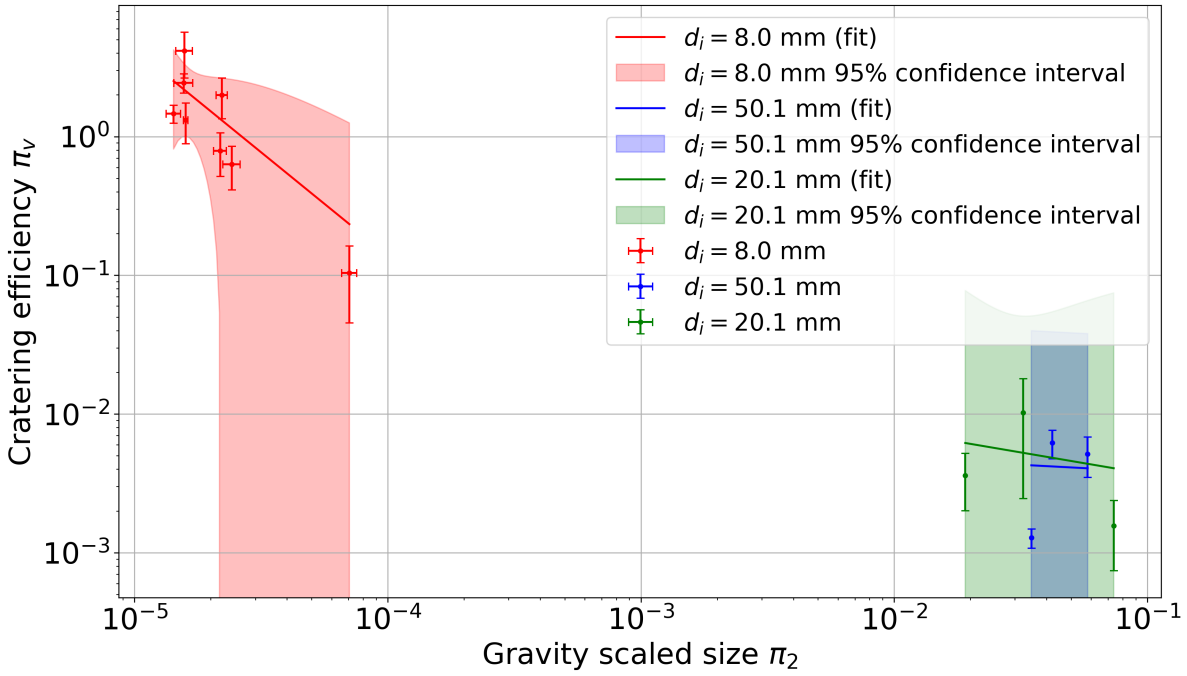

Figure C.4: Results of all (valid) impact experiments in ice blocks divided by impactor diameter, along with π scaling relationships and 95% confidence intervals.

D

Schematics

This page was intentionally left blank.

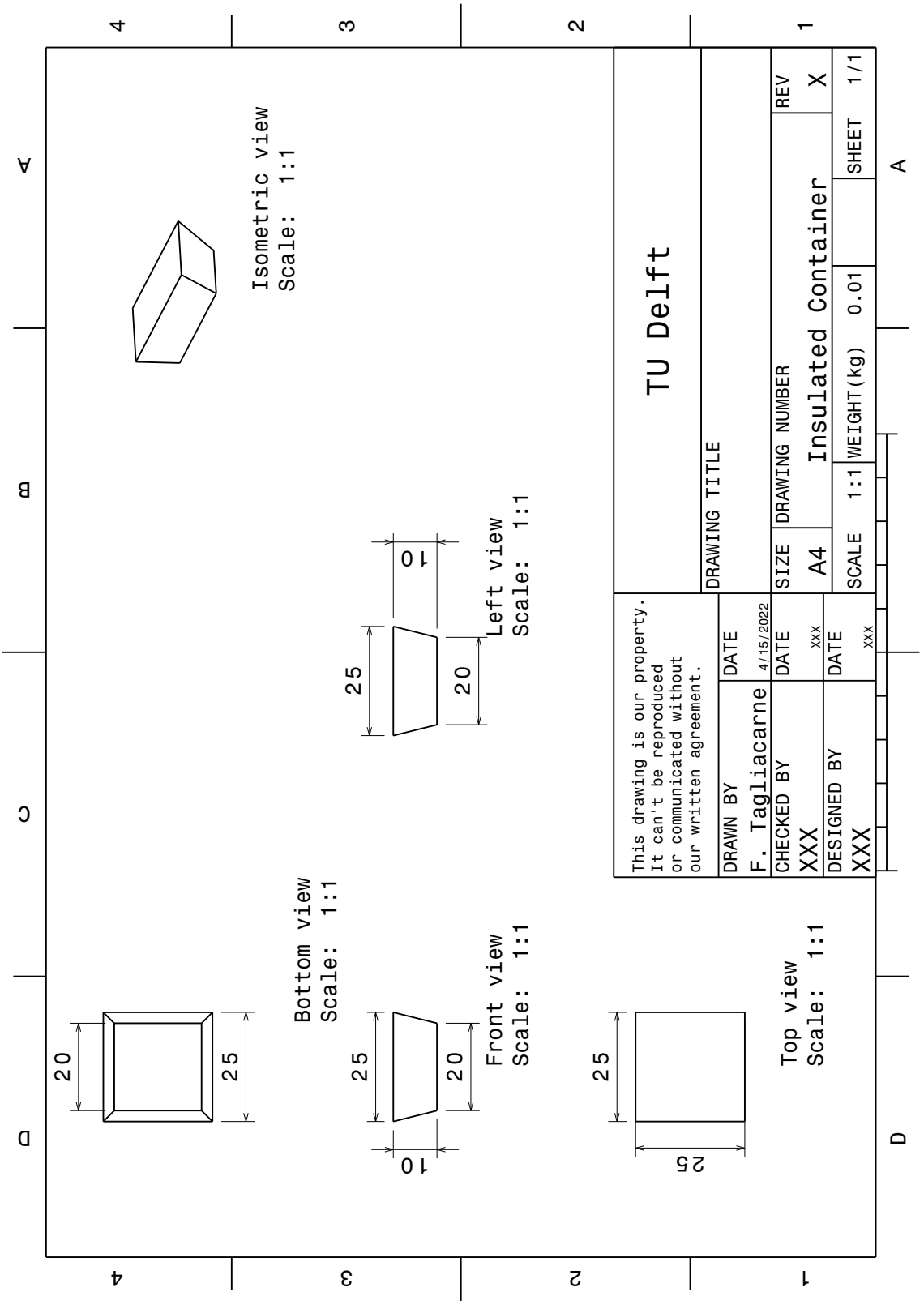

Figure D.1: Full size image of the schematics for the insulated container.

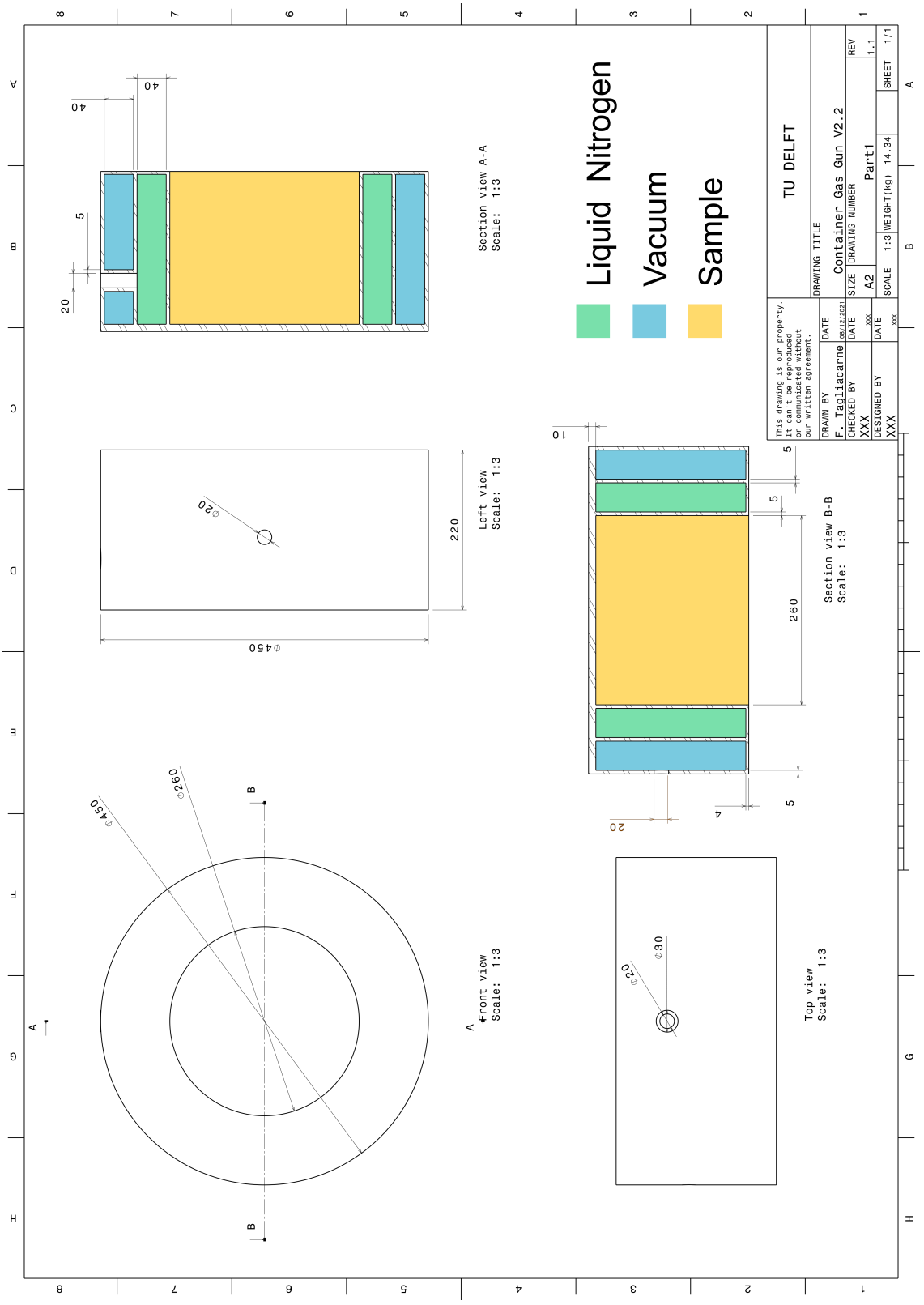

Figure D.2: Full size image of the schematics for the steel container.

E

Derivations

This chapter includes all the required derivations ued in this work.

E.1. Drag acceleration

The formula for the drag is given by Equation 4.1 (Anderson & Bowden, 2005), where C_D is the drag coefficient, ρ is the air density, V_i is the projectile velocity, and A is the surface area perpendicular to the airflow.

$$D = C_D A \frac{1}{2} \rho V_i^2 \tag{E.1}$$

The acceleration is defined as the change in velocity over time or:

$$a(t) = \frac{\mathrm{d}v(t)}{\mathrm{d}t} \tag{E.2}$$

Where $a(t)$ is the acceleration at time t, and $v(t)$ is the velocity at time t From Newton's second law of motion (Olenick et al., 1986):

$$F(t) = ma(t) \tag{E.3}$$

Where $F(t)$ is the sum of the forces acting on a body of mass m (mass does not change over time). Substituting the drag D from Equation E.1 as the force F in Equation E.3, and a from Equation E.2 into Equation E.3, the following equation can be obtained.

$$\Delta V = \int_{t_0}^{t_1} a(t)dt = \int_{t_0}^{t_1} \frac{D(t)}{m} dt = \int_{t_0}^{t_1} \frac{C_D A \rho V_i^2}{2m} dt \tag{E.4}$$

Substituting $dt = dx/V_i$ the following equation is obtained.

$$\Delta V = \int_{x_0}^{x_1} \frac{C_D A \rho V_i}{2m} dx \tag{E.5}$$

In the equation above, the only parameter that changes with either time or position is the velocity itself. However, in order to simplify the calculations this velocity is assumed that the change in velocity is negligible for now (i.e. $\Delta V \ll 1$). The ΔV can then be calculated using the equation below.

$$\Delta V = \frac{1}{2} \frac{C_D A}{m} \rho V_i \Delta x \tag{E.6}$$

Note that if the result from Equation E.6 is too large ($\Delta V/V > 0.01$) the assumption made at the end of Equation E.5 to simplify the equation is no longer valid. However, in that case the assumption that is being verified in subsection 4.1.1 is wrong, meaning there is no need for an estimate of the change in velocity when $\Delta V/V > 0.01$.

E.2. Impactor diameter uncertainty

The impactor diameter can be obtained using Equation 7.2 (repeated below).

$$L = \left(\beta \left(1.61 \left(\frac{\rho_t}{\rho_i} \right)^{\alpha} \left(D^3 \left(\frac{d}{D} \right)^2 \left(3 - 2\frac{d}{D} \right) \right)^{\alpha} \frac{g}{v_i^2} \right)^{-1} \right)^{1/(1-3\alpha)}$$

The propagation of uncertainty can then be calculated using equations E.8 through E.10 (Palmer, 2003).

$$x = 1.61 \left(\frac{\rho_t}{\rho_i} \right)^{\alpha} \left(D^3 \left(\frac{d}{D} \right)^2 \left(3 - 2\frac{d}{D} \right) \right)^{\alpha} \frac{g}{v_i^2} \tag{E.7}$$

$$\frac{\partial L}{\partial \alpha} = L(1-3\alpha)^2 \left(3\log\left(\frac{\beta}{x} \right) + (3\alpha - 1)\log\left(\frac{6V}{\pi} \right) \right) \tag{E.8}$$

$$\frac{\partial L}{\partial \beta} = \frac{1}{1-3\alpha}\frac{L}{\beta} \tag{E.9}$$

$$\delta L = \sqrt{\left(\frac{\partial L}{\partial \alpha}\delta\alpha \right)^2 + \left(\frac{\partial L}{\partial \beta}\delta\beta \right)^2} \tag{E.10}$$

Where $\frac{\partial L}{\partial \alpha}$ is the partial derivative of L with respect to α, $\frac{\partial L}{\partial \beta}$ is the partial derivative of L with respect to β, δL is the uncertainty in L, $\delta\alpha$ is the uncertainty in α, and $\delta\beta$ is the uncertainty in β.

Bibliography

Anderson, J. D., & Bowden, M. L. (2005). Introduction to flight.

Baker, W. E., Cox, P., Kulesz, J., Strehlow, R., & Westine, P. (2012). *Explosion hazards and evaluation*. Elsevier.

Barucci, M. A., Belskaya, I., Fulchignoni, M., & Birlan, M. (2005). Taxonomy of centaurs and trans-neptunian objects. *The Astronomical Journal*, *130*(3), 1291.

Bell, S. W. (2020). Relative Crater Scaling Between the Major Moons of Saturn: Implications for Planetocentric Cratering and the Surface Age of Titan. *Journal of Geophysical Research: Planets*, *125*(7), 1–18. https://doi.org/10.1029/2020JE006392

Bertie, J., Calvert, L., & Whalley, E. (1964). Transformations of ice vi and ice vii at atmospheric pressure. *Canadian journal of Chemistry*, *42*(6), 1373–1378.

Bottke, W. F., Durda, D. D., Nesvorný, D., Jedicke, R., Morbidelli, A., Vokrouhlický, D., & Levison, H. F. (2005). Linking the collisional history of the main asteroid belt to its dynamical excitation and depletion. *Icarus*, *179*(1), 63–94. https://doi.org/10.1016/j.icarus.2005.05.017

Britt, D. T., & Consolmagno, G. J. (2004). Meteorite porosities and densities: A review of trends in the data, In *Lunar and planetary science conference*.

Britt, D., Consolmagno, G., & Merline, W. (2006). Small body density and porosity: New data, new insights, In *37th annual lunar and planetary science conference*.

Chiang, E. I., & Lithwick, Y. (2005). Neptune trojans as a test bed for planet formation. *The Astrophysical Journal*, *628*(1), 520–532. https://doi.org/10.1086/430825

Cintala, M., Smrekar, S., Horz, F., & Cardenas, F. (1985). Impact experiments in h2o ice, i: Cratering, In *Lunar and planetary science conference*.

Collins, G., & Head, J. (1996). Criteria for determination of volcanic embayment of impact craters on venus, In *Lunar and planetary science conference*.

Croft, S. K., Kieffer, S. W., & Ahrens, T. J. (1979). Low-velocity impact craters in ice and ice-saturated sand with implications for Martian crater count ages. *Journal of Geophysical Research*, *84*(B14), 8023–8032. https://doi.org/10.1029/JB084iB14p08023

Ćuk, M., Dones, L., & Nesvornỳ, D. (2016). Dynamical evidence for a late formation of saturn's moons. *The Astrophysical Journal*, *820*(2), 97. https://doi.org/10.3847/0004-637x/820/2/97

Davis, A. M., Holland, H., & Turekian, K. (2003). *Meteorites, comets, and planets* (Vol. 1).

Dermott, S. F., & Murray, C. D. (2020). Nature of the kirkwood gaps in the asteroid belt. In *Hamiltonian dynamical systems* (pp. 655–659). CRC Press.

Fink, J., Greeley, R., & Gault, D. E. (1982). Impact cratering experiments in Bingham materials and the morphology of craters on Mars and Ganymede. *Lunar and Planetary Science Conference Proceedings*, *12*, 1649–1666.

Fraser, W. C., Bannister, M. T., Pike, R. E., Marsset, M., Schwamb, M. E., Kavelaars, J., Lacerda, P., Nesvornỳ, D., Volk, K., Delsanti, A., et al. (2017). All planetesimals born near the kuiper belt formed as binaries. *Nature Astronomy*, *1*(4), 1–6.

Frederking, R. M. W., Svec, O. J., & Timco, G. W. (1988). *On measuring the shear strength of ice*. National Research Council Canada, Institute for Research in Construction.

Gaffney, E. S., & Matson, D. L. (1980). Water ice polymorphs and their significance on planetary surfaces. *Icarus*, *44*(2), 511–519. https://doi.org/10.1016/0019-1035(80)90041-X

Gault, D. E., Quaide, W. L., & Oberbeck, V. R. (1974). Impact cratering mechanics and structures. *A Primer in Lunar Geology*, 177–189.

Grieve, R. (1999). *Traces of catastrophe: A handbook of shock-metamorphic features in terrestrial meteorite impact structures* (Vol. 80). https://doi.org/10.1029/99EO00200

Gundlach, B., Kilias, S., Beitz, E., & Blum, J. (2011). Micrometer-sized ice particles for planetary-science experiments - I. Preparation, critical rolling friction force, and specific surface energy. *Icarus*, *214*(2)arXiv 1102.0430, 717–723. https://doi.org/10.1016/j.icarus.2011.05.005

Häßner, D., Mutschke, H., Blum, J., Zeller, T., & Gundlach, B. (2018). Laboratory measurements of the sub-millimetre opacity of amorphous and micro-particulate h2o ices for temperatures above 80 k. *Monthly Notices of the Royal Astronomical Society*, *481*(4), 5022–5033.

Hogerheijde, M. R., van Dishoeck, E. F., Blake, G. A., & van Langevelde, H. J. (1998). Envelope Structure on 700 AU Scales and the Molecular Outflows of Low-Mass Young Stellar Objects. *The Astrophysical Journal*, *502*(1), 315–336. https://doi.org/10.1086/305885

Holsapple, K. A. (1993). The scaling of impact processes in planetary sciences. *Annual review of earth and planetary sciences*, *21*(1), 333–373.

Horedt, G. P., & Neukum, G. (1984). Planetocentric versus heliocentric impacts in the Jovian and Saturnian Satellite System. *Journal of Geophysical Research: Solid Earth*, *89*(B12), 10405–10410. https://doi.org/10.1029/JB089iB12p10405

Ida, S. (2019). The origin of saturn's rings and moons. *Science*, *364*(6445), 1028–1030.

Iess, L., Militzer, B., Kaspi, Y., Nicholson, P., Durante, D., Racioppa, P., Anabtawi, A., Galanti, E., Hubbard, W., Mariani, M., et al. (2019). Measurement and implications of saturn's gravity field and ring mass. *Science*, *364*(6445), eaat2965.

Jenniskens, P., & Blake, D. F. (1994a). Structural transitions in amorphous water ice and astrophysical implications. *Science*, *265*(5173), 753–756. https://doi.org/10.1126/science.11539186

Jenniskens, P., & Blake, D. F. (1994b). Structural transitions in amorphous water ice and astrophysical implications. *Science*, *265*(5173), 753–756.

Kant, I. (1755). *Universal natural history and theory of the heavens*.

Kawakami, S.-I., Mizutani, H., Takagi, Y., Kumazawa, M., & Kato, M. (1983). IMPACT EXPERIMENTS ON ICE. *Journal of Geophysical Research*, *88*(B7), 5806–5814. https://doi.org/10.1029/JB088iB07p05806

Kieffer, S. W., & Simonds, C. H. (1980). The role of volatiles and lithology in the impact cratering process. *Reviews of Geophysics*, *18*(1), 143–181.

Kirchoff, M. R., Bierhaus, E. B., Dones, L., Robbins, S. J., Singer, K. N., Wagner, R. J., & Zahnle, K. J. (2018). Cratering histories in the saturnian system. *Enceladus and the icy moons of Saturn*, 267–284. https://doi.org/10.2458/azu_uapress_9780816537075-ch013

Kraus, R. G., Senft, L. E., & Stewart, S. T. (2011). Impacts onto h2o ice: Scaling laws for melting, vaporization, excavation, and final crater size. *Icarus*, *214*(2), 724–738.

Kring, D. A. (2003). Environmental consequences of impact cratering events as a function of ambient conditions on earth. *Astrobiology*, *3*(1), 133–152.

Kring, D. A. (2006). Formation of a simple crater. https://www.lpl.arizona.edu/sic/education

Lange, M. A., & Ahrens, T. J. (1981). Fragmentation of ice by low velocity impact. *Lunar and Planetary Sciences*, *2*, 1667–1687.

Lange, M. A., & Ahrens, T. J. (1987). Impact experiments in low-temperature ice. *Icarus*, *69*(3), 506–518. https://doi.org/10.1016/0019-1035(87)90020-0

Le Gall, A., West, R. D., & Bonnefoy, L. E. (2019). Dust and Snow Cover on Saturn's Icy Moons. *Geophysical Research Letters*, *46*(21), 11747–11755. https://doi.org/10.1029/2019GL084218

Lellouch, E., Moreno, R., Bockelée-Morvan, D., Biver, N., & Santos-Sanz, P. (2022). Size and albedo of the largest detected oort-cloud object: Comet c/2014 un271 (bernardinelli-bernstein). *Astronomy & Astrophysics*, *659*, L1.

Lissauer, J. J., & de Pater, I. (2019). *Fundamental planetary science*. https://doi.org/10.1017/9781108304061

Lorenz, R., Wood, C., Lunine, J., Wall, S., Lopes, R., Mitchell, K., Paganelli, F., Anderson, Y., Wye, L., Tsai, C., et al. (2007). Titan's young surface: Initial impact crater survey by cassini radar and model comparison. *Geophysical Research Letters*, *34*(7). https://doi.org/https://doi.org/10.1029/2006GL028971

Mastrapa, R., Bernstein, M., Sandford, S., Roush, T., Cruikshank, D., & Dalle Ore, C. (2008). Optical constants of amorphous and crystalline h2o-ice in the near infrared from 1.1 to 2.6 μm. *Icarus*, *197*(1), 307–320.

Mdf. (2006). The asteroids of the inner solar system and jupiter. Encyclopedia Britannica. https://commons.wikimedia.org/w/index.php?curid=1951518

Melosh, H. J. (1989). Impact cratering: A geologic process. *icgp*.

Melosh, H. J. (2011). *Planetary surface processes*. https://doi.org/10.1017/cbo9780511977848

Mishima, O., Calvert, L., & Whalley, E. (1984). 'melting ice'i at 77 k and 10 kbar: A new method of making amorphous solids. *Nature*, *310*(5976), 393–395.

Moore, F. (1965). *Rheology of ceramic systems* (Vol. 2). MacLaren.

Murray, C. D., & Dermott, S. F. (1999). *Solar system dynamics*. Cambridge university press.

Olenick, R. P., Apostol, T. M., Goodstein, D. L., & Arons, A. (1986). The mechanical universe: Introduction to mechanics and heat. American Association of Physics Teachers.

Palmer, M. (2003). Propagation of uncertainty through mathematical operations. *Massachusetts Institute of Technology*.

PHOTRON. (2022). *Product datasheet nova s* (tech. rep.). NOVA S6 https://photron.com/wp-content/uploads/2022/01/NOVA_4models_Rev.2022.01.11.pdf.

Pierazzo, E., Vickery, A., & Melosh, H. (1997). A Reevaluation of Impact Melt Production. *Icarus*, *127*(2), 408–423. https://doi.org/10.1006/icar.1997.5713

Pilkington, M., & Grieve, R. (1992). The geophysical signature of terrestrial impact craters. *Reviews of Geophysics*, *30*(2), 161–181.

Prieur, N. C., Rolf, T., Luther, R., Wünnemann, K., Xiao, Z., & Werner, S. C. (2017). The effect of target properties on transient crater scaling for simple craters. *Journal of Geophysical Research: Planets*, *122*(8), 1704–1726.

Resolution, I. (2006). B5: Definition of a planet in the solar system. IAU.

Richardson, J. E., Melosh, H. J., Lisse, C. M., & Carcich, B. (2007). A ballistics analysis of the deep impact ejecta plume: Determining comet tempel 1's gravity, mass, and density. *Icarus*, *191*(2), 176–209.

Santra, B., Klimeš, J., Tkatchenko, A., Alfè, D., Slater, B., Michaelides, A., Car, R., & Scheffler, M. (2013). On the accuracy of van der waals inclusive density-functional theory exchange-correlation functionals for ice at ambient and high pressures. *The Journal of Chemical Physics*, *139*(15), 154702.

Schenk, P. M. (2002). Thickness constraints on the icy shells of the galilean satellites from a comparison of crater shapes. *Nature*, *417*(6887), 419–421.

Schmidt, R. M., & Housen, K. R. (1987). Some recent advances in the scaling of impact and explosion cratering. *International Journal of Impact Engineering*, *5*(1-4), 543–560.

Schultz, P. H. (1996). Effect of impact angle on vaporization. *Journal of Geophysical Research E: Planets*, *101*(E9), 21117–21136. https://doi.org/10.1029/96JE02266

Schultz, P. H., Eberhardy, C. A., Ernst, C. M., A'hearn, M. F., Sunshine, J. M., & Lisse, C. M. (2007). The Deep Impact oblique impact cratering experiment. *Icarus*, *190*, 295–333. https://doi.org/10.1016/j.icarus.2007.06.006

Seki, N., Sugawara, M., & Fukusako, S. (1979). Radiative melting of ice layer adhering to a vertical surface. *Wärme-und Stoffübertragung*, *12*(2), 137–144.

Sheppard, S. S. (2006). A Thick Cloud of Neptune Trojans and Their Colors. *Science*, *313*(5786), 511–514. https://doi.org/10.1126/science.1127173

Shrine, N. R., Burchell, M. J., & Grey, I. D. (2002). Velocity scaling of impact craters in water ice over the range 1 to 7.3 km s-1. *Icarus*, *155*(2), 475–485. https://doi.org/10.1006/icar.2001.6734

Shrine, N. R., Burchell, M., & Grey, I. (2000). Velocity scaling of impact craters in water ice with relevance to cratering on icy planetary surfaces, In *Lunar and planetary science conference*.

Stansberry, J., Grundy, W., Brown, M., Cruikshank, D., Spencer, J., Trilling, D., & Margot, J.-L. (2008). Physical properties of kuiper belt and centaur objects: Constraints from the spitzer space telescope. *The Solar System Beyond Neptune*, *161*.

Tagliacarne, F. (2021). *Determining the origin of impactors on titan via laboratory experiments* [TU Delft]. TU Delft.

Tancredi, G., Fernández, J. A., Rickman, H., & Licandro, J. (2006). Nuclear magnitudes and the size distribution of jupiter family comets. *Icarus*, *182*(2), 527–549.

Tedesco, E. F. (2021). Asteroid. Encyclopedia Britannica. https://www.britannica.com/science/asteroid

Thomas, P., A'Hearn, M. F., Veverka, J., Belton, M. J., Kissel, J., Klaasen, K. P., McFadden, L. A., Melosh, H. J., Schultz, P. H., Besse, S., et al. (2013). Shape, density, and geology of the nucleus of comet 103p/hartley 2. *Icarus*, *222*(2), 550–558.

Thomas, P., Tajeddine, R., Tiscareno, M., Burns, J., Joseph, J., Loredo, T., Helfenstein, P., & Porco, C. (2016). Enceladus's measured physical libration requires a global subsurface ocean. *Icarus*, *264*, 37–47.

Tulk, C., Molaison, J., Makhluf, A., Manning, C., & Klug, D. (2019). Absence of amorphous forms when ice is compressed at low temperature. *Nature*, *569*. https://doi.org/10.1038/s41586-019-1204-5

Vanzant, B. (1962). Dynamic rock penetration tests at atmospheric pressure, In *5th symposium on rock mechanics, university of minnesota*.

Wetherill, G. (1975). Late heavy bombardment of the moon and terrestrial planets, In *Lunar and planetary science conference proceedings*.

Woolum, D. S., & Cassen, P. (1999). Astronomical constraints on nebular temperatures: Implications for planetesimal formation. *Meteoritics & Planetary Science*, *34*(6), 897–907. https://doi.org/10.1111/j.1945-5100.1999.tb01408.x

Zahnle, K., Schenk, P., Levison, H., & Dones, L. (2003). Cratering rates in the outer solar system. *Icarus*, *163*(2), 263–289. https://doi.org/10.1016/S0019-1035(03)00048-4